Adsorption and Self-Assembly of Proteins at Chemically Modified Surfaces

Shohreh Zahedijasbi

A Dissertation Submitted to the Faculty of Graduate Studies

In Partial Fulfillment of the Requirements

for the Degree of

Doctor of Philosophy

Graduate Program in Chemistry

York University

Toronto, Ontario

October 2014

Abstract

Our research is mostly focused on the subject of adsorption and self-assembly of proteins at modified surfaces. We employed atomic force microscopy (AFM) to study bovine serum albumin (BSA) and insulin adsorption at 1-decene- and methyl 10-undecenoate-modified Si(111) substrates. The results were compared to matrix-assisted laser desorption/ionization-mass spectroscopy (MALDI-MS) data previously published in the Morin group. The MALDI-MS spectra showed a big insulin signal, while BSA was not detected for 1 mg/mL BSA and 10% saturated insulin solutions. Our AFM images revealed considerable BSA adsorption, whereas it was not possible to observe insulin molecules. This clearly shows that in addition to the low quantity of the protein, a stronger interaction between the surface and the protein may result in a weak MALDI-MS signal and prevent quantitative analysis using this technique.

Self-assembled monolayers on Au surfaces were used to investigate the oligomerization of truncated K122-4 (ΔK122-4) pilins into a new protein nanostructure. Employing AFM, we observed that at hydrophobic layers, with more than 10-30% accessible hydrophobic component, ΔK122-4 pilins oligomerize to a nanoweb.

To differentiate the structure of ΔK122-4 nanoweb from the aggregation of the pilins at hydrophilic surfaces, electrochemical impedance spectroscopy was employed. Through equivalent circuit fitting, capacitance values of 3.7 ± 0.4 $\mu F/cm^2$ and 2.5 ± 0.2 $\mu F/cm^2$ were obtained for the aggregated pilins and the web pattern, respectively. Because of the higher average thickness of the former layer, this could support the presence of water in

this layer. A dielectric constant (ε) of 5.1 ± 0.7 was obtained for the nanoweb. This low value could indicate a more compact and ordered assembly.

Finally, conductive protein nanotube (PNTs) fabrication was performed by electroless copper deposition at ΔK122-4 PNTs in aqueous solution. The nanostructures were catalyzed by $PdCl_4^{2-}$. At least 20% of the accessible amino acids of the PNTs have S-, N- and O-donor side chains which are able to form a complex with Pd(II). Metallization was verified using scanning electron microscopy (SEM).

Acknowledgements

First, I would like to thank God who gave me the grace and privilege to pursue this program and successfully complete it in spite of many challenges faced.

I would like to express my sincere gratitude to my supervisor, Dr. Sylvie Morin for the continuous support of my Ph.D. study and research. I appreciate all her contributions of time, ideas, and funding to make my Ph.D. experience productive and stimulating.

I greatly appreciate the collaboration with Dr. Gerald F. Audette and his students Stephanie Lombardo, Anna Petrov and Arik Vishnevsky in protein nanotube research.

I am grateful to Susan Suk-Kyung Jeung for help in FT-IR measurements, Souzan Elkhazendar for copper electroless deposition and TEM measurements, and Takyi Ofori for SAM preparation.

I also wish to thank the members of my supervising and reading committee, Dr. Valeria Tsoukanova and Dr. Pierre G. Potvin for their advice and questions.

I would like to appreciate Karen Rethoret, at York University, Imaging Facility, for her contribution to the TEM measurements. I'd like to thank Dr. Morin's group member.

I would like to dedicate this thesis to my dear parents and my beloved daughter Shabnam.

Statement of Collaboration

The experiments related to ΔK122-4 pilins in this thesis were carried out in collaboration with Professor Gerald F. Audette's group. Stephanie Lombardo, Anna Petrov, and Arik Vishnevsky prepared ΔK122-4 pilin monomer solutions and grew PNTs in solution. I prepared and characterized all modified surfaces. After incubation, I imaged the samples using atomic force microscopy. I also employed the samples for electrochemical tests. PNTs grown in solution were employed for metal deposition and were imaged using transmission electron microscope.

The work presented in chapter five was performed with help of Souzan Elkhazendar, an honours thesis student in Prof. Morin's group. Susan Suk-Kyung Jeung, another honours thesis student in Prof. Morin's group, carried out some of FT-IR measurements presented in chapters two and three. Takyi Ofori, a volunteer undergrad student, prepared some of SAM surfaces for FT-IR measurements presented in chapter three. I assisted the students and advised them in the laboratory and took part in the experimental work presented therein. I really appreciate their help.

Table of Contents

List of Tables

List of Figures

List of Abbreviations

AC	Alternating current
AET	2-Aminoethanethiol
AFM	Atomic force microscopy
ATR-FTIR	Attenuated total reflection Fourier transform infrared
BSA	Bovine serum albumin
CNT	Carbon nanotube
CPE	Constant phase element
CPE_p	Constant phase element representing the capacitive behaviour of a pilin layer
CPE_{SAM}	Constant phase element representing the capacitive behaviour of a SAM
CV	Cyclic voltammetry
DLVO	Derjaguin-Landau-Verwey-Overbeek
DMAB	Dimethylamine borane
dsDNA	Double-stranded DNA
EFM	Electrostatic force microscopy
EIS	Electrochemical impedance spectroscopy
ELD	Electroless deposition
fcc	Face centered cubic
hcp	Hexagonal close packing
HCP1	Heme carrier protein 1

HOPG	Highly oriented pyrolytic graphite
HPA	Human plasma albumin
I	Insulin
iep	Isoelectric point
MALDI-MS	Matrix-assisted laser desorption/ionization mass spectroscopy
MPD	2-Methyl-1,3-propanediol
Na_2H_2EDTA	Ethylenediaminetetraacetic acid disodium salt
PNT	Protein nanotube
pzc	Potential at the point of zero charge
SAM	Self-assembled monolayer
SCE	Saturated calomel electrode
SELDI	Surface-enhanced laser desorption/ionization
SEM	Scanning electron microscopy
SHE	Saturated hydrogen electrode
ssDNA	Single-stranded DNA
STM	Scanning tunneling microscopy
SWNT	Single-walled carbon nanotube
T4P	Type IV pilus
TEA	Triethanolamine
TEM	Transmission electron microscopy
TMV	Tobacco mosaic virus

TOC	Total oxidizable carbon
ToMV	Tomato mosaic virus
Tris	2-Amino-2-(hydroxymethyl)-1,3-propanediol

List of Symbols

$\Delta G°$	Change in standard Gibbs energy
$\Delta H°$	Change in standard enthalpy
$\Delta K122\text{-}4$	Truncated K122-4
$\Delta S°$	Change in standard entropy
ε	Dielectric constant
$\varepsilon_{\circ}$	Space permittivity constant
φ	Phase-angle between **E** and **i**
ω	Angular frequency
A	Electrode surface area
C	Capacitance
C_{dl}	Impedance due to double layer charging
C_s	Pseudocapacitor
d	Plate distance
d_p	Thickness of a pilin layer
E(t)	Potential
f	Frequency
i	Current
j	$\sqrt{-1}$
K_{f2}	Dimerization constant
K_{f4}	Tetramerization constant

m	Number of methylenes in alkanethiols ($CH_3(CH_2)_mSH$)
n	(1-n) 90° shows clockwise deflection of a Nyquist diagram due to surface inhomogeneity
n_p	(1-n) 90° shows clockwise deflection of a Nyquist diagram due to the surface inhomogeneity of a pilin layer
n_{SAM}	(1-n) 90° shows clockwise deflection of a Nyquist diagram due to the surface inhomogeneity of a SAM
q	Electric charge
Q	With unit of $\Omega^{-1}s^n$ represents CPE
Q_p	With unit of $\Omega^{-1}s^n$ represents the CPE of a pilin layer
Q_{SAM}	With unit of $\Omega^{-1}s^n$ represents the CPE of a SAM
R	Resistance
R_Ω	Ohmic resistance
R_p	Ohmic resistance of a pilin layer
R_{SAM}	Ohmic resistance of a SAM
R_t	Resistance to charge transfer activity
V_A	Van der Waals attractive force
V_R	Electrostatic double layer repulsive force
V_S	Solvation force
V_T	Total potential energy
Z	Impedance

Z_f	Impedance due to faradaic process
Z_{Im}	Imaginary part of impedance
Z_{Re}	Real part of impedance

Chapter 1: Introduction

1.1. Protein Adsorption

Proteins play a key role in fields such as implants [1,2], biosensors [3,4], cosmetics [5,6], pharmaceuticals [7,8], food processing [9,10] and bionanotechnology [11-14]. Adsorption onto a substrate is often a significant step in many industrial and medical processes involving proteins.

A striking example of the importance of protein adsorption onto various types of surfaces is related to insulin.[15-19] For instance, in order to predict the exact quantity of injected insulin, it is necessary to know the amount of insulin adsorbed into the infusion system and container. Insulin adsorption is also very important in designing an artificial pancreas.[20] Even though the adsorbed protein on an interface does not desorb easily, exchange with the proteins in the bulk solution is often reported.[21] When the protein with altered structure, due to the adsorption into the interface, distributes back into the solution, it can result in aggregation.[21] Another example involves medical prostheses, where in order to reduce the risk of unwanted blood clotting, it is important to prevent adsorption of blood proteins.[22]

1.1.1. Protein Structure

Proteins are made of twenty different α-amino acids. Each amino acid has a central carbon atom (alpha carbon), surrounded by an amino group (except for prolin), a carboxyl group, a hydrogen atom and a side side-chain (except for glycine having a hydrogen substituent as its side-chain). The structure of proteins shows four levels of

organization. The sequence of amino acids connected by peptide bonds is called the primary structure. (Fig. 1.1) The secondary structure is formed by hydrogen bonds. The most common secondary structures found in proteins are α-helices and β-sheets. (Fig. 1.2)

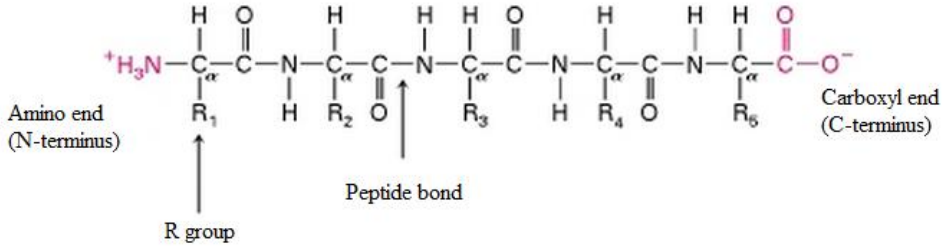

Fig. 1.1. Amino acid sequence of polypeptide chains. The N-terminus, the C-terminus, an R group and a peptide bond are shown in the figure. "Reprinted with permission from (Lodish, H.; Berk, A.; Zipursky, S. L.; Matsudaira, P.; Baltimore, D.; Darnell, J. Molecular Cell Biology; 4th Ed.; W. H. Freeman: New York, 2000, 1184 pages), Copyright (2000) National Library of Medicine."

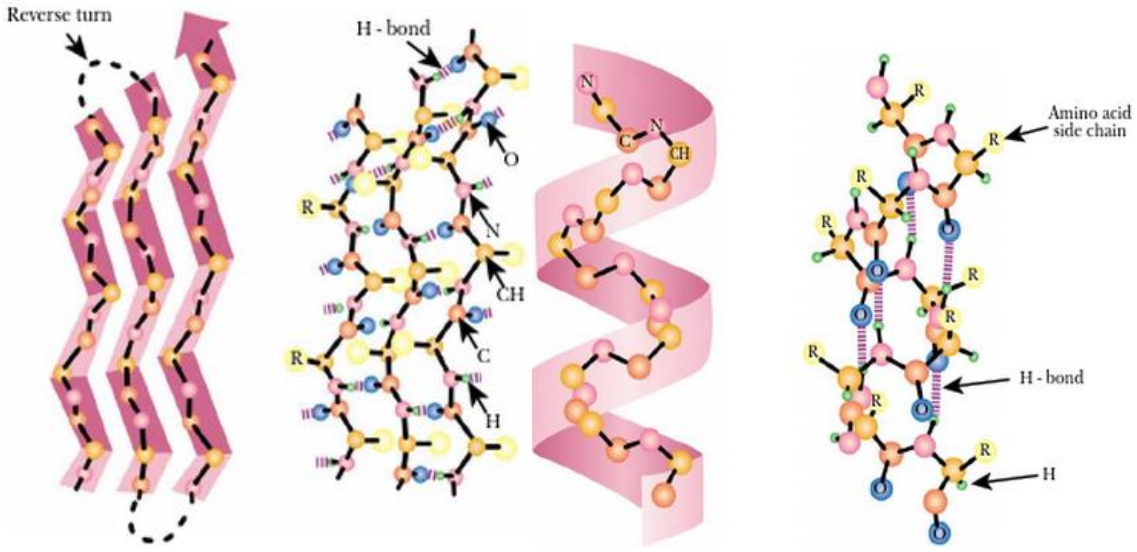

Fig. 1.2. Secondary structure of proteins. (a) Carbon backbone of an α-helix, (b) hydrogen bonding between the peptide groups of the α-helix shown in a, (c) carbon backbone of a β-sheet, and (d) hydrogen bonding between the β-sheet shown in c. "Reprinted from Molecular Biology, Clark, D.P., Protein Structure and Function, 802, Copyright (2005), with permission from Elsevier."

Interactions between the side chains of the amino acids result in further folding of the polypeptide chain to form the final 3-D structure called tertiary structure. The most important interactions that determine the structure of proteins are hydrophobic interactions, coulomb interactions between positively and negatively charged residues (salt bridge), hydrogen bonds, and disulfide bonds.[23] Fig. 1.3 shows some interactions which maintain 3-D structure of proteins. Assembly of several separate polypeptide chains forms a quaternary structure.[23]

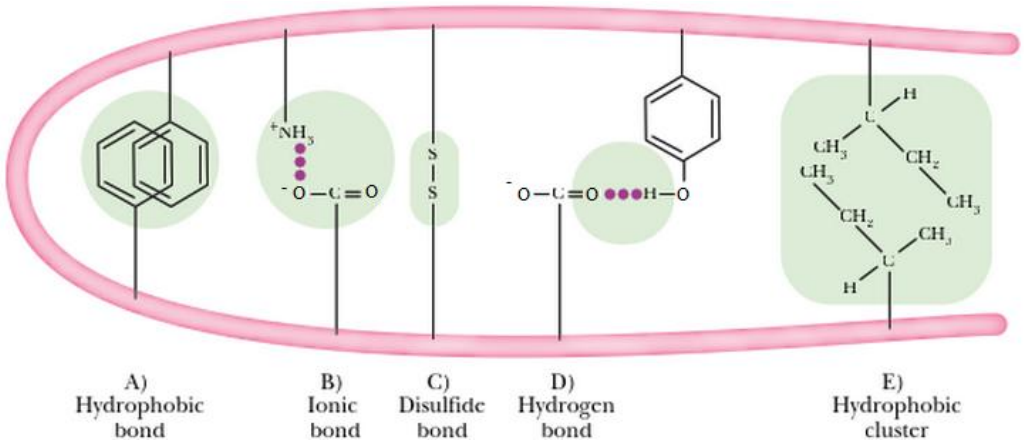

Fig. 1.3. Some bonds that form 3-D structure of proteins. "Reprinted from Molecular Biology, Clark, D. P., Protein Structure and Function, 802, Copyright (2005), with permission from Elsevier."

In an aqueous environment, protein molecules form a globular structure. In order to investigate what stabilizes the globular structure of proteins, G. C. Krescheck *et al.* used N-methylacetamide as a model for peptide units to examine the role of peptide-peptide hydrogen bonds in protein structure.[24] At 25°C, the following values for changes in the standard Gibbs energy (ΔG°), the enthalpy (ΔH°) and the entropy (ΔS°) were obtained for transferring one mole of N-methylacetamide from its medium to water.

$$(\text{-N-H}\ldots\text{O = C-})_{H_2O} \rightarrow (\text{-N-H, O = C-})_{H_2O} \quad (1)$$

$\Delta G° = -13 \text{ kJ mol}^{-1}$

$\Delta H° = 0 \text{ kJ mol}^{-1}$

$\Delta S° = +42 \text{ J K}^{-1} \text{ mol}^{-1}$

The negative $\Delta G°$ shows that in aqueous solution, the intermolecular hydrogen bond (modeled by the interaction of an N-methylacetamides and a molecule of water) is more favorable than the intramolecular one (modeled by the interaction of two N-methylacetamides). Therefore, even though hydrogen bonding between the peptide groups stabilizes the secondary structures, the compact structure is not stabilized by H-bonds between the peptide units. This reveals that hydrophobic interactions are the main driving force to form the globular structure of proteins in an aqueous environment.[24]

Hydrophobic interactions comprise spontaneous dehydration and subsequent aggregation of non-polar components in an aqueous environment. These interactions are not primarily motivated by any intrinsic interaction between the hydrophobic groups, but rather hydrophobic bonds are formed because the water-water interaction is more favorable than the interaction between the water and non-polar parts of the protein molecules. Therefore, in aqueous solution the hydrophobic parts dehydrate and aggregate to be shielded from the water.[23]

Hydrophobic interactions are associated with an entropy increase of the solvent molecules and an entropy decrease due to aggregation of the hydrophobic parts.[24] Moreover, the hydrophobic association releases heat. To model hydrophobic bonds, W. Norde *et al.* transferred molecules of a homologous series of alcohols, $H(CH_2)_nOH$, from

an aqueous solution into their own medium.[24] The following values are reported for each additional -CH_2 group at 25ºC:

$\Delta G° = -3.4$ kJ mol^{-1}

$\Delta H° = -0.4$ kJ mol^{-1}

$\Delta S° = +10.1$ J K^{-1} mol^{-1}

The measured value of 10.1 J K^{-1} mol^{-1} for $\Delta S°$ reveals that the entropy gain of the solvent molecules is much bigger than the entropy loss due to the hydrophobic aggregation. Moreover, the released heat also promotes the process.[24]

Even though hydrophobic interactions play an important role in the globular shape of the proteins in an aqueous environment, because of the geometrical restrictions, some of the hydrophobic parts are not buried inside the protein molecules. This leads to the tendency of the proteins to adsorb at both hydrophobic and hydrophilic surfaces.

In an aqueous environment, most of the charged amino acid residues of the protein are exposed to the solution. The charges presented in the hydrophobic interior part of the protein mostly form ion pairs. At the isoelectric point (iep) the electrokinetic charge[1] is zero, and the uniform distribution of the positive and negative charges facilitates intramolecular interactions.[24] At this point, a compact form with less free energy is more favorable. However, the excess of either positive or negative charge results in intramolecular repulsion. Therefore, an expanded structure is stabilized.[24]

[1] Electrokinetic charge includes the molecule charge due to (de)protonation and the charge of slipping layer around the protein molecule.[25]

1.1.2. Protein Denaturation and Aggregation

Aggregation or self-association of proteins may occur via different mechanisms. While native proteins can aggregate reversibly, misfolded proteins may undergo irreversible aggregation. As an example for the latter, in prion and diseases such as Alzheimer's, protein misfolding results in fibril formation.[26] When proteins lose their quaternary structure, tertiary structure and secondary structure present in their native state, denaturation occurs. Proteins denature at high or low pH, at high concentration of inorganic salts, in organic solvents (e.g., alcohol or chloroform), and with radiation or heat.[25] Denatured proteins may lose their solubility or aggregate.

1.1.3. Processes Involved in Protein Adsorption

A high tendency of proteins to adsorb at different surfaces is due to their amphiphilic nature. Several interactions such as van der Waals forces, hydrogen bonds, hydrophobic and electrostatic interactions are involved in protein adsorption. S. Kidoaki *et al.* divided the processes engaged in protein-surface interactions into three general steps of approach, attachment and detachment.[27] The amount of protein approaching to the surface is determined by transport properties of the protein molecules and intrinsic interactions between the protein and the surface; both are affected by solvent motion and its molecular properties.

When the protein approaches the surface, attachment may happen. Three factors involved in the attachment process are short-range interactions between the protein molecule and the surface, entropy gain due to the release of counter ions and hydration waters bound

between the protein and the surface, and entropy gain due to surface denaturation of the adsorbed protein.[27] Entropy gain even may drive endothermic adsorption.[28,29] For example, Fig. 1.4 shows the enthalpy of human plasma albumin (HPA) adsorption on hematite versus the surface coverage (θ) at 22°C and different pH values. This figure shows that under most conditions, the adsorption enthalpy is positive; therefore, the driving force for this adsorption is attributed to the increase of entropy rather than enthalpy loss.[29]

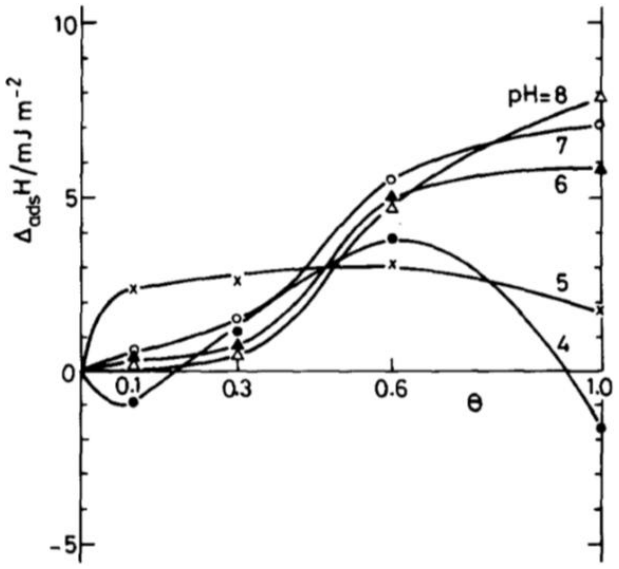

Fig. 1.4. Enthalpy of HPA adsorption onto hematite. T = 22°C. Electrolyte: 0.01 M KNO_3. The pH is indicated. "Reprinted from Journal of Colloid and Interface Science, 95, Koutsoukos, P. G.; Norde, W.; Lyklema, J., Protein Adsorption on Hematite (α-Fe_2O_3) Surfaces, 13 pages, Copyright (1983), with permission from Elsevier."

The third process is the detachment of the adsorbed protein. Because of the size, the free energy release due to protein adsorption is much greater than that of small molecules. Even though the free energy released because of adsorption of each amino acid of proteins is comparable to the free energy of thermal motion (1 kT, ca. 2.48 kJ/mol), the

adsorption of several amino acids, for example 50 amino acids, results in the release of a considerable amount of energy (~124 kJ/mol).[24] Consequently, protein molecules do not desorb easily by diluting the solution. However, factors such as competition by other species with higher surface adsorption affinity, thermal energy, and mechanical movement of the solvent can lead to replacement of the adsorbed molecules.[27,30]

1.1.4. Protein Stability

The stability of individual protein molecules in aqueous solution can be expressed by extended DLVO (Derjaguin-Landau-Verwey-Overbeek) theory as the sum of van der Waals attractive (V_A), electrostatic double layer repulsive (V_R), and hydration (V_S) forces between particles.[31-33]

$$V_T = V_R + V_A + V_S \quad (2)$$

The hydration force is a short range (~6 nm) repulsive force that acts between hydrophilic surfaces separated by a thin layer of water or hydrated ions adsorbed at the surfaces.[33-35] However, the nature of the hydration force is not completely understood.

1.2. Nanostructure Self-Assembly

In self-assembly, the subunits associate in a defined arrangement without guidance or management from an outside source. The non-covalent interactions between the subunits, as well as their geometry define the spatial organization of the assembly.[36] Generally, this assembly is associated with a large area of interface between the subunits. Although the interactions are individually weak, due to the considerable number of interactions, a significant strength is generated.[36] For biological materials, these non-covalent

interactions are typically hydrogen and ionic bonds, hydrophobic and electrostatic interactions, and van der Waal forces.

1.2.1. Nanotubes

Bionanostructure self-assembly has a wide range of applications from electronics to biomedicine.[11-14,37-43] Interest in nanotechnology is growing rapidly, and biology is a natural source for the building blocks of nanoscale materials.[43-51] Carbon nanotubes (CNTs) are the most studied synthesized nanostructures and possess a number of valuable and unique properties such as high thermal and electrical conductivity, flexibility, high tensile strength (several GPa), light weight and large surface area.[52] However, their limited biocompatibility restricts their bioapplications (e.g., biosensors).[53] For instance, due to hydrophobicity, CNTs have limited water-solubility, and also their electric properties are reduced by exposure to humidity, oxygen, N_2O and NH_3.[54]

Among other issues to be considered is the presence of residues from metal catalysts, used to produce CNTs, and the toxicity of CNTs.[53] It has been shown that carbon nanoparticles have a severe disruptive effect on phagocytosis, because of their shape, size, surface chemistry and mechanical properties.[55-59] While particles with a diameter of 2-3 μm exhibit maximum phagocytosis [56], single-walled carbon nanotubes (SWNTs), having a mean length of ca. 1 μm, are too small. However, multi-walled CNTs with a length of several μm are too big to be engulfed easily. [55] The fiber-like shape of CNTs also makes phagocytosis more difficult; it causes the CNTs to persist longer in the body.[57] Other drawbacks for CNTs applications are a lack of structural uniformity,

restricted reproducibility of precise structural properties, limited opportunities for covalent modification, as well as the costs involved.[54]

1.2.2. Carbon Nanotube Modification

Several attempts have been made to introduce various functional groups onto the surface of CNTs to increase their dispersion and biocompatibility.[60] For example, X. Su *et al.* covalently functionalized multi-walled CNTs with thermo-responsive poly(N-isopropylacrylamide) to raise their solubility and stability in water.[61]

Moreover, various biological properties are introduced to CNTs using immobilization of biochemical materials such as carbohydrates [62], biotin [63,64], DNA [65-67] and proteins [68,69] via covalent and non-covalent attachments. For example, carbohydrates are non-covalently introduced to carbon nanostructures to improve their water solubility and to enable them to interact selectively with biological systems such as pathogenic bacteria. This suggests their possible applications in imaging and sensing devices or even therapeutic fields.[62]

The main disadvantage of covalent functionalization of carbon nanostructures is the changes that occur in their lattice, resulting in variations in their intrinsic properties.[62] Ballistic conductivity, by which electrons travel in a medium with negligible electrical resistivity due to scattering, is reported for defect-free multi-walled and single-walled carbon nanotubes.[70-72] Ballistic conductivity can be affected by covalent bond and local structural defects which act as scattering centers.[70,73] Chemical functionalization disrupts the π-bonding system of single-walled carbon nanotubes by introducing saturated

sp^3 carbon atoms. Consequently, the electronic and transport properties of SWNTs change dramatically.[62]

As an alternative strategy, the noncovalent functionalization of carbon nanostructures was carried out more recently using various organic molecules via hydrophobic and/ or π-π stacking interactions.[62] The main advantage of these interactions is in the protection of the carbon nanostructure constitution, resulting in the optimal nanostructure properties.[62] However, in fluid systems, leaching of the noncovalently attached molecules is possible. Consequently, the application of these functionalized carbon nanostructures in liquid systems is not favorable.[62]

1.2.3. Nanostructures Fabrication Employing Biomaterials

In order to have soluble and biocompatible nanotubes, instead of modifying external part of CNTs, an alternative approach is employing biomaterials such as proteins and peptides as building blocks to self-assemble nanostructures.[43-51] It is known that proteins and peptides are inherently able to self-assemble into different structures such as elongated solid nanofibrils.[74-76] This may result in amyloid diseases [77-79] or nanostructures with potential applications ranging from tissue engineering to nanoelectronics [54,80-83]. There are various nanostructures in living systems such as microtubules, actin filaments, flagella, clathrin lattices[1], viruses and chromatins[2] formed by the self-assembly of biomolecules including nucleic acids, lipids and proteins.[84] For instance, microtubules,

[1] Clathrin is a protein playing a major role in the formation of coated vesicles (small bubbles within a cell).

[2] Chromatin is a combination of DNA and proteins making up the contents of the nucleus of a cell.

natural nanotubes with a diameter of 24 nm, are produced by the self-assembly of two kinds of proteins, tubulin α and β, in the presence of GTP[1].[85]

Various nanostructures such as fibers, tubes, rings, cages and polyhedrons are designed via self-assembly of different natural building blocks such as peptides [54,83], heme carrier protein 1 (HCP1) [86] and α-lactalbumin [87], along with engineered structures like flagella [88-90], pilins [44-48], viral capsids [49-51] and amyloid nanofibrils.[37] In this study, we are interested in pilin-based nanostructures.

1.2.3.1. Pilin-Based Protein Nanotubes (PNTs)

Recently, the development of pilin-based protein nanotubes has been reported.[44-48] G. F. Audette *et al.* employed an engineered type IV pilin to self-assemble protein nanotubes (PNTs).[45] Type IV pilins are monomeric subunits of type IV pilus (T4P), a flexible filament with a diameter of about 6 nm and a length of several micrometers produced at the poles of various bacteria.[45, 91] Pilins from all bacteria share similar amino acid sequences and structures, composed of a long α-helix and a β-sheet, wrapped around one end of the α-helix. The N-terminus of the α-helices is conserved in the interior part of the pilus, while the β-sheets are exposed on the outer surface.[44-48]

Fig. 1.5 shows the suggested model for type IV pilus assembled from K122-4 pilins. According to this model, K122-4 pilins form a helical structure with an outer diameter of approximately 52 Å, a helical pitch of 42 Å, and 5 pilin monomers per helical turn.[45]

[1] Guanosine-5'-triphosphate (GTP) is used as a source of energy for protein synthesis.

Even though the assembly of pilins to pili is not normally a spontaneous process, it is known that deletion of the last 28 amino acids of the α-helix of K122-4 pilins from bacterium *p. aeruginosa* results in water-soluble monomers which, in the presence of hydrophobic molecules in the solution, oligomerize to form nanotubes (Fig. 1.5C).[44-48] Fig. 1.6 shows a transmission electron microscopic (TEM) image of several truncated K122-4 (ΔK122-4) pilin-based protein nanotubes.

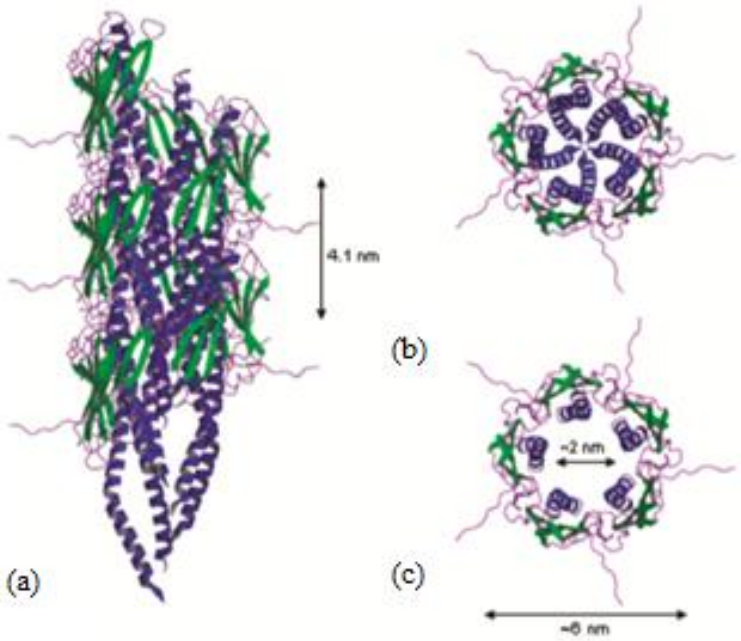

Fig. 1.5. Type IV pili and protein nanotubes. (a) Two turns of a type IV pilus assembled from K122-4 pilins. Type IV pili contain a 4.1 nm helical pitch and an outer diameter of ~6 nm. For each pilin monomer, the N-terminal α-helix, 4-stranded antiparallel β-sheet, and loop regions are shown in blue, green and purple, respectively. (b) Axial view of a single turn of the type IV pilus from a. The central core of the pilus is occupied by the N-terminus of α-helices of the pilin monomers. (c) Axial view of the protein nanotubes formed by ΔK122-4 pilin monomers. Deletion of the N-terminal α-helix in the pilin monomers results in an ~2 nm central channel. "Reprinted with permission from (Audette, G. F.; van Schaik, E .J.; Hazes, B.; Irvin, R. T. DNA-Binding Protein Nanotubes: Learning from Nature's Nanotech Examples. *Nano Lett.* **2004**, 4, 1897–1902). Copyright (2004) American Chemical Society."

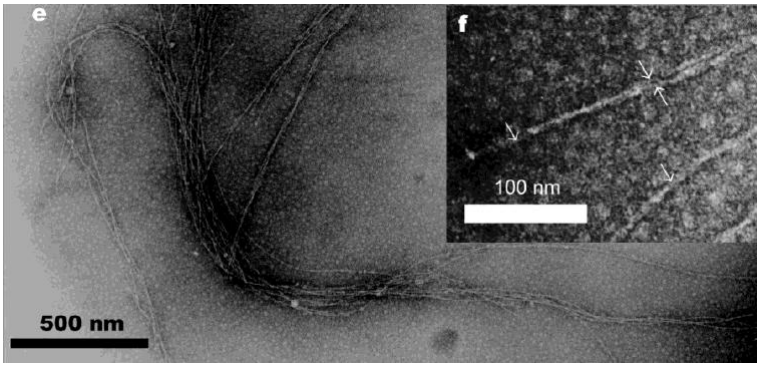

Fig. 1.6. Transmission electron microscope image of negatively stained purified *P. aeruginosa* pili. In this image the nanotubes have a diameter of ~6 nm. "Reprinted with permission from (Audette, G. F.; van Schaik, E. J.; Hazes, B.; Irvin, R. T. DNA-Binding Protein Nanotubes: Learning from Nature's Nanotech Examples. *Nano Lett*. **2004**, 4, 1897–1902). Copyright (2004) American Chemical Society."

1.2.3.2. Conductive Bionanostructures

While much research about bionanostructures has been conducted to address biological and medical needs [92], some employ the bionanostructures to fabricate various nonbiological nanostructures with applications in fields such as nano- or micro-electronics [93]. Various nanoscale metal and other inorganic wires are fabricated employing biological templates including proteins [11-14], peptides [37-42], nucleic acids (DNA and RNA) [94-96], bacteriophages[1] [97-100] and plant viruses [13,14].

For instance, E. Braun *et al.* employed complementary single-stranded DNA (ssDNA) to bridge two gold electrodes with a 12 μm distance.[94] Then, the double-stranded DNA (dsDNA) was formed and coated with silver to produce a wire with a diameter of 100 nm. Due to the polyanion structure of DNAs, the DNA bridge was loaded with silver ions, through Na^+/Ag^+ ion exchange, followed by Ag^+ reduction.

[1] Bacteriophages are viruses that infect bacteria.

As another example, tobacco mosaic virus (TMV) particles are one of the first bionano-templates used for the deposition of various inorganic materials.[13,14] S. Y. Lee *et al*. reported Pt deposition on the outer surface of engineered TMVs using hexachloroplatinate.[13] Platinum ions bind to the TMV cysteine residues. The cysteine residues, containing thiol, have particular affinity for Pt(II) ions. Then, reduction of the Platinum ions leads to the Pt cluster formation.

Knez *et al.* formed nickel and cobalt nanowire in the central channel of tobacco mosaic virus through activation of the virus inner surface with Pd(II).[11] Consequently, reduction of the palladium ions forms small palladium clusters that act as nucleation sites to deposit cobalt and nickel. Fig. 1.7 shows TEM image of a TMV particle after synthesis of a 3-nm cobalt nanowire in the central channel. Kobayashi *et al.* also employed the same technique to form a nanowire in the central channel of the tomato mosaic virus (ToMV).[12] They genetically modified ToMV to increase the number of lysine residues on the internal surface to generate more nucleation sites. Note that lysine is an N-donor residue with specific affinity for Pd(II).[12]

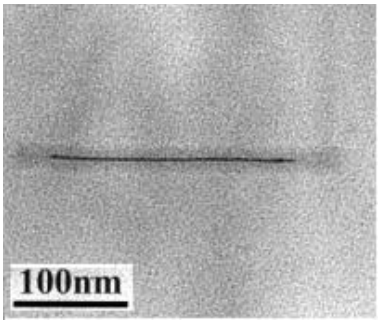

Fig. 1.7. TEM image of a TMV particle after activation with Pd(II) followed by electroless deposition of cobalt. "Reprinted with permission from (Knez, M.; Bittner, A. M.; Boes, F.; Wege, C.; Jeske, H.; Maiβ, E.; Kern, K. Biotemplate Synthesis of 3-nm Nickel and Cobalt Nanowires. *Nano Lett.* **2003**, 3, 1079-1082). Copyright (2003) American Chemical Society."

1.2.4. Characterization of Protein Self-Assembled Nanostructures

This section presents some examples of the techniques employed to characterize self-organized structures.

1.2.4.1. Atomic Force Microscopy (AFM)

An atomic force microscope (AFM) can be used in many different modes to characterize a number of parameters, ranging from outer-surface topography of a structure to its electrical conductivity.[101] Tapping and contact modes of AFM are explained in section 2.2.2.2. As an example of AFM applications, C. H. Clausen *et al.* employed electrostatic force microscopy (EFM) to determine whether a nanotube structure is hollow or not.[102,103] Through this technique, they compared hollow and silver-filled peptide-based nanotubes formed by self-assembly of diphenylalanine.

Initially, using a tapping-mode AFM, they scan a line with no bias between the surface and the tip. Subsequently, the tip is raised some nanometers above the surface. Employing a potential between the tip and the substrate (Fig. 1.8) and keeping the tip in constant distance, they used tapping-mode AFM to retrace the topography of the previous scan. During the second scan, the phase shift of the cantilever oscillation is monitored.

Because the distance between the tip and the surface is constant, it is assumed that the only force acting on the cantilever is the electrostatic force caused by the applied potential. The electrostatic force is proportional to the capacitance of the material present between the tip and the substrate located under the sample; consequently, the appearance of the phase shift signal is strongly dependent on the material of the sample and also on whether the sample is hollow or solid.[102,103]

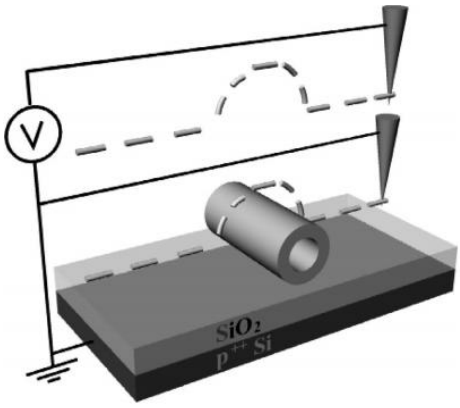

Fig.1.8. Principle of phase mode electrostatic force microscopy. Initially a topography line scan is made. Then, the tip is lifted and using a potential difference between the AFM tip and the backgate another line scan is made. "Reprinted with permission from (Clausen, C. H.; Jensen, J.; Castillo, J.; Dimaki, M.; Svendsen, W. E. Qualitative Mapping of Structurally Different Dipeptide Nanotubes. *Nano Lett.* **2008**, 8, 4066-4069). Copyright (2008) American Chemical Society."

1.2.4.2. Electron Microscopy

Electron microscopes, such as transmission electron microscope and scanning electron microscope (SEM), are commonly used to characterize self-organized structures. In addition to characterizing the geometry of the structure, which is the first starting point, TEM can verify whether the structure contains a cavity or a metal.[103] As will be explained in section 3.2.2.2, in TEM, high-energy electrons are transmitted through an ultra-thin specimen. The number of the electrons passing through each point of the sample is proportional to the density of the sample in the corresponding point.[101] For example, if the structure is hollow, the walls will be shown darker than the central part.

In SEM, a focused beam of electrons scans a sample to generate its image.[104] The electron-sample interaction produces different signals, containing information about the sample's surface topography and composition. SEM can be used in combination with other techniques to improve efficiency. For instance, Adler-Abramovich *et al.* combined

SEM with a hotplate to determine the thermal stability of the structure.[105] They heated the structure to a certain temperature and then imaged the sample by SEM to verify whether the sample was damaged or not.

1.2.4.3. Electrochemical Methods

Electrochemical methods are among the techniques used to characterize biological nanostructures.[106-108] For instance, G. Cunwang *et al.* employed cyclic voltammetry (CV) and electrochemical impedance spectroscopy (EIS) to investigate DNA self-assembly on 2-aminoethanethiol (AET) on a gold electrode under the controlled potentials of +1V and -1V.[109] EIS will be discussed in chapter 4. Fig. 1.9 shows the Nyquist diagram of bare Au, AET/Au and DNA/AET/Au obtained via impedance spectroscopy. The electrolyte contained $K_3Fe(CN)_6$ and $K_4Fe(CN)_6$ to investigate a faradaic process at the electrodes. The AET-modified electrode could not block the charge transfer activity of $[Fe(CN)_6]^{4-/3-}$ species, while DNA adsorption prevented it. The surface modified with DNA resulted in a larger semicircle in the Nyquist diagram under controlled potential of 0.1 V, compared to that of under controlled potential of -0.1 V. (Fig. 1.9) The larger semicircle represents a higher resistance to the charge transfer activity. This suggests higher degree of DNA self-assembly on the electrode at the more positive controlled potential.

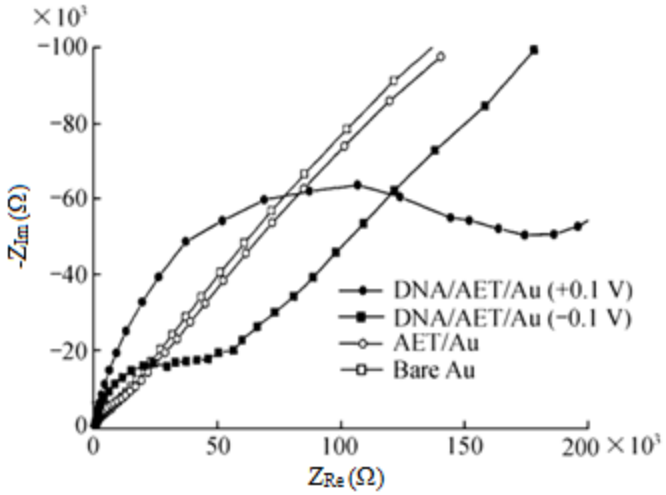

Fig. 1.9. Nyquist curves of bare Au, AET/Au and DNA/ AET/Au electrodes at ± 0.1 V control for 1 h. AC impedance was carried out by measuring the frequency range of 0.01 Hz -100 kHz. A 5 mV sinusoidal potential was applied to the electrode held at an open circuit potential. The electrolyte solution contained 1 mmol/L $K_3Fe(CN)_6$, 1 mmol/L $K_4Fe(CN)_6$ and 0.1 mol/L KCl. Reprinted from "Chinese Science Bulletin, 47, 2002, 370-375, Potential Control of DNA Self-Assembly on Gold Electrode, Cunwang, G.; Yibin, T.; Jianhui, L.; Yu, Z.; Haiqian, Z.; Ning, G., Figure 4, Copyright (2002); with kind permission from Springer Science and Business Media."

1.2.4.4. Matrix-Assisted Laser Desorption/Ionization Mass Spectrometry (MALDI-MS)

Matrix-assisted laser desorption/ionization (MALDI) is a soft ionization technique used in mass spectrometry. Fragile molecules such as biomolecules and large organic molecules can be investigated via this technique. The most common method is to deposit a droplet of the analyte-matrix mixture on the MS sample stage, followed by drying the spot at room temperature to co-crystallize the matrix and the analyte.[110] Compounds such as sinapinic acid[1] with a reasonably low molecular weight, strong optical absorption

[1] 3,5-dimethoxy-4-hydroxycinnamic acid

(in either UV or IR range), and acidic properties (to act as a proton source to promote ionization of the analyte) are employed as the matrix.

This experiment comprises two steps. At first, desorption of the matrix material is triggered by a UV laser beam that leads to formation of a hot stream containing neutral and ionized matrix molecules, matrix clusters, and nanodroplets. Consequently, in this hot stream, the analyte molecules are ionized (protonated or deprotonated). Finally the analyte is analyzed by mass spectroscopy, which separates the ions according to their mass-to-charge ratio. In this technique, typically, ions are accelerated and then separated in a magnetic field.

1.2.4.5. Surface-Enhanced Laser Desorption Ionization (SELDI)

Surface-enhanced laser desorption ionization (SELDI) is a variation of MALDI. In MALDI, the analyte and matrix are co-crystallized at the MALDI plate, which is not selective. In contrast, in SELDI, a complex mixture (e.g., crude biological samples) is spotted directly on a functional surface with selective adsorption.[111,112] Some proteins in the sample bind to the surface, while the others are removed by washing. Subsequently, the matrix is applied to the surface and allowed to crystallize along with the adsorbed materials.[112] Then, the components, which are retained by the surface, can be identified by mass spectroscopy.

Binding to the SELDI surface acts as a separation step. This method of on-probe washing of the sample spot could be enough to decrease the sample complexity and remove the components that could prevent efficient ionization of the proteins (e.g., buffer salts and detergents).[111]

1.3. Monolayer Self-Assembly

Self-assembly of monolayers (SAMs) allows us to tailor the interfacial properties of metals, metal oxides and semiconductors. SAMs with desired properties such as hydrophobicity or acidity are employed to investigate protein adsorption or self-assembly. In this section, we will have a brief explanation of two types of surface modification. These two methods will be discussed in more detailed in chapter 2 and chapter 3.

1.3.1. Self-Assembled Monolayers on Single-Crystal Silicon

Self-assembled monolayer on a single-crystal silicon wafer is a commonly used substrate to investigate protein adsorption.[113-117] This self-assembly, described as the addition of a Si-H to an unsaturated bond, is carried out via hydrosilylation. In advance of the hydrosilylation reaction, the Si wafer, which is covered by SiO_2, is etched to produce a H-terminated Si(111) surface. 40% NH_4F in water is a frequently used etchant. Fig. 1.10 represents the reaction of 1-alkenes with a hydrogen-terminated silicon surface. Protein adsorption at modified silicon surfaces is studied via methods such as MALDI-MS [111,116,117], SELDI [118,119] and AFM [120,121].

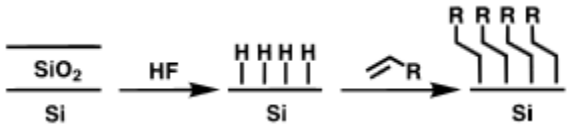

Fig. 1.10. Schematic illustration of the reaction of 1-alkenes with H-terminated silicon surface. "Reprinted with permission from (Sieval, A. B.; Demirel, A. L.; Nissink, J. W. M. ;Linford, M. R.; van der Maas, J. H.; de Jeu, W. H.; Zuilhof, H.; Sudholter, E. J. R. Highly Stable Si-C Linked Functionalized Monolayers on the Silicon (100) Surface. *Langmuir*. **1998**, 14, 1759-1768). Copyright (1998) American Chemical Society."

1.3.2. Alkanethiol Self-Assembled Monolayers on Au(111)

Self-assembled monolayers can also be formed as a result of alkanethiol adsorption on gold. Thiols have high affinity for the surface of gold, silver, copper, palladium, platinum and mercury, forming self-assembled monolayers with desired chemical functionalities displayed at the exposed interface.[122]

Because of the semicrystalline, ultrathin and homogeneous structure of alkanethiol SAMs, the films have reproducible electronic properties.[123] These properties, along with the conductivity of gold, allow us to use gold electrodes modified by alkanethiol SAMs to investigate the effects of monolayer thickness and functional end-group by electrochemical methods.[123-127] Electrochemical methods are also employed to investigate the adsorption of materials such as proteins [128,129] and DNA [108,130] onto SAM on gold. Moreover, the SAM flatness allows to investigate the protein self-assembly or adsorption by instruments such as AFM and scanning tunneling microscope (STM).[131,132]

1.4. Scope and Origin of the Research

The present work involves the study of protein adsorption and protein nanostructure self-assembly at modified surfaces. We were also interested in producing a new conductive nanostructure. The main goal of the first section of this research was to investigate the relationship between the intensity of MALDI-MS signals and protein adsorption. We were interested in finding whether an intense signal in the MALDI-MS spectra is a

measure of protein concentration, or it may occur because of a weak protein-substrate interaction.

Initially, AFM allowed us to compare bovine serum albumin (BSA) and insulin coverage at methyl- and ester-terminated surfaces. Then, we compared our findings with the results obtained using MALDI-MS [111].

The main goal of the second section was to invent a new protein nanostructure. The recent discovery of ΔK122-4 pilin-based protein nanotube [44-48], along with the fact that the self-assembly of the engineered pilins is triggered by hydrophobic molecules in solution, prompted us to investigate the possibility of directing the growth of such material at a surface with an appropriate hydrophobicity. This approach would allow us further chemical or physical modifications without losses of the sample. Moreover, because pilin-base PNTs are able to bind at both biotic and abiotic surfaces, and they can also stick together, surface-initiated PNTs would be easier to handle.

Several facts, such as the ability of ΔK122-4 pilin-based PNT to bind DNA [45,48,133], and the high sequence variation of different pilins [45,48,133] suggest that the surface-derived pilin-based nanostructures may be useful in a variety of nanotechnology applications including biosensing, bioseparation and bionanoelectronics.

In order to develop the application of the surface-derived nanostructures, several modifications are possible. Binding a specific sequence of amino acids at the surface can introduce binding sites for specific ligands. Considering the ability of ΔK122-4 PNT to capture ssDNA and dsDNA non-specifically [45], the attached DNA can be biotinylated [45] to target specific molecules with the goal of developing sensors. Moreover,

introducing histidine amino acids to engineered K122-4 pilins facilitates metal deposition at or in the self-assembled protein nanostructure with potential applications in nanoelectronics.

We carried out ΔK122-4 pilin self-assembly at different modified surfaces to investigate the effect of surface hydrophobicity on pilin oligomerization. Surface modifications were examined via FT-IR spectroscopy. In addition to AFM, which gave us an insight to compare the appearance of the layers formed by ΔK122-4 pilins at hydrophobic and hydrophilic surfaces, we also employed electrochemical impedance spectroscopy to investigate the layers. Our goal was to see if the layer formed at the hydrophobic surface is a well-packed and structured layer or it is formed by pilin aggregation.

We also aimed to develop a conductive nanowire with possible applications in bionanotechnology. ΔK122-4 pilin-based PNTs were employed as a template for electroless copper deposition. In order to investigate the metal deposited PNTs, TEM was used.

1.5. Outline of the Thesis

This dissertation includes six chapters. Chapter one comprises the introduction, and the scope and origin of the thesis. The results are presented in four chapters, each of which has its own introduction, experimental part, results and discussion, and conclusion. Chapter two describes bovine serum albumin and insulin adsorption at Si(111) surfaces modified with 1-decene or methyl 10-undecenoate. Chapter three deals with ΔK122-4 pilin-based nanoweb fabrication. Type IV pilins from bacterium *Pseudomonas*

aeruginosa are used as building blocks. Chapter four reports the investigation of pilin self-assembly at different surfaces, employing electrochemical impedance spectroscopy. Chapter five elaborates on copper electroless deposition (ELD) at ΔK122-4 pilin-based PNTs. Finally, a summary of this research is presented in chapter six.

Chapter 2: Protein Adsorption at Modified Silicon Surfaces

2.1. Introduction

Due to the importance of protein adsorption in biological process, the adsorption of proteins at a solid–liquid interface is the subject of a wide range of studies.[1-13] In this Chapter, protein adsorption is reported in the context of applications of modified or unmodified porous [11,12] and crystalline [13] silicon substrates for direct readout of adsorbed protein by MALDI-MS. These applications have demonstrated enhanced protein detection signal from the background signal when these substrates were employed.

In this study, crystalline silicon surfaces terminated by methyl and ester groups are employed. Crystalline silicon is very flat, well-defined, and can be modified easily using simple chemistry to produce a stable solid base for protein adsorption study. Flatness of the surface facilitates quantification of the protein adsorption by AFM. Via a hydrosilylation reaction, very stable silicon-carbon bonds form, resulting in a dense monolayer.[13-18] This surface modification can introduce various terminal groups that can control the hydrophobicity, acidity and chemistry of the surface.[13-17]

We employed modified silicon substrates to investigate protein adsorption by AFM. We were interested in learning about the relationship between the protein coverage measured by AFM and its correlation to signal intensities observed by MALDI-MS from an earlier study [13]. This would help to understand whether a weak MALDI-MS signal is due to

the low quantity of the protein, or it may occur because of strong attachment to the substrate.

2.1.1. Silicon Surface Modification

Functionalization of hydrogen-terminated Si(111) surface can be performed through a hydrosilylation reaction with ω-functionalized 1-alkenes (or 1-alkynes) using different methods such as thermal, photochemical, radical-initiated, and Lewis acid processes.[13-18] Fig. 2.1 shows the proposed mechanism by Louis *et al.* for the thermal hydrosilylation reaction.[19]

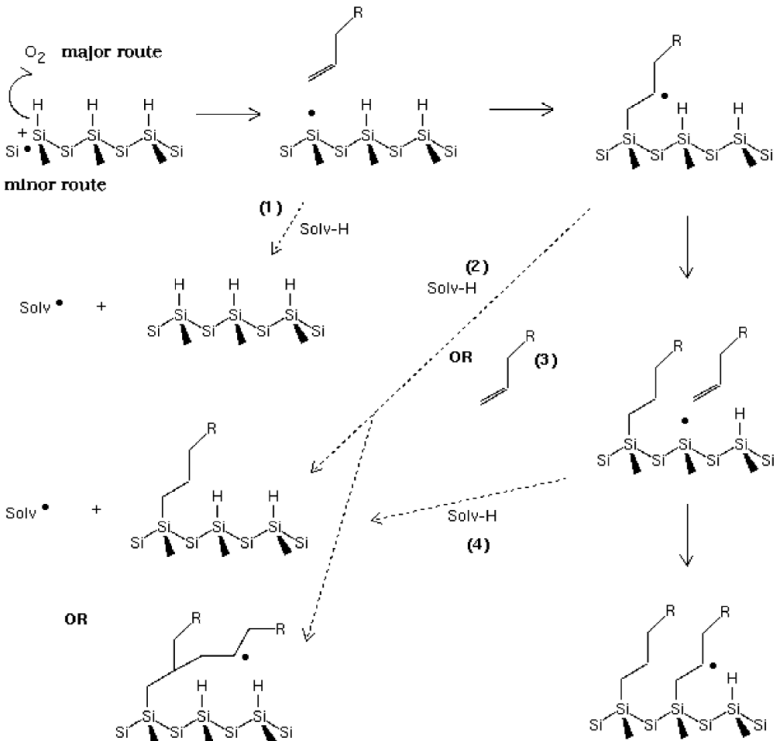

Fig. 2.1 Thermal hydrosilylation reaction to form an alkyl monolayer on H-terminated silicon, proposed by Louis *et al*. "Reprinted with permission from de Smet, L. C. P. M.; Zuilhof, H.; Sudholter, E. J. R.; Lie, L. H.; Houlton A.; Horrocks, B. R. Mechanism of the Hydrosilylation Reaction of Alkenes at Porous Silicon: Experimental and Computational Deuterium Labeling Studies. *J. Phys. Chem. B.* **2005**, 109, 12020-12031. Copyright (2005) American Chemical Society."

Prior to surface modification, the Si(111) substrates are chemically etched to remove the surface oxide and produce atomically flat H-terminated surfaces to be investigated by AFM. This process alters the surface morphology of the silicon thoroughly. The use of 40% NH_4F in water (free from oxygen gas) is a common method of etching.[20] It is known that an aqueous solution of HF with pH around 9-10 produces Si(111) surfaces, ideally terminated with silicon monohydride (75% SiH) oriented normal to the surface. The surface was shown to be very homogeneous with a low defect density (<0.5%).[20]

Fig. 2.2 demonstrates the different sites of a Si(111) surface. The surface morphology of an etched Si(111) surface is the result of competition between two types of reactive sites in close-packed steps, the close-packed step site and the kink site.[21] In kink-site etching, one step site is etched and two kink sites are nucleated. When repeated many times, kink etching removes a single row of atoms from the step edge. This process tends to decrease the surface roughness. On the other hand, etching into the close-packed steps increases the surface roughness.

The final roughness of the surface depends on the anisotropy of the etchant, i.e., the ratio of kink etching rate to the step etching rate. An anisotropic etchant, such as NH_4F(aq) is highly site-selective and attacks defects on the Si(111) surface (e.g., steps and kinks), while leaving the perfect surface (the close-packed plane) basically intact.

On Si(111), there are two principal miscuts (i.e., close-packed step directions). Surface miscut towards the $<1\bar{1}2>$ and $<\bar{1}12>$ directions have monohydride-terminated and dihydride-terminated steps, respectively. (Fig. 2.2) Due to the threefold symmetry of the surface, each type of miscut has three equivalent steps with an angle of 60°.[21]

The structure and density of the steps of an etched silicon surface are affected by the surface miscut and its magnitude, respectively.[21] Etching of a Si(111) surface with a miscut toward the $<\bar{1}\bar{1}2>$ direction (dihydride-terminated) produces step edges with a shark teeth pattern, while a miscut toward the $<1\bar{1}\bar{2}>$ direction (monohydride-terminated) results in straight step edges. On the other hand, etching of a surface with a bigger miscut results in a higher step density.

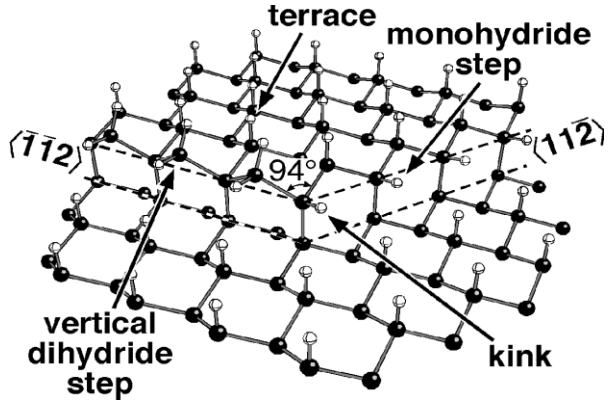

Fig. 2.2. Atomic structure of a H-Si(111) surface. The dark and light spheres represent silicon and hydrogen atoms, respectively. The vertical dihydride and kink sites are severely strained by interactions with the hydrogen atom on the terrace below. "Reprinted with permission from (Hines, M. A. The Picture Tells the Story: Using Surface Morphology to Probe Chemical Etching Reactions. *Int. Rev. Phys. Chem.* **2001**, 20, 645-672). Copyright (2001) Taylor and Francis."

In order to study protein adsorption, we functionalized H-terminated n-type Si(111) surfaces with 1-decene and methyl 10-undecenoate. Bovine serum albumin and insulin were chosen as protein adsorbates. We compared our results with the MALDI-MS spectra of the work previously accomplished by Professor Morin's group. [Fig. 2.3] We were interested in figuring out whether the lack of MALDI-MS BSA signal is due to a low BSA adsorption or to a strong attachment of BSA to the surface.

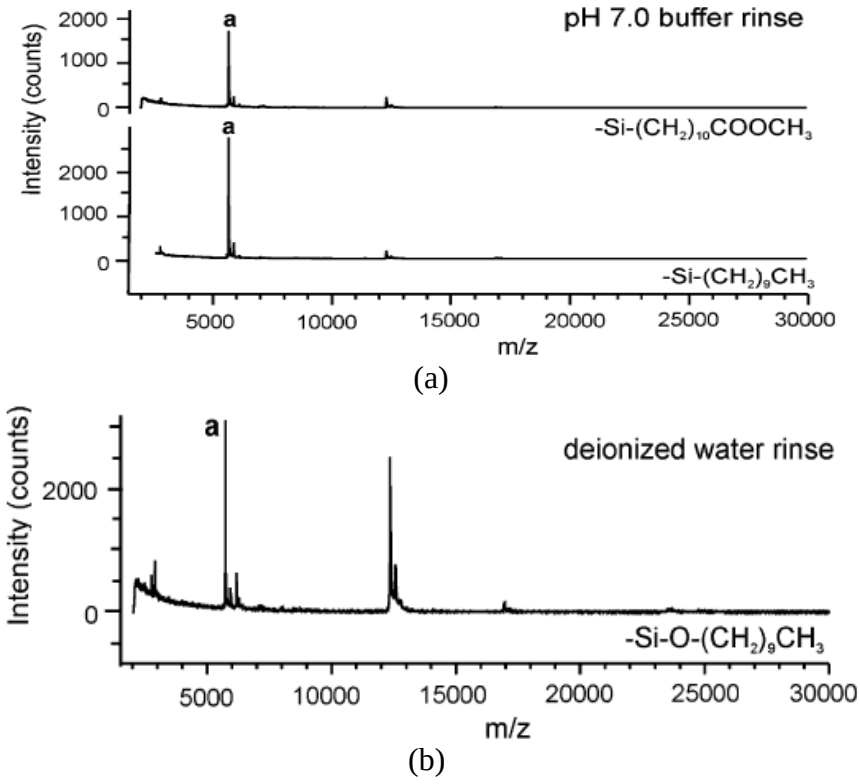

Fig. 2.3. Mass spectra of a mixture of eight proteins (BSA, insulin, cytochrome, lactalbumin, myoglobin, ubiquitin, casein and carbonic anhydrase) (a) on methyl- and ester-functionalized silicon substrates after rinsing with a pH 7.0 buffer, and (b) on a methyl-terminated silicon substrate after rinsing with deionized water. Detected signal related to insulin is shown by a. BSA was not detected. "Reprinted from Journal of Chromatography A, 1135, Mengistu, T. Z.; DeSouza, L.; Morin, S. Probing Proteins on Functionalized Silicon Surfaces Using Matrix-Assisted Laser Desorption/Ionization Mass Spectrometry, 9 pages, Copyright (2006), with permission from Elsevier."

2.1.2. Insulin

Insulin, with a molecular weight of 5.8 kDa and isoelectric point of 5.4, [22] may be regarded as a spherical molecule with the diameter of 2.3 ± 0.1 nm [23]. Insulin includes two peptide chains (A and B).[24, 25] In most species, chain A and chain B consist of 21 and 30 amino acids, respectively.[24] As shown in Fig. 2.4a, each monomer has three cystine disulfide bonds. Two disulfide bonds connect the A and B chains and the third

one exists within the A chain.[24-26] The structure of insulin is mostly conserved in the animal kingdom.[25] Each of the A and B chains have two acidic residues and one carboxylate end group.[24,27]

In aqueous solution, insulin has a high tendency to form dimers, tetramers and hexamers.[25,28] The dimer formation takes place because of antiparallel association of the C-terminus of the B chains containing several hydrophobic residues.[25] The main driving force for the dimerization is interaction between extremely hydrophobic groups, e.g., phenylalanine, tyrosine and valine. Insulin dimerization forms a hydrophobic core in the monomer-monomer interface of the dimer.[28] This interface resembles a drop of oil in a very polar and hydrophilic environment. Four hydrogen bonds are formed between the two monomers.[24,27,28] However, because H bonding between protein and water molecules is stronger than the one formed between the two proteins, the hydrogen bonds do not stabilize the dimer. Fig. 2.4b demonstrates an insulin dimer.

The self-association constants of insulin depend on the experimental conditions, e.g., pH, ionic strength, temperature, and concentration of metal ions like Zn^{2+} or certain compounds such as m-cresol and phenol.[25,29,30] At pH 2 and ionic strength of 0.05, the following values are reported for dimerization and tetramerization constants.[29] I represents insulin.

$$I + I \rightleftarrows I_2 \qquad K_{f2} = 7.95 \times 10^3\ M^{-1} \qquad (1)$$

$$I_2 + I_2 \rightleftarrows I_4 \qquad K_{f4} = 3.1 \times 10^2\ M^{-1} \qquad (2)$$

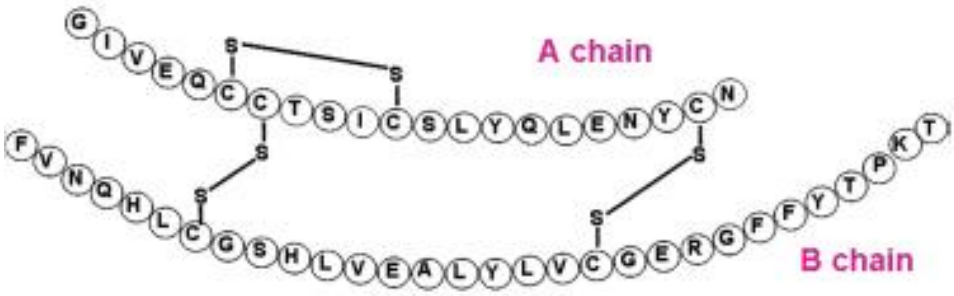

	A8	A9	A10	B30
Human	Thr	Ser	Ile	Thr
Porcine	Thr	Ser	Ile	Ala
Bovine	Ala	Ser	Val	Ala
Sheep	Ala	Gly	Val	Ala

(a)

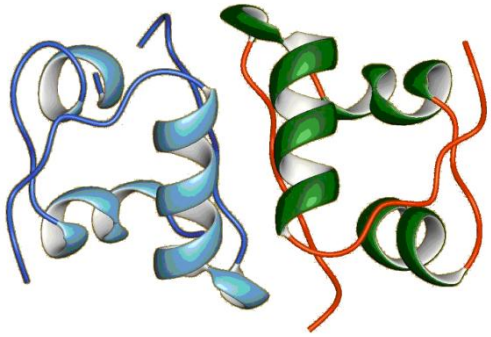

(b)

Fig. 2.4. (a) Amino acid sequence and disulfide bonds of human, porcine, bovine and sheep insulin. (b) Molecular model of insulin dimers. "Reprinted from (Mayer, J. P.; Zhang, F.; DiMarchi, R.D. Biopolymers, Insulin Structure and Function, 88, 5, 687–713, DOI: 10.1002/bip.20734, http://onlinelibrary.wiley.com/doi/10.1002/bip.20734/full), Copyright (2006), with permission from John Wiley and Sons."

At pH ranging from 7 to 11, the net charge of insulin varies from -2 to -6; therefore, in the center of dimerization (the C-terminus of the B chains), electrostatic repulsion between ionized amino acid residues prohibits the dimerization. An increase of pH from 2.0 to 11.2 reduces the dimerization constant sixfold, and a pH change from 11.2 to 12.7

decreases it another 20 times.[25] Both insulin hexamer and monomer adsorb more strongly and more irreversibly at hydrophobic than hydrophilic surfaces.[24,31]

As a consequence of the small size of insulin, most residues are solvent accessible.[31] Using liquid affinity chromatography, H. Lakhiari and his colleague have investigated insulin adsorption on coated silica-based supports, grafted with N-acetylglucosamine.[25] They studied the influence of different parameters, such as insulin and NaCl concentration, as well as pH, on insulin retention time. It was observed that with increasing the salt concentration in the solution, the quantity of adsorbed insulin decreases. Therefore, it was concluded that ionic interactions between insulin and the stationary phase are very weak, and insulin adsorption is the result of hydrophilic, hydrophobic and weak ionic interactions.[25]

High insulin adsorption onto hydrophobic surfaces, even in the case of electrostatic repulsion, indicates that the insulin adsorption is dominated by non-electrostatic interactions, which are assisted by surface dehydration.[30] It is conceivable that involvement of the C-terminus of the B-chain exposes the hydrophobic part of the molecule that is normally buried in the interior part of insulin monomers. In the presence of opposite charges, hydrophobic interactions are assisted by electrostatic interactions. Upon adsorption at a hydrophobic surface, the secondary structure of insulin changes, i.e., the α-helix reduces and the amount of disordered structures (coils) increases.[30]

2.1.3. Bovine Serum Albumin

We also investigated the adsorption of bovine serum albumin onto modified silicon surfaces. Albumins are highly soluble in water, and their aqueous solution is very stable

(specially the frozen solution). However, albumin coagulates with heat.[32] BSA with a molecular weight of about 66 kDa is a large protein which consists of about 583 amino acid residues.[33] The tertiary structure of BSA consists of nine loops stabilized by seventeen internal disulfide bonds that organize the molecule into three similar structural domains, each of which is divided into two subdomains. [34,35]

Native BSA is a heart-shaped molecule which can be approximated to an equilateral triangle with sides of 8 nm and a thickness of 3 nm (Fig. 2.5a).[36-38] It is suggested that BSA keeps its native structure (N form, Fig. 2.5b) with a molecular volume of about 88.25 nm^3 in the pH range from 4.5 to 8.[35] At pH 4-4.5, a reversible unfolding results in a more elongated shape (~4 nm×12.9 nm, F form, Fig. 2.5c).[35] Bellow pH 4, further unfolding leads to a fully extended structure known as the E form. (Fig. 2.5d)

BSA, with isoelectric point of 4.7, is comprised of both positively and negatively charged parts, as well as hydrophobic regions.[34,39] The primary structure of BSA is not charged evenly. At neutral pHs, the net charges of domains I, II and III of BSA are -10, -8 and 0, respectively.[40] However, the tertiary structure of BSA (Fig. 2.6) shows an almost uniform distribution of charges.[41]

Exposure of hydrophobic residues assists BSA adsorption onto hydrophobic surfaces. Even though BSA has an affinity to adsorb onto both hydrophobic and hydrophilic surfaces, it has a much higher binding affinity toward the former.[42] When adsorbed onto hydrophobic surfaces, BSA loses some ordered structure and spread at the surface which results in a lower density of adsorption.[42] Fig. 2.7 shows a schematic

representation of the conformational change of BSA due to adsorption onto a hydrophobic surface.

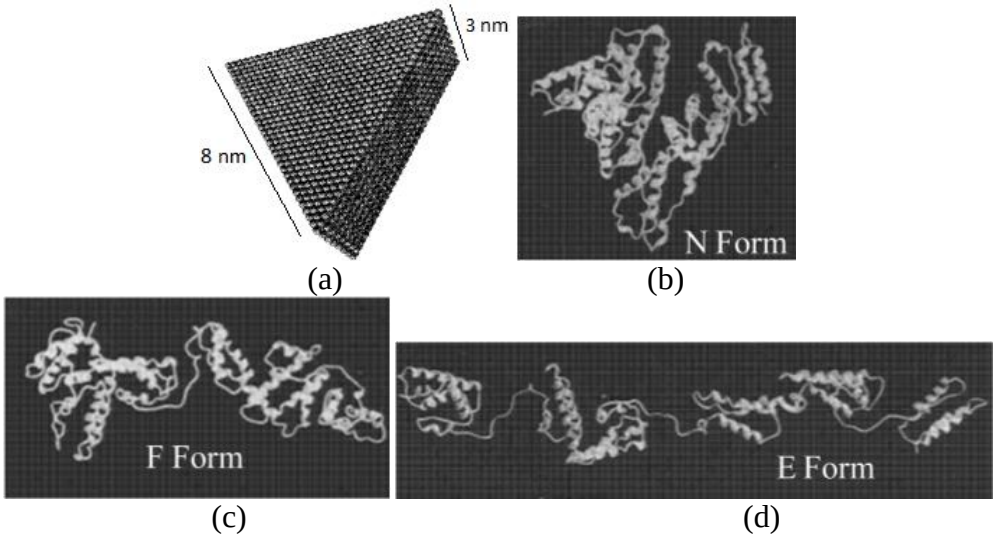

Fig. 2.5. (a) Rough shell triangular model of BSA with dimension of 80 × 80 × 80 × 30 Å. “Reprinted from Biophysical Journal, 80, Ferrer, M. L.; Duchowicz, R.; Carrasco, B.; de la Torre, J. G.; Acuna, A. U., The Conformation of Serum Albumin in Solution: A Combined Phosphorescence Depolarization-Hydrodynamic Modeling Study, 9 pages, Copyright (2001), with permission from Elsevier.” (b) Principal structures of normal conformation (N form, pH 4.5-8), (c) fast conformation (F form, pH 4.5-4), and (d) the fully extended structure (E form, below pH 4) of serum albumin. “Reprinted from Advances in Protein Chemistry, 45, Carter, D. C.; Ho, J. X., Structure of Serum Albumin, 51 pages, Copyright (1994), with permission from Elsevier.”

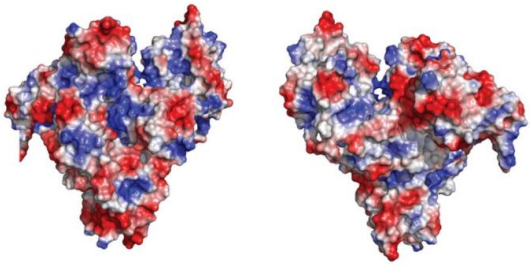

Fig. 2.6. Surface charge distribution of BSA. (a) Domain I is on the left, and domains II and III are arranged anticlockwise. (b) Domain I is on the right, and other domains are arranged clockwise. "Reprinted with permission from (Bujacz A. Structures of Bovine, Equine and Leporine Serum Albumin. *Acta Crystallogr. D Biol. Crystallogr.* **2012**, 68, 1278-1289). Copyright (2012) Crystallography Journals."

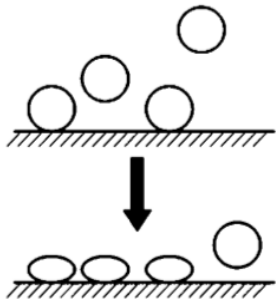

Fig. 2.7. Schematic representation of the BSA conformational change upon adsorption onto a hydrophobic surface. "Reprinted with permission from (Roach, P.; Farrar, D.; Perry, C. C. Interpretation of Protein Adsorption: Surface-Induced Conformational Changes. J. Am. Chem. Soc. **2005**, 127, 8168-8173). Copyright (2005) American Chemical Society."

2.2. Experimental and methodology

2.2.1. Materials and Reagents

Single side polished n-type Si(111) wafers (miscut by ± 0.5°, doped with phosphorus, 0.02- 0.5 Ω cm resistivity) from Virginia Semiconductor (Fredericksburg, VA, USA) were used in this study. Si(111) ATR substrates (n-type, 25 mm × 4.5 mm × 1 mm, 45°) were obtained from Harrick Scientific Corporation. 1-Decene (94%) and methyl 10-undecenoate (96%) were purchased from Aldrich. Ultra pure grade chemicals were used to clean and etch the silicon samples: ULSI (ultra large-scale integration) grade hydrogen peroxide (30%) and ammonium fluoride (40%) were from Honeywell, and sulfuric acid (96%) was purchased from GEM Microelectronic Materials (Arizona, USA). Ultrapure water (Millipore, 18 M Ω cm, 1 μg/L total oxidizable carbon (TOC)) was used to rinse

surfaces and prepare solutions. The BSA (≥ 96%) and insulin (potency ≥ 29.1 USP[1] unit/mg (HPLC) [2]), used to study protein adsorption, were from Sigma.

2.2.2. Instrumentation

2.2.2.1. ATR-FTIR

A Nexus 870 Spectrometer (ThermoNicolet) equipped with 4X Beam Condenser (Harrick Scientific Corporation) was employed to collect attenuated total reflection-Fourier transform infrared (ATR-FTIR) data with 0.96 cm^{-1} resolution. The instrument was purged with dry air half an hour before and while measurement.

An IR beam passes through a crystal and reflects from the internal walls several times to form an evanescent wave (Fig. 2.8).[43] At each reflection, the evanescent wave[3] penetrates a few micrometers (0.5-5 µm) to the sample which is adsorbed onto or held in contact with the outer surface of the crystal.[43] Then, the spectrum of the beam is collected by a detector to reveal structural and quantitative information about the sample. Silicon is one of the most commonly used materials for ATR crystals.[43]

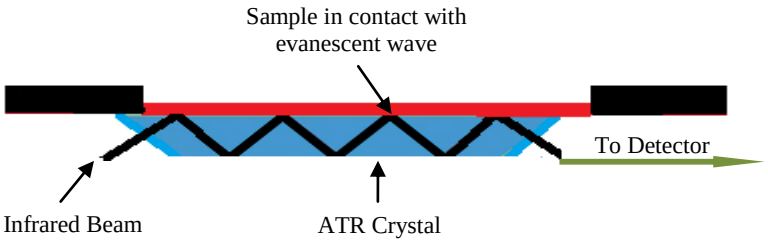

Fig. 2.8. Schematic representation of attenuated total reflectance through a crystal.

[1] According to U.S. pharmacopia convention

[2] Measured by HPLC (high performance liquid chromatography)

[3] An evanescent wave is a near-field standing wave with an intensity that exponentially decays with distance from the boundary at which the wave was formed.

2.2.2.2. AFM

A commercial AFM instrument (Dimension 3100, NanoScope IIIa, Digital Instrument, USA) was employed to perform topographic measurements of the etched and functionalized silicon samples before and after protein adsorption. AFM probes were purchased from Veeco. Imaging was carried out under atmospheric air in tapping and contact modes. A common gray scale is used for AFM images. Lowest and highest features are shown by darkest and lightest parts, respectively. A width and height scale is specified with each figure. Image SXM software was used for volume analysis of BSA adsorbed at the modified surfaces. The method mentioned by Ratcliff and Erie was employed to calculate the volume of the aggregates.[44]

An AFM probe consists of a microscopic tip attached to the end of an elastic cantilever. The tip diameter is a few nanometers (typically ca. 10 nm). The cantilever is usually made of silicon or silicon nitride and is attached to a piezo electric ceramic tube. While scanning in contact mode, a split photodiode detector monitors the changes of the cantilever deflection.[45] When the cantilever is pushed against the sample, a force is exerted to the tip, resulting cantilever deflection. A feedback loop maintains the cantilever deflection at the desired value by inserting a voltage to the piezoelectric to raise or lower the scanner at each x, y data point.[45] The applied voltage is a measure of the height of the features on the sample surface.

Tapping-mode AFM operates by scanning a tip attached to the end of an oscillating cantilever across the sample surface.[45] The frequency of the oscillating cantilever is at or slightly less than the resonance frequency of the cantilever.[45] The oscillation

amplitude is in the range of 20-100 nm.[45] Protrusions or holes on the surface increase or decrease the interactions between the tip and the surface, respectively. These interactions change the cantilever amplitude. As shown in Fig. 2.9, a feedback loop maintains the amplitude or frequency to reach the set point by lifting or lowering the tip. The vertical movement of the scanner is used to form a topographic image.[45]

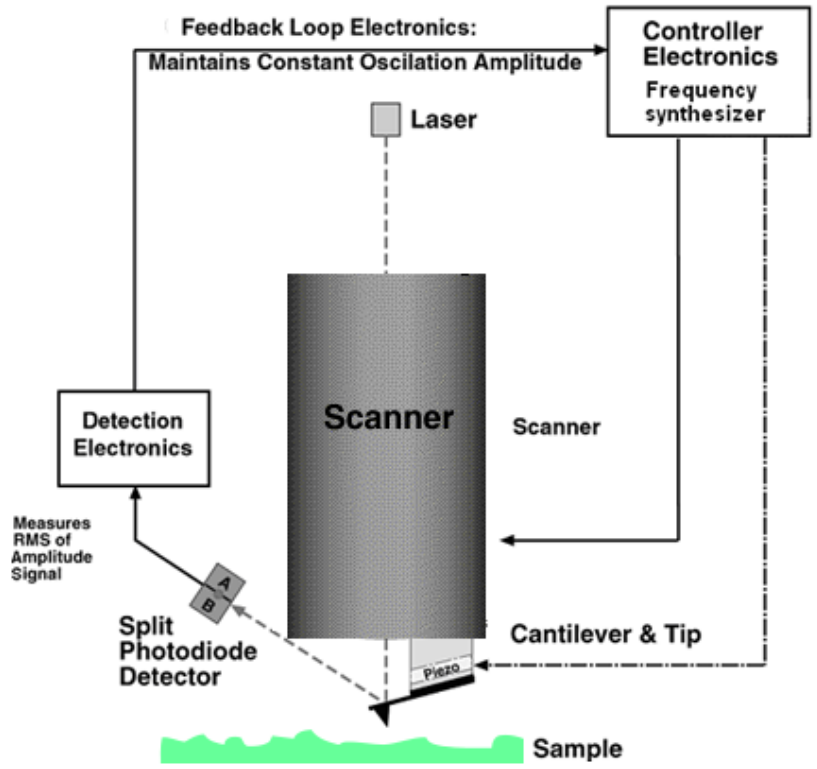

Fig. 2.9. Schematic representation of a tapping-mode AFM. Feedback loop maintains a constant cantilever deflection.

2.2.3. Sample Preparation

Single side polished n-type silicon wafers were cut into pieces of approximately 14 mm × 40 mm in size. Then the samples were cleaned, etched, functionalized and used for protein adsorption investigation. After each step, the samples were imaged by AFM.

A hot (~90ºC) mixture of H_2SO_4 (96%) and H_2O_2 (30%) (1:1, v:v) was employed to clean the silicon wafer samples. The samples were cleaned in a PTFE vial for 30 min. The PTFE vial was also cleaned in the same way before each usage. Then, the solution was discarded and the samples were rinsed with a copious amount of water from the Millipore system in the same vial.

To prepare an atomically flat H-terminated Si(111) surface, a silicon sample was dipped into 40% deoxygenated aqueous NH_4F solution for 30 min. The solution was bubbled with argon for 30 min before etching. The reaction was carried out in a PTFE vial under argon flow without disturbing the solution.

After etching, the surface was immediately functionalized to prevent oxidation. Thermal functionalization with 1-decene and methyl 10-undecenoate was performed at 150°C and 115°C, respectively. A lower temperature was employed for methyl 10-undecenoate because it is degraded at higher temperatures as shown by a change in its color. The reaction was performed under argon flow in a Schlenk tube for 23 h. The Schlenk tube was cleaned in hot 96% H_2SO_4, rinsed with deionized water, and dried in an oven. Before each usage, the reagents were argon-purged for 30 min to be free of oxygen. Deionized water, anhydrous ethanol, tetrahydrofuran and carbon tetrachloride were used to rinse the functionalized substrates. In order to characterize the surfaces by ATR-FTIR, Si(111) ATR elements were used. The ATR samples were prepared using the same method described for the silicon wafer samples. An average of 100 scans at 0.96 cm^{-1} resolution was used to record the spectra. To prepare a carboxylic acid-terminated surface, a H-terminated Si(111) ATR element was thermally functionalized with methyl 10-

undecanoate. Then, the surface was hydrolyzed in 2.4 M HCl (aq.) at 70 °C for 2 h. A freshly etched Si(111) ATR substrate was used as reference background.

Saturated (~0.1 mg/mL) and 10% saturated (~0.01 mg/mL) insulin solutions, and 1.0, 0.2 and 0.01 mg/mL BSA solutions were used to investigate protein adsorption. These concentrations were chosen to compare the results obtained via our AFM imaging with MALDI-MS spectra from a previous work [13]. In the latter experiment, 10% saturated insulin and 1 mg/mL BSA solutions were used. Functionalized silicon surfaces were treated with protein solutions for about 30 seconds. Then the samples were rinsed with plenty of deionized water and blow dried with nitrogen gas prior to further characterization.

2.3. Results and Discussion

This section is structured as (a) modification of Si(111) substrates with 1-decene and methyl 10-undecenoate, (b) investigation of BSA and insulin adsorption at the modified surfaces employing AFM, (c) volume analysis of BSA adsorbed at 1-decene- and methyl 10-undecenoate-modified surfaces using AFM images, and (d) comparison of the results with the protein adsorption measurements of the work done by T. Z. Mengistu *et al.* using MALDI-MS [13].

In this research a tapping-mode AFM was employed to investigate the surfaces before and after BSA and insulin adsorption. This method is adopted because in contact-mode imaging, the AFM tip swipes the surface and can remove some adsorbed proteins; therefore, it was necessary to perform imaging in tapping mode. To illustrate this point,

Fig. 2.10a and 2.10b compare tapping and contact modes AFM images of BSA adsorption at a carboxylic acid-terminated surface. Due to the removal of material from the surface during scanning, the contact-mode image shows much less protein adsorption.

2.3.1. Surface Modification

In order to investigate BSA and insulin adsorption at methyl- and ester-terminated surfaces, n-type Si(111) substrates were modified with 1-decene or methyl 10-undecenoate. AFM and infrared spectroscopy were used to investigate the layers. Prior to hydrosilylation, the substrates were chemically etched to produce hydrogen-terminated Si(111). Fig. 2.11a and 2.11b show 1 μm × 1 μm and 5 μm × 5 μm contact-mode images of n-type Si(111) etched in 40% aqueous NH_4F. The images reveal atomically-flat terraces of a H-terminated Si(111) substrate. The height of the steps (0.31 ± 0.04 nm) is in agreement with the value of 0.314 nm reported for the atomic steps for the same type of crystal [46].

40% aqueous NH_4F, containing HF at pH around 9-10 [20], removes silicon atoms through sequential oxidation and etching reactions which are proposed to be: [31]

Oxidation: $\equiv Si\text{-}H\ (s) + H_2O\ (l) \xrightarrow{OH^-} \equiv Si\text{-}OH\ (s) + H_2\ (g)$ (3)

Etching: $(\equiv Si)_3Si\text{-}OH\ (s) + 3HF\ (aq) \longrightarrow 3(\equiv Si\text{-}H)\ (s) + SiF_3OH\ (aq)$ (4)

Oxidation of a Si-H bond produces Si-OH and releases one H_2 molecule. Because the Si-H bond is almost nonpolar, this is a slow and rate-limiting step.[47] Then, the Si-OH bond is substituted by a Si-F bond. Due to the high electronegativity difference between F and Si, the Si-Si bond underneath is polarized. This facilitates chemical disruption of the Si-Si bond. An H atom attaches to the $Si^{-\delta}$ (bound to the surface), and an OH bonds to

the $Si^{+\delta}$ (bound to the F).[47] Finally, the Si, attached to the F, enters the solution as SiF_3OH.[31] Because the first step is the rate-limiting step, the etched surface is completely hydrogen-terminated.[20,47,48]

Fig. 2.11 shows a few etch pits. Etch pits are particular features of the etched surface and they are formed when the rate of terrace etching is not equal to zero. Even though the hydrogen-terminated Si(111) surface is highly resistant to oxidation in air, the surface is extremely sensitive to the oxygen content of the etchant solution. It is known that dissolved O_2 can nucleate etch pits.[49] The reduction of O_2 produces the superoxide anion radical, which is an intermediate.

$$O_2 + e^- \rightarrow O_2^{-}\bullet \quad (5)$$

The etch pit formation, due to trace amount of $O_2^{-}\bullet$, is suggested to be as: [49]

$$O_2^{-}\bullet + \equiv Si\text{-}H \rightarrow \equiv Si\bullet + HO_2^- \quad (6)$$

In order to reduce the number of etch pits, an argon-purged solution of NH_4F was used. However, a few etch pits observed in Fig.2.11 can be attributed to the existence of oxide, along with dislocation in the silicon wafer, which can also produce etch pits [21]. As expected, applying a highly anisotropic etchant generated triangular etch pits (Fig. 2.11). A highly anisotropic etchant removes atoms from pits' edges in rows. This, along with threefold symmetry of the surface results in triangular etch pits. Because low anisotropic etchants, such as NH_4F(aq) containing 0.2% isopropanol, undergoes a less site-selective etching reaction, they generate blunted triangle etch pits.[21]

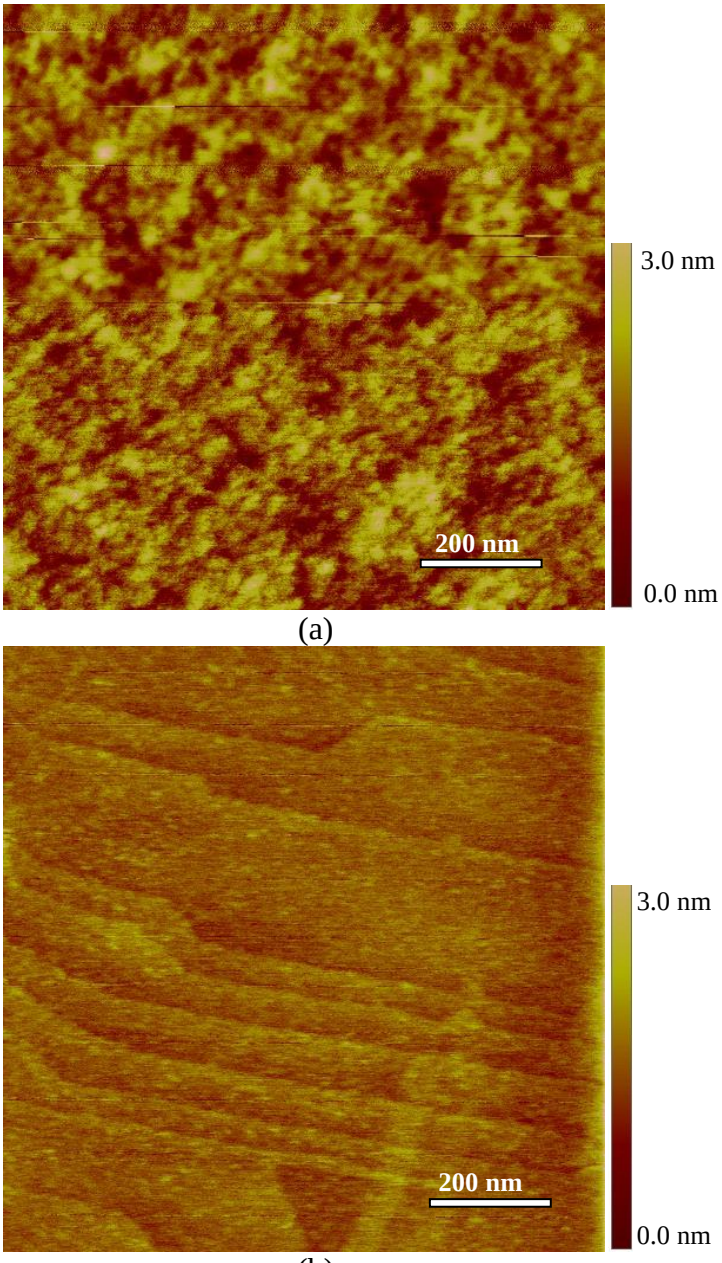

Fig. 2.10. (a) Contact- and (b) tapping-mode AFM images of BSA adsorption at a carboxylic acid-terminated surface. To prepare the surface, Si(111) was etched, thermally functionalized with methyl 10-undecenoate, and hydrolyzed with HCl. Subsequently, 5.6 mg/mL BSA solution was deposited at the surface. After 1.5 h, the solution was pipetted out, and the surface was dried in nitrogen gas flow.

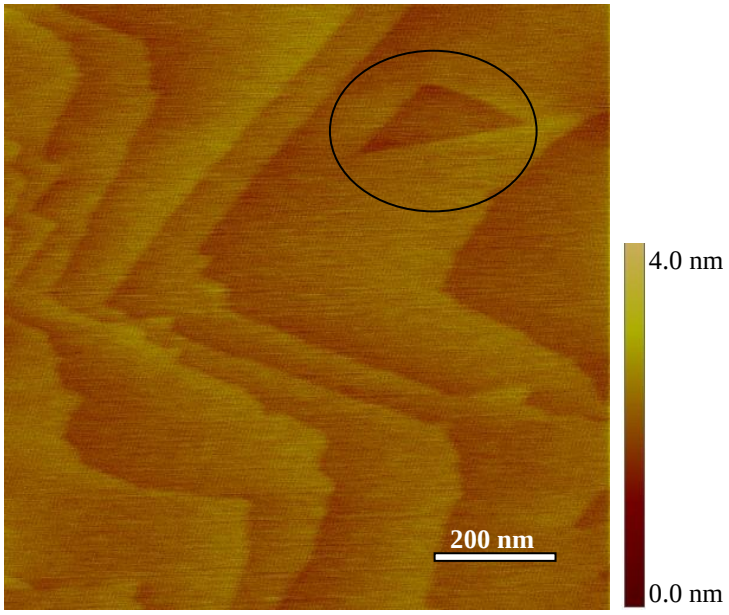

(a)

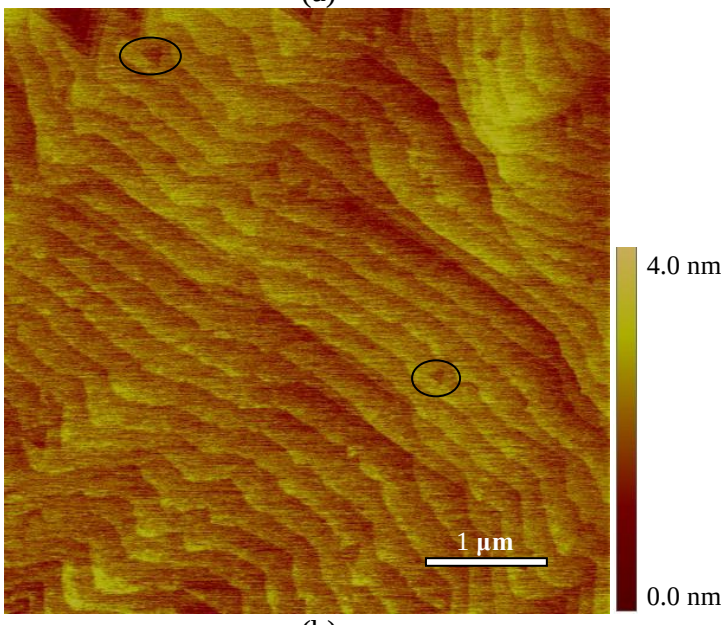

(b)

Fig. 2.11. (a) 1 µm × 1 µm and (b) 5 µm × 5 µm contact-mode AFM images of a H-Si(111) surface. In order to prepare the substrate, n-type Si(111) was etched in 40% NH_4F (aq) for 30 minutes under argon flow. Examples of etch pits are circled.

Fig. 2.12 and 2.13 show tapping-mode AFM images of n-type Si(111) surfaces, etched and thermally functionalized with 1-decene and methyl 10-undecenoate, respectively.

The average step height for the above-mentioned surfaces is 0.32 ± 0.04 nm and 0.32 ± 0.01 nm, respectively. The AFM images are in agreement with that of the freshly etched H-Si(111) surface (Fig. 2.11) in which steps with a height of 0.31 ± 0.04 nm separate the atomically smooth terraces. Fig. 2.12 and 2.13 confirm that the surface modification did not alter the surfaces significantly. These surfaces are chosen as methyl- and ester-terminated templates to study protein adsorption. According to the literature, an advancing contact angle of a silicon surface, terminated with methyl, is ~110° revealing hydrophobicity of the surface. However, a methyl ester-terminated silicon surface with an advancing contact angle[1] of ~77° shows less hydrophobicity.[17]

In fact, forming an oxide-free surface through a hydrosilylation reaction was found to be very challenging. Various drying agents like molecular sieve were tried to obtain surfaces free of oxide. Moreover, different solvents such as anhydrous ethanol, carbon tetrachloride, tetrahydrofuran, deionized water, hot acetic acid and trifluoroacetic acid were used to remove physisorbed materials and SiO_2.

Some literature used contact-mode images as a proof of obtaining oxide- and physisorbed-free surfaces.[46] However, through contact-mode AFM imaging, the tip is able to remove SiO_2 formed on the surface. As an example, Fig. 2.14a and 2.14b show tapping- and contact-mode AFM images of a surface functionalized with methyl 10-undecenoate. While the former image shows several white features, the latter appears to be free of white spots. Observation of a band at ~1057 cm^{-1} in the IR spectrum indicates

[1] An advancing contact angle is measured when the maximum amount of liquid is added to the drop without a change in the liquid-solid interfacial area.

the presence of some oxide on the surface, which is a common problem in hydrosilylation reactions [46].

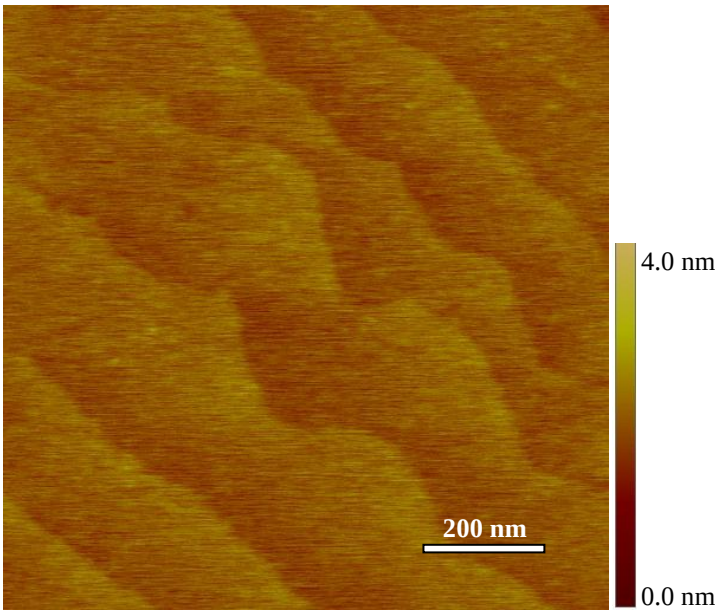

(a)

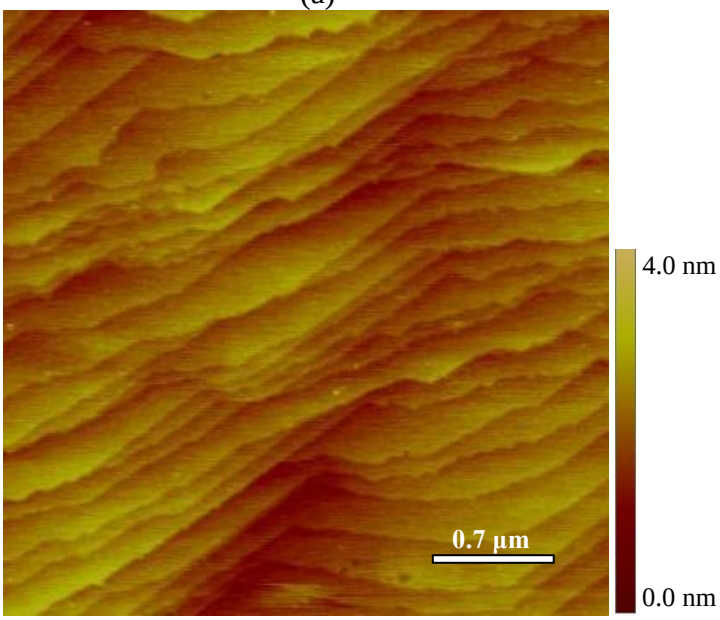

(b)

Fig. 2.12. (a) 1 µm × 1 µm and (b) 3.5 µm × 3.5 µm tapping-mode AFM images of a 1-decene-modified Si(111) surface.

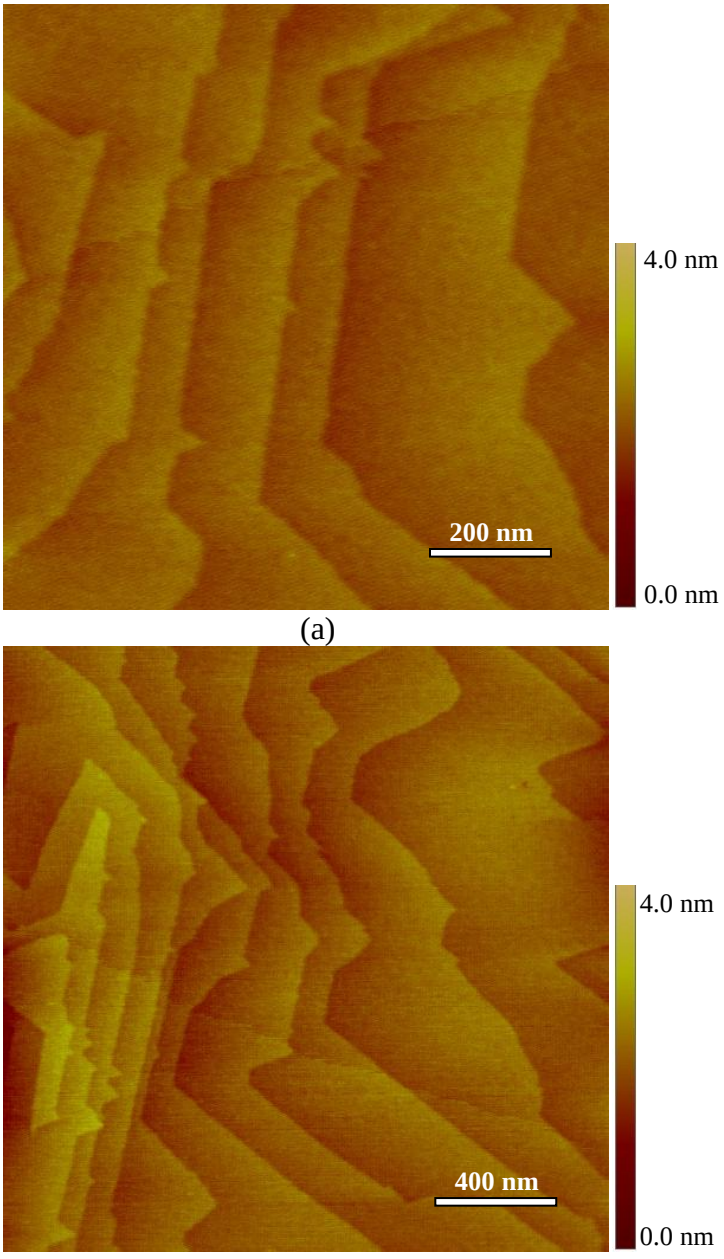

Fig. 2.13. (a) 1 μm × 1 μm and (b) 2 μm × 2 μm tapping-mode AFM images of a methyl 10-undecenoate-modified Si(111) substrate.

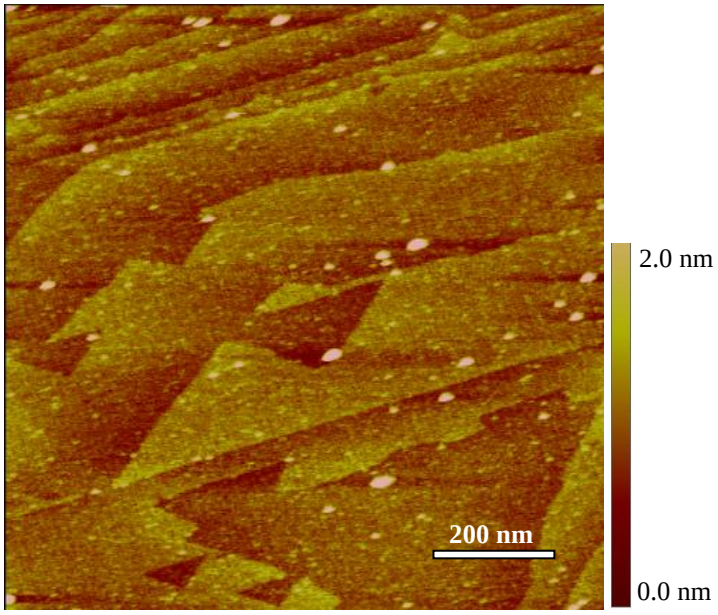

(a)

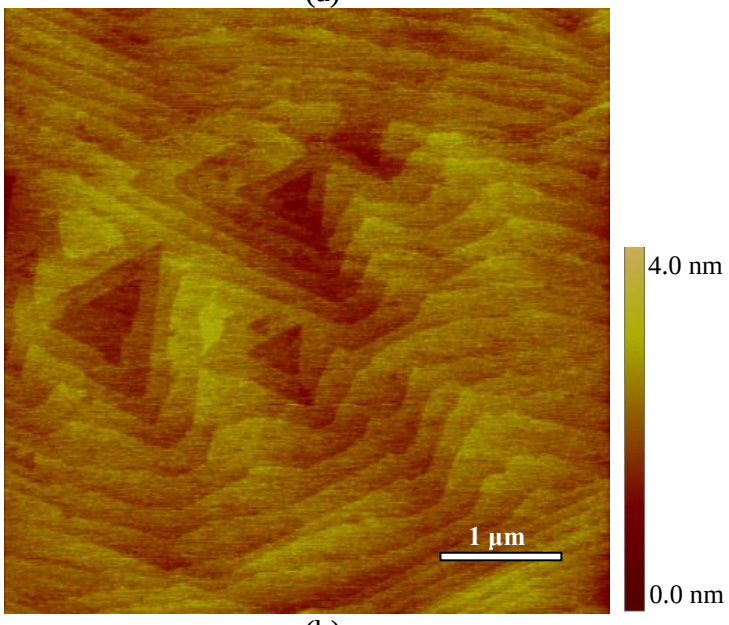

(b)

Fig. 2.14. (a) Tapping and (b) contact-mode AFM images of a methyl 10-undecenoate-modified Si(111) surface. While the first image shows considerable amount of white spots, the second one seems free of them. Because of a band, observed at ~1057 cm^{-1} in the IR spectrum, the white spots of b are attributed to SiO_2.

AFM does not give chemical information on the features observed at the surfaces. Therefore, prior to exposing to the protein solution, the surfaces should be confirmed to be free of the features that could be assigned to protein adsorption. We carried out the hydrosilylation reaction several times to obtain surfaces free or with a low degree of SiO_2 formation.

ATR-FTIR was employed to confirm the chemical modification of the silicon surfaces. While thermal modification with 1-decene and methyl 10-undecenoate has been shown to be straightforward [13], surface modification involving hydrolysis requires the reaction to be monitored. An ATR-FTIR spectrum of the acid-terminated silicon substrate is shown in Fig. 2.15. In order to prepare this surface, the ATR element was modified with methyl 10-undecenoate and then hydrolyzed. A freshly etched Si(111) ATR substrate was used to subtract the background.

The negative peak at ~2082 cm^{-1} corresponds to Si–H stretch mode. Peaks at ~2853 cm^{-1} and ~2925 cm^{-1} are assigned to C–H stretch of CH_2. The peak at ~1712 cm^{-1} corresponds to the carbonyl stretch of the carboxyl group. This peak replaced the peak at ~1745 cm^{-1} related to surfaces terminated with a methyl ester group. These observations are in good agreement with the literature.[16,17] The above-mentioned data confirmed the formation of a carboxylic acid-terminated surface, as well as the successful preparation of the original ester-terminated surface.

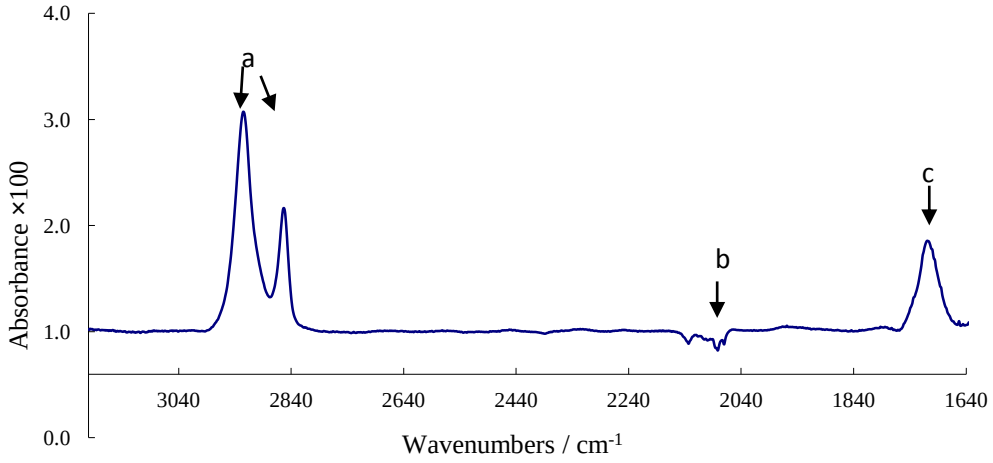

Fig. 2.15. ATR-FTIR spectrum of a carboxylic acid-terminated Si(111) substrate. The absorbance (the logarithmic ratio of the initial radiation to the transmitted radiation) is graphed versus the wavenumber. The surface was functionalized with methyl 10-undecanoate; then, the substrate was hydrolyzed. In order to subtract the background, a freshly etched Si(111) ATR substrate was used. Peaks at (a) 2925 cm^{-1} and 2853 cm^{-1}, (b) 2082 cm^{-1} and (c) 1712 cm^{-1} are corresponding to CH_2, Si-H, as well as C=O of the carboxylic acid, respectively.

2.3.2. Protein Adsorption

In this section we will present our attempt to investigate BSA and insulin adsorption at 1-decene- and methyl 10-undecenoate-modified Si(111) surfaces using AFM. The data will be discussed in the context of the previous MALDI-MS experiments performed by Professor S. Morin's group [13]. Additionally, volume analysis of BSA, adsorbed at 1-decene- and methyl 10-undecenoate-modified surfaces, will be presented.

Firstly, the data for BSA adsorption at two modified surfaces will be presented. BSA was adsorbed at a methyl 10-undecenoate-modified Si(111) surface using 1 mg/mL BSA solution. This BSA adsorption resulted in distinct particles shown by the tapping-mode AFM image of Fig. 2.16a. To assess whether the number of BSA molecules in each

particle is concentration-dependent, the BSA solution was diluted to 0.2 mg/mL and allowed to adsorb on the methyl 10-undecenoate-modified surface. As shown in Fig. 2.16b, much less adsorption was observed.

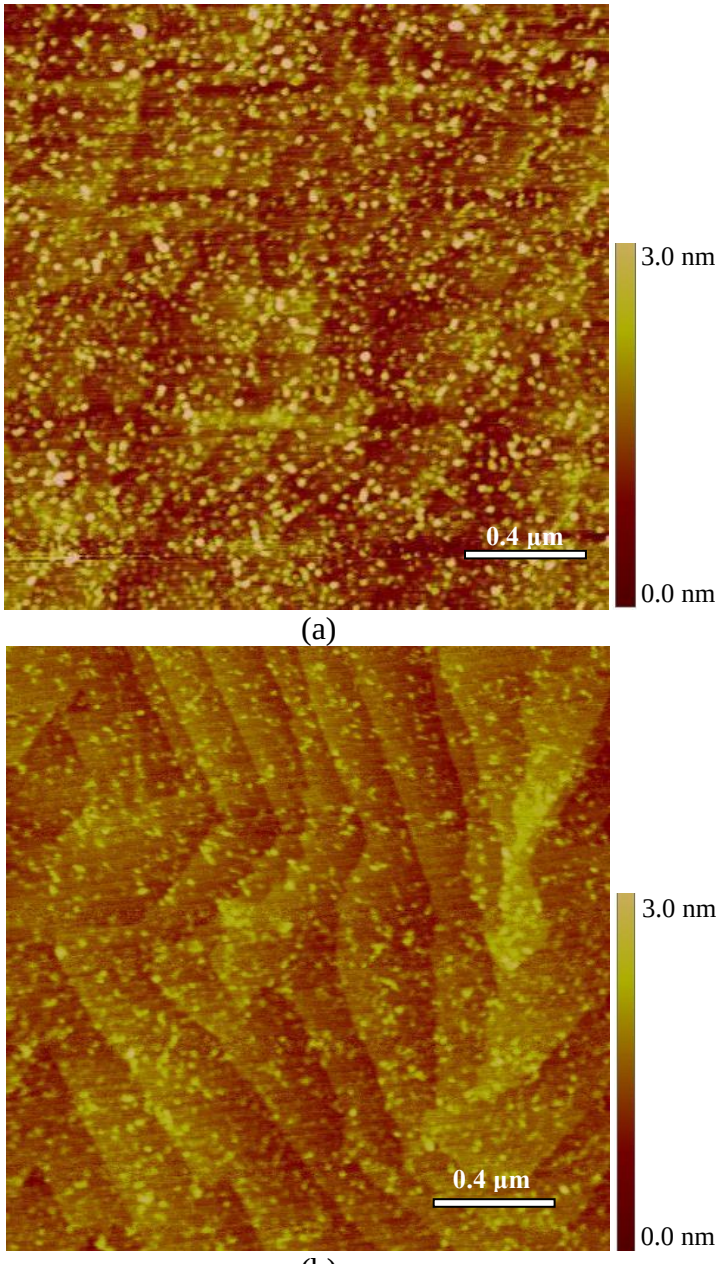

Fig. 2.16. 2 µm × 2 µm Tapping-mode AFM images of (a) 1 mg/mL and (b) 0.2 mg/mL BSA deposition at a methyl 10-undecenoate-modified Si(111) surface.

In order to investigate BSA adsorption at a 1-decene-modified Si(111) surface, a more dilute solution with concentration of 0.01 mg/mL BSA was employed. This BSA adsorption is shown in the tapping-mode AFM images (1 μm x 1 μm and 5 μm x 5 μm) of Fig. 2.17.

Insulin adsorption was investigated at the 1-decene- and methyl 10-undecenoate-modified Si(111) surfaces. Initially, 10% saturated insulin solution was used. Fig. 2.18 shows AFM images of a 1-decene-modified Si(111) surface after deposition of the 10% saturated insulin solution. Insulin was not detected.

The 10% saturated insulin was also employed to adsorb at the ester-terminated surface. The AFM image of this surface (Fig. 2.19a) shows the same result as depicted in Fig. 2.18 (10% saturated insulin deposition at the 1-decene-modified surface). No insulin was detected. Subsequently, a higher concentration of insulin was employed. Fig. 2.19b shows adsorption of a saturated insulin solution at a methyl 10-undecenoate-modified Si(111) surface. This AFM image reveals a considerable amount of insulin all over the surface.

AFM images of the BSA-deposited ester-terminated surface were analyzed to investigate the number of BSA molecules present in the adsorbed particles. The effect of this adsorption on the compact form of BSA was also investigated. To calculate the number of BSA molecules, a value of 88.25 nm^3 [35] was used for the volume of BSA. In order to carry out volume analysis of the particles, ImageSXM software and the method mentioned by Ratcliff and Erie were employed [44]. In this method, the surface area of the particles is multiplied by their thickness to get the volume.

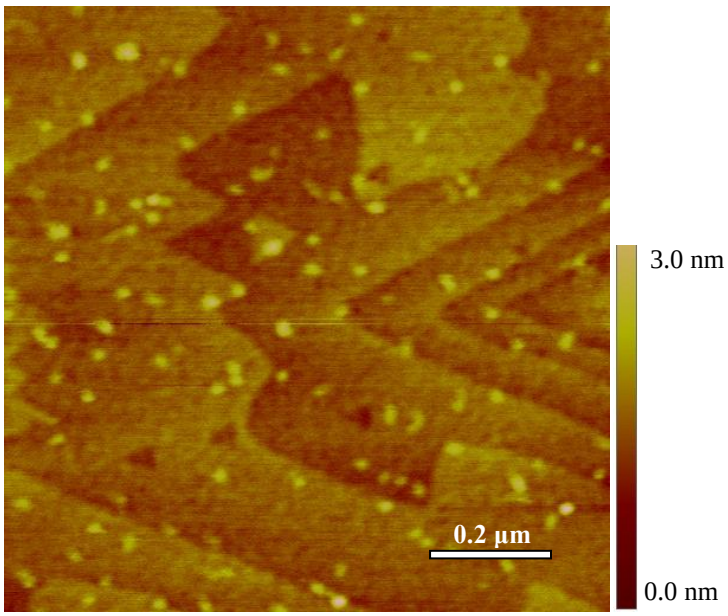

(a)

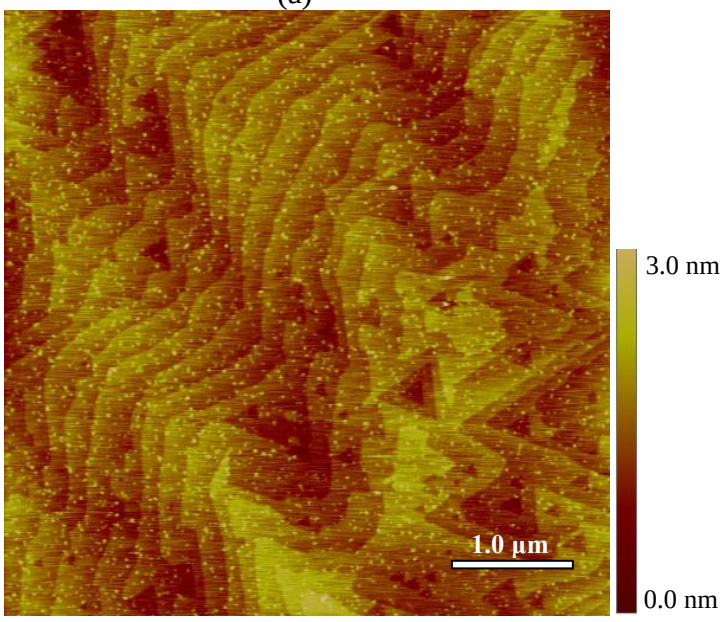

(b)

Fig. 2. 17. (a) 1 µm x 1 µm and (b) 5 µm x 5 µm tapping-mode AFM images of a 1-decene-modified Si(111) substrate after 0.01 mg/mL BSA solution deposition.

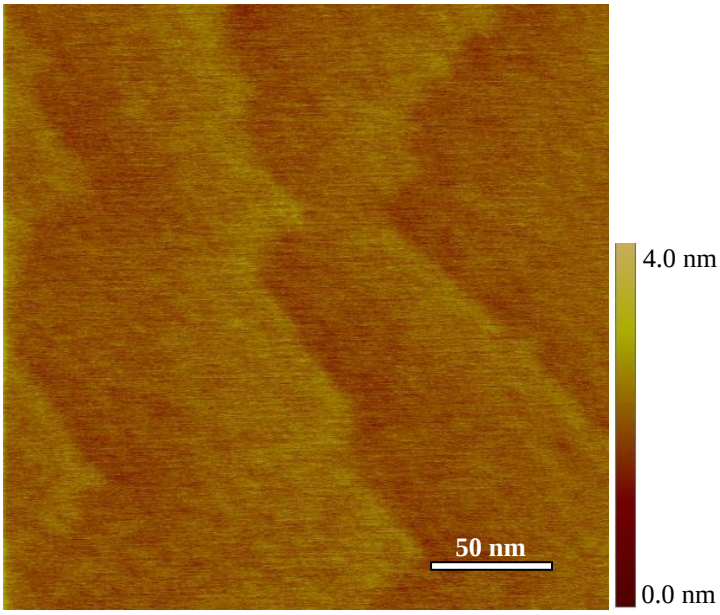

(a)

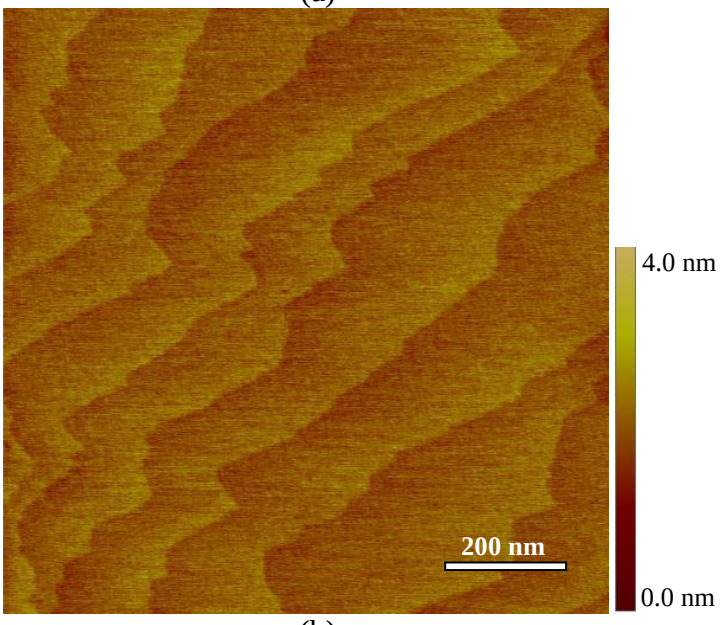

(b)

Fig. 2.18. (a) 250 nm × 250 nm and (b) 1 μm × 1 μm AFM images of a 1-decene-modified Si(111) substrate after the deposition of 10% saturated insulin solution.

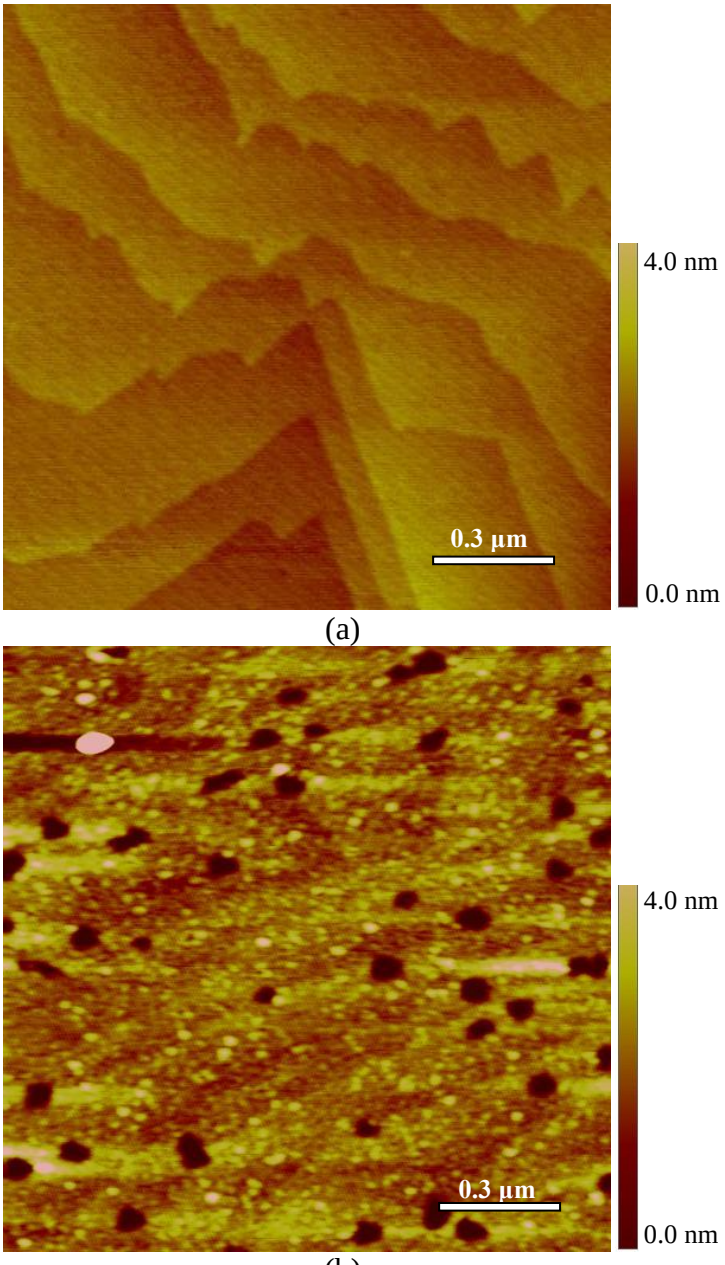

Fig. 2.19. 1.5 µm × 1.5 µm Tapping-mode AFM images of a methyl 10-undecanoate-modified Si(111) substrate after (a) 10% saturated and (b) saturated insulin solution deposition.

Fig. 2.20a and 2.20b show two histograms related to BSA adsorption at methyl 10-undecenoate-modified substrates via 0.2 and 1 mg/mL BSA solutions, respectively. The histograms show the percentage of the particles versus the number of BSA molecules in

each particle. Even though the higher BSA concentration (1 mg/mL) resulted in much more adsorption (Fig. 16b), it is revealed that in both cases (0.2 and 1 mg/mL), BSA was mostly adsorbed as individual molecules.

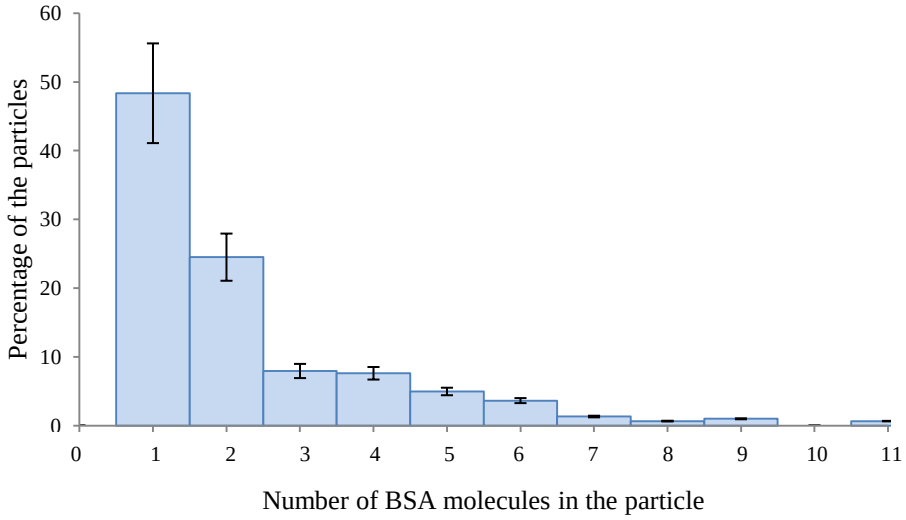

(a)

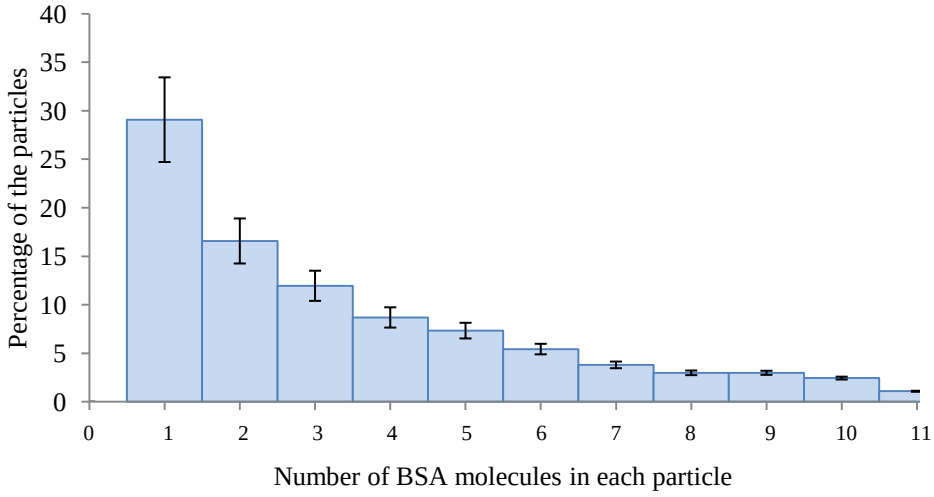

(b)

Fig. 2.20. BSA adsorption from (a) 0.2 mg/mL and (b) 1 mg/mL BSA solutions at a methyl 10-undecenoate-modified Si(111) surface. The histograms show the percentage of the BSA particles versus the number of BSA in each particle detected by AFM. The BSA volume analysis is carried out using ImageSXM software and the method mentioned by Ratcliff and Erie.[44] To measure the number of BSA in each particle, the volume of each particle is divided by the volume of a single BSA molecule.

In a separate analysis, the average thickness of the particles was determined from AFM images. The adsorption of the solutions, containing 0.2 and 1 mg/mL of BSA at methyl 10-undecenoate-modified substrates, was recorded. Thicknesses of 0.4 ± 0.1 nm and 0.6 ± 0.2 nm were observed for the above-mentioned solutions. The lower thickness of the BSA spots, due to adsorption from the lower concentration solution (0.2 mg/mL), is consistent with the findings of particle-size analysis where more individual BSA was observed. The thickness of the BSA layer due to adsorption from 0.01 mg/mL solution at 1-decene-modified surface was also measured, which turned out to be 0.4 ± 0.1 nm. Because the observed average values for the thickness of the BSA particles were smaller than the smallest dimension of BSA (3 nm [36-38]), it is inferred that the BSA molecules unfold and spread upon adsorption onto the methyl- and ester-terminated surfaces to increase the strength of the protein-surface interactions. T. C. Ta and his colleague obtained a value of 1.7 ± 0.3 nm for the thickness of the BSA particles adsorbed at the hydrophobic surface of highly oriented pyrolytic graphite (HOPG) when 0.01 mg/mL BSA solution was allowed to interact for 30 min with the surface.[50] They carried out AFM imaging using a fluid cell. Even though this value is much bigger than our values, it still shows the BSA unfolding due to adsorption.

It should be mentioned that, in our experiments, the BSA adsorption took place during a much shorter time (~30 sec) to avoid extensive adsorption. These conditions allowed single proteins or particles with small number of BSA molecules to be characterized by AFM. A longer time of exposure of the surface to the BSA solution results in more adsorption and a thicker layer of the BSA. For lower coverage, a higher conformational

change is suggested. Note that neighboring molecules can confine the spreading of the protein upon adsorption. Moreover, we dried the substrates before imaging, which could cause more unfolding and flattening.

Roach *et al.* studied changes in the secondary structure of BSA as a result of binding to a methyl-terminated surface.[42] The authors showed that BSA loses a large degree of its α-helix structure by the interaction with a methyl-terminated surface. The structural changes cause the BSA to spread for a larger interface with the surface. No changes of this nature were observed upon adsorption to the OH-terminated surface.[42]

Here, a comparison between the results of the protein adsorption study via MALDI-MS experiments [13] and our AFM images is presented. (Table 2.1) In the former research, T. Z. Mengistu *et al.* employed the MALDI-MS technique to investigate the non-specific binding of proteins from a mixture of eight proteins on different alkyl-modified Si(111) substrates.[13] They applied a mixture of proteins including 1.0 mg/mL BSA and 10% saturated (~0.01 mg/mL) insulin.

The MALDI-MS spectra for methyl- and ester-terminated surfaces are shown in Fig. 2.3. After protein deposition, pH 7 buffer (Fig. 2.3a) and deionized water (Fig. 2.3b) were used to rinse the surfaces. Fig. 2.3a shows the mass spectra related to the protein adsorption at the methyl 10-undecenoate- and 1-decene-modified surfaces, while Fig. 2.3b shows the proteins adsorbed at the 1-decenol-modified surface. Although the greatest degree of adsorption was observed for insulin, BSA was detected in none of the spectra.

Table 2.1. Comparison between BSA and insulin adsorption at methyl 10-undecenoate- and 1-decene-modified Si(111) substrates, detected by AFM and MALDI-MS [13].

Methyl 10-undecanoate

BSA Concentration (mg/mL)	AFM	MALDI-MS
0.2	Detected	
1	Detected	Not detected

Insulin Concentration (mg/mL)	AFM	MALDI-MS
10% Saturated	Not detected	Detected
Saturated	Detected	

1-Decene

BSA Concentration (mg/mL)	AFM	MALDI-MS
0.01	Detected	
1		Not detected

Insulin Concentration (mg/mL)	AFM	MALDI-MS
10% Saturated	Not detected	Detected

Based on these results, the authors concluded that the lack of strong BSA MALDI-MS signal could be attributed to either competition between the components in the protonation process or because of less degree of BSA adsorption. Our AFM images have shown that in addition to 1 mg/mL BSA (Fig. 2.16a), the 0.2 mg/mL BSA solution (Fig. 2.16b) resulted in considerable protein adsorption at a methyl 10-undecenoate-modified substrate. As shown in Fig. 2.17, even BSA adsorption was observed when we used 0.01 mg/mL solution at a 1-decene-modified Si(111) surface.

On the contrary, AFM investigation did not detect insulin after the deposition of 10% saturated solution at the surfaces modified with 1-decene (Fig. 2.18) and methyl 10-undecenoate (Fig. 2.19a). Even though insulin is ten times lighter than BSA, because of its spherical shape, the diameter of insulin (2.3 nm) is comparable with the smallest dimension of BSA (3 nm). Moreover, because most insulin residues are solvent accessible [31], less unfolding due to adsorption is expected. We concluded that if the

10% saturated insulin solution had resulted in protein adsorption, comparable to the BSA adsorption, AFM would have detected it. Table 2.1 depicts results of the BSA and insulin adsorption at the methyl- and ester-terminated surfaces detected by AFM and MALDI-MS. The AFM investigation on BSA and insulin adsorption onto the methyl- and ester-terminated surfaces showed that applying 1 mg/mL BSA solution resulted in more adsorption than using 10% saturated insulin solution. This finding is not in conformity with the MALDI-MS investigations accomplished by T. Z. Mengistu *et al*.[13] MALDI is a two-step process. In the first step, UV laser beam[1] produces a hot stream of neutral and ionized matrix molecules. In the second step, this stream ionizes (protonates or deprotonates) and detaches the analyte molecules from the surface. Hence, any weak MALDI-MS signal can be attributed to either a low quantity of the adsorbate or a stronger bond between the adsorbate and the surface. At the methyl- and ester-terminated surfaces, more protein was detected (by AFM) from 1 mg/mL BSA than from saturated insulin solution. Therefore, the lack of BSA MALDI-MS signal is attributed to stronger BSA-surface interaction rather than the lack of BSA adsorption.

As the solubility of insulin in water is less than 16 μM or 0.1 mg/mL [28], the concentration of the 10% saturated insulin solution is much less than that of the applied BSA solution (1 mg/mL). Even the molarity of the insulin solution is around 9.5 times less than the BSA solution. Therefore, it is not surprising to observe more BSA via the above-mentioned solutions. However, even 0.01 mg/mL BSA solution resulted in more adsorption than 10% saturated insulin. These two solutions have almost the same

[1] In the above-mentioned experiment, a nitrogen laser (337 nm wavelength) was used.[13]

concentration. Therefore, concentration is not the only factor affecting the difference between the adsorption level of BSA and insulin. This can be explained by the difference in size, because high the affinity of proteins to adsorb at different surfaces is due to their amphiphilic nature and is proportional to their dimensions. The spectra in Fig. 2.3a and 2.3b show a large signal at ~5.8 kDa while no signal at ~11.6 kDa was detected. This observation suggests that in a 10% saturated solution, insulin molecules exist as monomers.[13] Even though at neutral pHs, electrostatic repulsion is not a barrier for the self-association behavior of insulin, dimerization is highly limited by the low solubility of insulin in pure water (less than 0.1 mg/mL). In an aqueous solution, insulin dimerization mostly occurs in concentrations higher than 10 mg/mL.[25] At such a low concentration of 0.1 mg/mL (saturated insulin solution), and in the absence of zinc ions, a large proportion of monomeric insulin molecules exist in solution.[27] Even though both the insulin and BSA adsorbed at the studied surfaces, mostly as monomers, BSA with a molecular weight of about 66 kDa is more prone to adsorption than insulin monomers with the molecular weight of 5.8 kDa. In our study, the charge densities of the BSA and insulin are likely not the cause of the adsorption behavior observed. At neutral pHs, the net charges of BSA and insulin are around -18 [40] and -2 [25], respectively. However, considering their molecular weights, insulin and BSA have almost the same charge densities.

2.4. Conclusions

In this section, we presented our work on the BSA and insulin adsorption at 1-decene- and methyl 10-undecenoate-modified Si(111) substrates. Our results were compared to the MALDI-MS spectra of the work previously carried out by Professor S. Morin's group [13]. When applying a solution with 1 mg/mL BSA and ~0.01 mg/mL insulin, at methyl- and ester-terminated surfaces, MALDI-MS did not detect BSA, but a large insulin signal was observed. The BSA and insulin solutions that we employed had the same concentration level as the experiment with MALDI-MS. Our AFM images show considerable amount of BSA adsorbed while no insulin could be detected at the methyl- and ester-terminated surfaces. The images show that BSA has much higher affinity than insulin to adsorb at the 1-decene- and methyl 10-undecenoate-modified Si(111) substrates, while the mass spectra indicated opposite results. We inferred that lack of BSA MALDI-MS signal is due to the stronger interaction between the surface and BSA, rather than the absence of the adsorbed BSA at the substrates. The magnitude of this interaction is proportional to the BSA size.

After deposition of 0.2 and 0.01 mg/mL BSA solutions at the methyl 10-undecenoate-modified Si(111) substrate, BSA volume analysis has shown that BSA adsorbed mostly as individual molecules.

Chapter 3: Oligomerization of ΔK122-4 Pilins at Alkanethiol SAMs on Gold

3.1. Introduction

There are different possible protein nanotube designs to capture specific molecules with potential applications in biosensing. For instance, recently, G. F. Audette *et al.* have proposed that attachment of a specific sequence of amino acids at the outer surface of PNTs can introduce a binding site for particular ligands.[1] Moreover, via ssDNA attachment, PNTs are able to capture ssDNA with complementary sequence. [1] ssDNA can form a covalent bond with biotin (biotinylation).[1] Particular molecules can be targeted by the PNT via biotinylated ssDNA or complementary ssDNA. For electrochemical detection applications, DNA-attached PNTs can be an alternative for DNA-attached CNTs, because unlike CNTs, employing PNTs in a biological environment is not a challenge. (See section 1.2.2) Various designs can introduce electrical conductivity to PNTs. It is known that the coordination of divalent metal ions to DNA gives electrical conductivity to the structure.[2-7] This finding suggests a possible nanowire property of PNTs coated with metal-bound DNA. T4P of several bacteria demonstrate a nanowire system. For example, the bacterium *Geobacter sulfurreducens* is able to transfer electrons to insoluble Fe(III) oxides through its pili.[8] Some bacteria such as *Shewanella oneidensis* have electrically conductive pili.[9]

However, PNTs have a much lower tensile strength[1] than carbon nanotubes.[10] While even the weakest types of carbon nanotubes have tensile strength of several GPa [11], it is reported that type IV pilus, an example for natural protein nanofibers, withstands stress of only 100 pN [10]. Nonetheless, there are chemical or protein engineering ways to increase the strength of PNTs. For example, glutaraldehyde forms a bridge between lysine residues via covalent bond formation.[10] An alternative choice is cross-linking between cysteine residues which can be introduced via protein engineering.[10] If cysteine residues are in the right position, an oxidizing condition can form disulfide bonds spontaneously.[12]

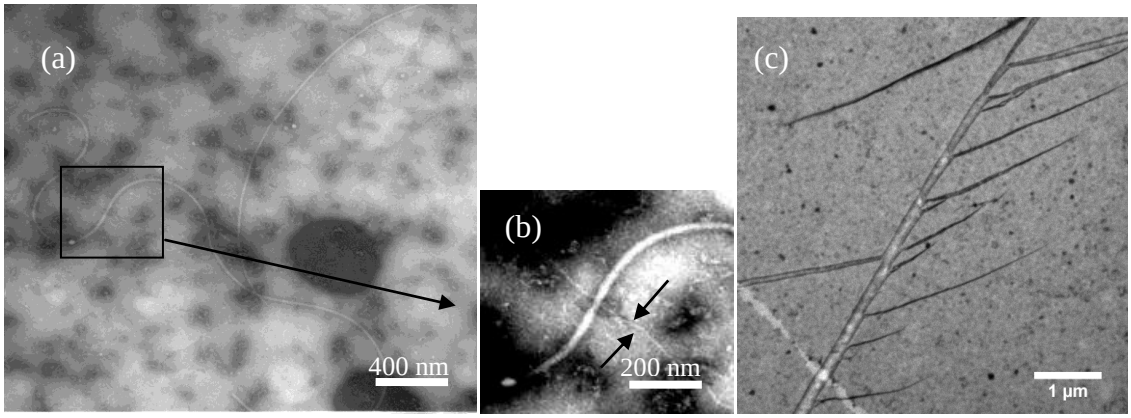

Fig. 3.1. (a) Negatively stained transmission electron microscope image of singles and bundles of ΔK122-4 pilin-based PNTs. (b) A magnified view of the boxed area, shown in a. Arrows show a single PNT. (c) Negatively stained TEM image of a branched ΔK122-4 pilin-based PNT. The oligomerization is initiated by 1-undecanethiol (0.58 M) in ΔK122-4 pilin solution (13 mg/mL). PNTs are formed during 6 days at room temperature. Reprinted with permission from (Lombardo, S. The Development of Solution and Surface Associated Protein Nanotubes for Applications in Bionanotechnology. M.Sc. Thesis, York University, Toronto, ON, 2010."

[1] Tensile strength measures the force per unit area required to pull something to the point where it breaks.

It is known that in a solution of engineered pilins from bacterium *P. aeruginosa,* the presence of hydrophobic molecules can trigger nanotube self-assembly (Fig. 3.1).[10,13] However, solution-grown nanotubes are hard to handle due to their size and their ability to adsorb on various types of surfaces [10]. These facts gave us the idea to use self-assembled monolayers (SAMs) as a mean to nucleate protein nanotubes at the surface to facilitate their handling and chemical modification without sample losses.

3.1.1. Alkanethiol Self-Assembled Monolayer on Au(111)

Alkanethiols form an organized superstructure of self-assembled monolayers with a favorable length and terminal group on gold. Gold has some advantages that make it suitable for this research.[14] Gold is the most studied substrate and thiols bind to gold with high affinity. They substitute physisorbed materials on the surface. Compared to metals such as palladium and platinum, which also have affinity for thiols, gold has a lower melting point (1040ºC) and tends to produce films with bigger grains. It is important that gold does not have a toxic effect on biological environments. Moreover, a SAM formed from thiols on gold is stable from days to weeks under biological conditions.[14]

3.1.1.1. Mechanism of Alkanethiol SAM Formation on Gold

It is believed that the mechanism of self-assembled monolayer formation from solution is similar to the one involved in SAM formation from a gas phase. This mechanism probably involves physisorption of the lateral part of the alkanethiol molecules onto the

surface (Fig. 3.2a).[14] In this state, the S-H bond remains intact, but eventually this bond dissociates and the thiolate forms.[14] Hydrogen is possibly released as H_2:

$$R\text{-}SH + Au \rightarrow R\text{-}S\text{-}Au + 1/2\ H_2 \quad (1)$$

Dissociation of S-H bonds (~339 kJ/mol) is driven by the formation of the gold-sulfur bond (~-167 kJ/mol), the heat resulting from the physisorption of alkanethiol on the surface, noncovalent interaction of the alkanethiols, and thermal energy. [14-16] Due to the additive contributions of the van der Waals forces of the entire chain, physisorption of the longer alkanethiol chain creates more heat to overcome the activation barrier of S-H bond dissociation.[17] The physisorption energy of n-alkanes on Au(111) increases 5.9 kJ/mol per additional carbon.[16] As an example, the physisorption of 1-hexanethiol on Au(111) releases ~36 kJ/mol.[16] An increase of the chain length thermodynamically improves SAM formation. On the other hand, a strong interaction between a long-chain alkanethiol and gold surface limits the kinetics of the process.[14]

Thermal energy (~29 kJ/mol) is necessary to cross the energy barrier to go from the physisorbed to the chemisorbed state. [17] For example, formation of 1-hexanethiol SAM on gold is not feasible at temperatures below 200 K.[14] At this temperature, the translational kinetic energy of the molecules is ~2.6 kJ/mol. Below 200 K, alkanethiol molecules are physisorbed and form a flat-lying monolayer (Fig. 3.2a).[17] When the substrate is warmed up to 208 K, the system crosses the energy barrier and begins to form ordered domains of the dense SAM c(4 × 2) phase shown in Fig. 3.2c.[17]

Since lateral noncovalent interaction of the alkanethiols releases energy, as shown Fig. 3.2b, the thiols form a structure with the strongest lateral interactions (van der Waals,

hydrogen bonding).[14] Each chain-chain interaction releases ~4.2 kJ/mol per CH_2 group. [14] Therefore, longer alkyl chains form a better-ordered monolayer than shorter ones.

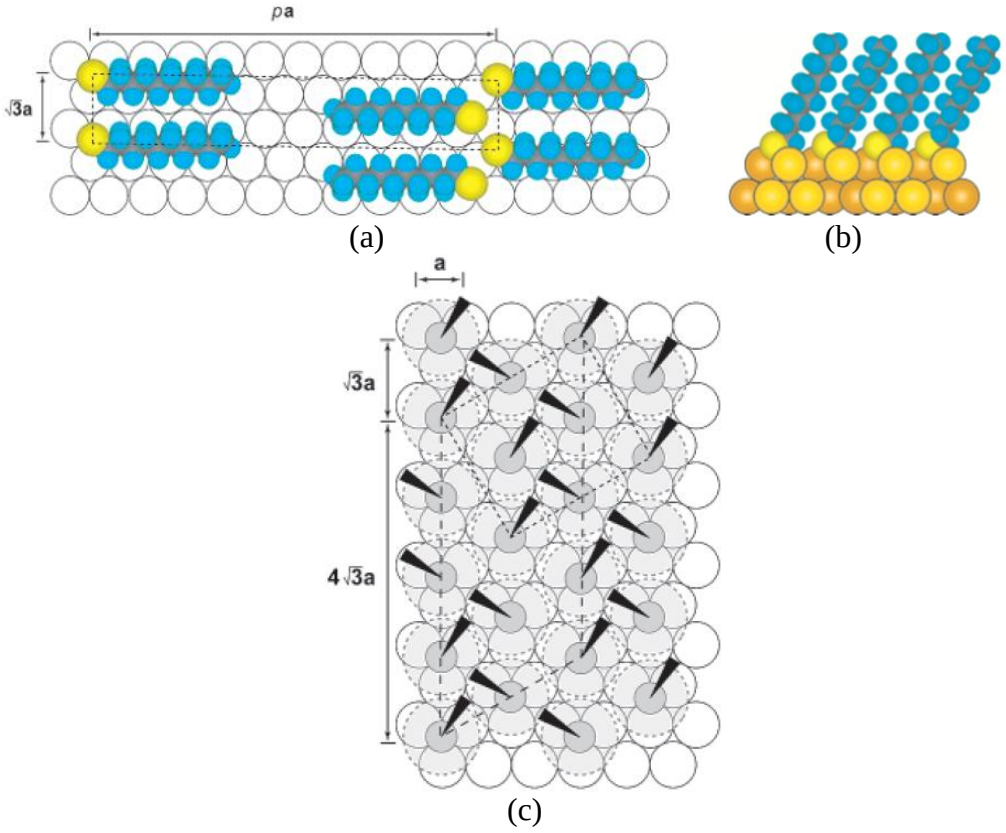

Fig. 3.2. Schematic diagrams depicting (a) a low coverage phase of thiols on Au(111) (a = 2.88Å). In this example, the periodicity of the rectangular of the unit cell (p) is 11.5. (b) Cross-section of the alkanethiol self-assembled monolayer on Au(111) formed from decanethiol, when maximum coverage of the thiolates is attained. (c) Structural model of the commensurate adlayer formed by decanethiols on the gold lattice with maximum coverage. The gold lattice, sulfur atoms and alkane chains are shown by white circles (a = 2.88 Å), dark gray circles and dark wedges. The shown arrangement is a (√3 × √3) R30° structure. The light gray circles with the dashed lines indicate the approximate projected surface area occupied by each alkane chain. The alternating orientation of the alkane chains defines a c (4 × 2) superlattice structure. The long dashes show the formal c (4 × 2) unit cell. An equivalent 2√3 × 3 unit cell is marked by lines with short dashes. "Reprinted with permission from (Love, J. C.; Estroff, L. A.; Kriebel, J. K.; Nuzzo R. G.; Whitesides, G. M. Self-Assembled Monolayers of Thiolates on Metals as a Form of Nanotechnology. *Chem. Rev*. **2005**, 105, 1103-1169). Copyright (2005) American Chemical Society."

The length of the thiol chain affects the SAM structure.[14] Alkanethiols ($CH_3(CH_2)_mSH$) with $m \geq 7$ form the ($\sqrt{3} \times \sqrt{3}$) R30° structure on Au(111) with a c (4×2) superlattice. (Fig. 3.2c) Alkanethiols with $m \leq 3$ form different structures of $p \times \sqrt{3}$ ($p = 8\text{-}10$). (Fig. 3.2a) It takes the short-chain thiols several hours to transfer from a 2D-liquid phase to a SAM, while long-chain alkanethiols ($m \geq 7$) form the SAM immediately. Alkanethiols with $3 < m < 7$ show intermediate behavior. For example for $m = 5$, both liquid phase and c (4×2) are observed.[14]

3.1.1.2. SAMs Defects

In addition to defects due to contamination, there are always intrinsic defects attributed to properties of the gold surface and the molecules that form SAMs.[14] The surface of polycrystalline gold shows a grain structure; consequently, the adsorbed layer follows the morphology of the surface with faulted part at the grain boundaries.

Gold surface reconstruction results in another type of defect.[14] While pure crystalline gold forms face-centered cubic (fcc) structures, Au(111) surfaces adopt a $(23 \times \sqrt{3})$[1] reconstruction.[18] This occurs because the binding symmetry is broken for the surface atoms.[19] Reconstruction is due to variations in registry between the top surface and the atomic layers below. This causes stacking arrangement alternations between the unfaulted ABC stacking and faulted ABA stacking (hexagonal close packing, hcp).[19] The surface of Au (111) adopts a herringbone structure which is formed by ordered domains of the faulted hcp among the unfaulted fcc domains, separated by rows of ridges

[1] It refers to the surface unit cell dimentions which are 23 and $\sqrt{3}$ times bigger than the diameter of one gold atom.

(Fig. 3.3a).[18] Reconstruction results in one extra Au atom per each ($23 \times \sqrt{3}$) primitive surface unit cell or 4.4% lateral compression relative to the bulk layers.[19] Due to alkanethiol adsorption, the herringbone features disappear and two atoms per ($23 \times \sqrt{3}$) primitive surface unit cell are released, introducing one net vacancy per the primitive surface unit cell.[19] The released Au adatoms diffuse rapidly and join the neighboring step edges.[19] As the thiol adsorption proceeds, the vacancy islands, which are mobile, coalesce into larger vacancy islands in the terraces.[19] The depth of a vacancy is equal to the diameter of one gold atom. In thiolate layers, pits with depth of 2.4 Å are consistent with creation of the vacancies.[18] Fig. 3.3b shows vacancy islands caused by thiophenol SAM formation on Au(111).

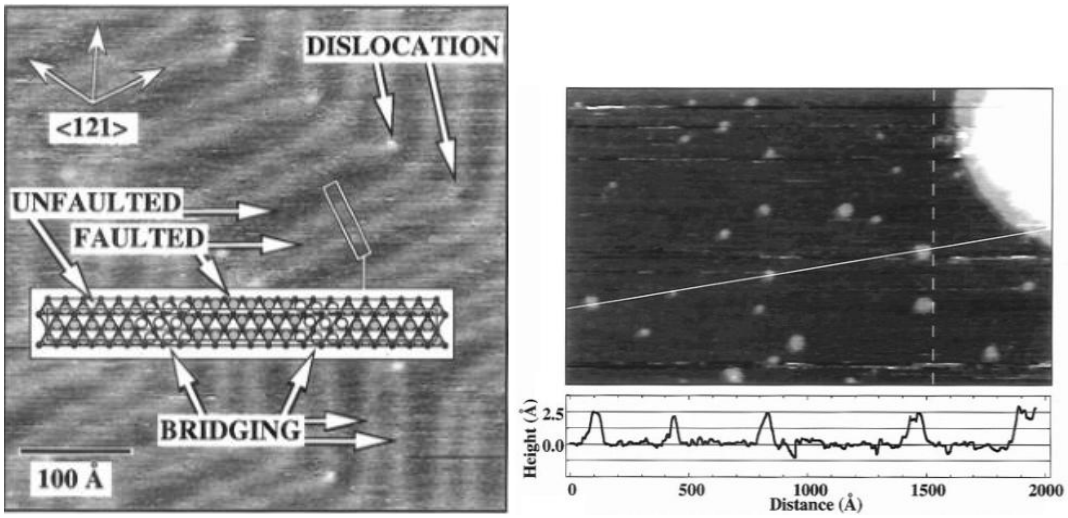

(a) (b)

Fig. 3.3. (a) Constant-current UHV STM image of bare Au(111) herringbone reconstruction with ($23 \times \sqrt{3}$) surface unit cell. Faulted (hcp), unfaulted (ccp) and bridging regions are shown in the figure. (b) STM image of thiophenol SAM on Au(111). Cross-sectional profile from the solid line of this image is shown bellow it and shows the ~2.5 Å height of the bright features which are attributed to Au islands. "Reprinted with permission from (Poirier, G. E. Mechanism of Formation of Au Vacancy Islands in Alkanethiol Monolayers on Au(111). *Langmuir*. **1997**, 13, 2019-2026). Copyright (1997) American Chemical Society."

Another kind of defect is due to the dynamic nature of SAMs. In the absence of a flux of the adsorbate, SAMs may be kinetically stable. However, the high coverage of adsorbate is thermodynamically unstable. Outside the solution used to prepare SAMs, only if the rate of desorption is zero, would the SAMs exist for an indefinite period of time.[14]

Fully extended alkanethiol (all trans conformation) adopts a crystalline structure on the surface of Au(111) with a tilt angle of 20º-30º.[14] SAMs show patches with an average size of 65-120 Å and a height of < 1 Å.[20] These regions are formed by chains with conformation different from that of the majority of alkanethiolate species. Fig. 3.4 depicts several kinds of defects found in SAMs formed on a polycrystalline substrate.

Missing thiolate molecules also form defect. Since at room temperature, the thermal energy is comparable to the rotational barrier of CH_2-CH_2, neighbours of the missing chain relax into the void space and decrease the depth of the hole.[21] Alkanethiol SAM on Au(111) is packed hexagonally; hence, each hole, due to a missing thiolate component, is surrounded by six nearest and the next six nearest molecules.[21] Relaxation of those molecules makes a depression.[21]

As an example, using STM, S. J. Stranick *et al.* studied two-component self-assembled monolayers of 1-hexadecanethiol and 16-mercaptohexadecanoic acid on gold.[20] They found that the smallest and the most common void defects, related to one missing thiolate, is about 1 Å deep and their full width at half-minimum is 18-25 Å. Defects with a diameter of $\geq$ 30 Å are attributed to multiple missing alkanethiolate chains and happen because of an insufficient deposition time.[20]

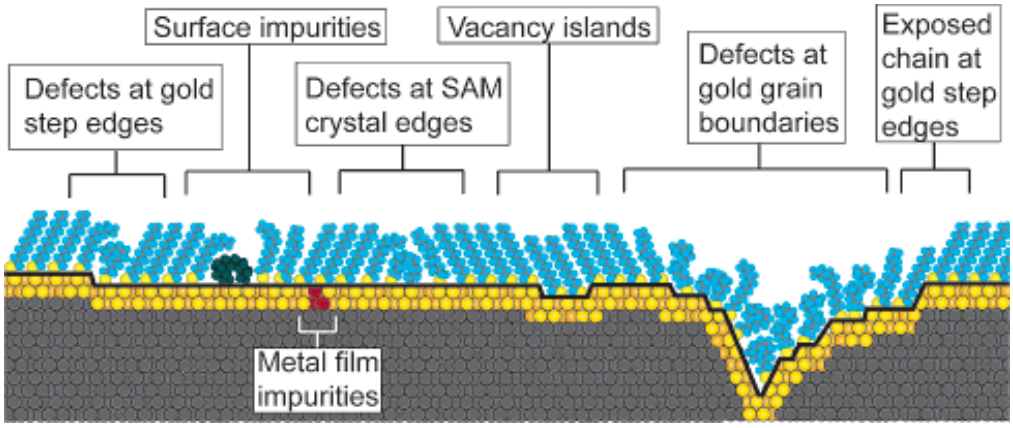

Fig. 3.4. Schematic diagram of intrinsic and extrinsic defects of SAMs formed on polycrystalline substrates. The dark line demonstrates the metal-sulfur interface. "Reprinted with permission from (Love, J. C.; Estroff, L. A.; Kriebel, J. K.; Nuzzo, R. G.; Whitesides, G. M. Self-Assembled Monolayers of Thiolates on Metals as a Form of Nanotechnology, *Chem. Rev.* **2005**, 105, 1103-1169). Copyright (2005) American Chemical Society."

In the case of monolayers composed of a mixture of alkanethiols, phase segregation provides another kind of defect. Phase-segregated domains can be as small as one molecule with a diameter of 5-7 Å. Domains of phase segregation move slowly within the densely packed layers.[20] When SAMs are prepared through co-adsorption from a solution containing two alkanethiols, mixed SAMs with some minor defects form quickly.[22] Then, the long chains placed in the solution have a much better chance to replace the short chains at the defective sites. The replacement trend of the short chains by the long ones is based on the interaction principle of long-long > short-short > short-long. Around the steps and defects, the exchange is more feasible. Thus, to have a more lateral interaction, exchange of the long with the short chains occurs. On the other hand, because of the steric effect in the terraces, the short chains have more chance to exchange with the long ones. Consequently, exchanges in terraces and steps result in the

segregation. Two-component SAMs with a difference of at least four carbons are prone to phase segregation.[22]

3.1.1.3. SAM Oxidation

Oxidation of alkanethiol SAM at gold may change the hydrophobicity and morphology of the surface. The thiolate layer oxidizes in air, even in the dark.[23] Several factors affect the oxidation of alkanethiol SAM on polycrystalline gold. The first factor is the morphology of the underlying gold. It is known that a decrease in the size of the grains, which decreases the amount of Au(111) on the surface, enhances the oxidation rate significantly.[23]

Another factor involved is the alkanethiol chain length [24]. SAMs formed by short-chain thiols ($m \leq 7$) have many disordered sites making thiols accessible for oxidation. SAM domain boundaries, which have more defects, are also active sites for oxidation.[24] Better van der Waals interactions between long-chain thiols ($m \geq 9$) make the SAM more difficult to penetrate, resulting in a lower oxidation rate.[24] The atmospheric ozone (O_3) level [24,25] is also reported to affect the oxidation of the SAM layer. It is suggested that O_3 oxidizes the thiolate layer by the interaction of the sulfur with singlet oxygen as a product of O_3 decomposition.[24,25]

Even though alkanethiol SAMs on gold exposed to ambient atmosphere have limited stability, in the case of alkanethiol SAMs kept in alkanethiol solution, the oxidized components of the SAMs can be quickly replaced by the alkanethiol chains placed in the solution.[24,25] Consequently, for prolonged SAM formation time, oxidation is not able to deteriorate the thiol layers. It is known that even after a period of two months of

immersion in air-saturated alkanethiol solutions, sulfonate, which is the main product of SAM oxidation, was not observed.[25] In addition to sulfonate, SAM oxidation results in sulfinate, sulfate and sulfite formation.[25] The final products of SAM oxidation, SO_4^{2-} and SO_3^{2-}, are due to scission of the S-C bond. These components can be easily replaced by thiols or washed off by water.[25]

3.1.2. K122-4 T4P and ΔK122-4 PNT

Pilins from different bacteria share structural similarities.[1,26] K122-4 pilin from *P. aeruginosa* consists of 150 amino acids including a long N-terminal α-helix wrapped in a four-stranded β-sheet.[27] Hydrophobic interactions between the helix and the β-strands, as well as the connecting loops anchor the helix across the β-sheet.[1] [27] Because the first 22 residues of K122-4 pilin (α1-N) are highly hydrophobic, the full-length pilin shows low water solubility.[1,10,26,27] The first 28 amino acids extend out of the β-sheet; therefore, deletion of these amino acids doesn't affect the structure of the rest of the molecule.[10] Fig. 3.5 shows a ΔK122-4 pilin. The α-helix, β-sheet and connecting loops are shown in blue, green and purple, respectively.

[1] The hydrophobic interface is comprised of residues Leu^{33}, Leu^{39}, Leu^{43}, Val^{47}, Ile^{50} and Phe^{51} of the α-helix with residues Val^{81}, Ala^{87}, Ile^{95}, Ala^{97}, Leu^{113}, Leu^{115}, Leu^{117}, Trp^{127} and Leu^{138}. These residues are mostly conserved.[27]

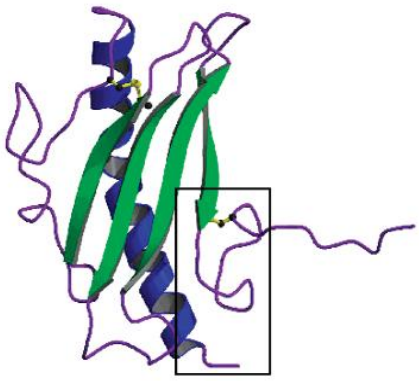

Fig. 3.5. ΔK122-4 pilin structure. The N-terminal α-helix, β-sheet- and coil regions are shown in blue, green and purple, respectively. The two disulfide bridges are shown in yellow. The receptor-binding domain of the pilin is boxed. "Reprinted with permission from (Audette, G. F.; Irvin, R. T.; Hazes, B. Crystallographic Analysis of the Pseudomonas aeruginosa Strain K122-4 Monomeric Pilin Reveals a Conserved Receptor-Binding Architecture. *Biochemistry*. **2004**, 43, 11427–11435.). Copyright (2004) American Chemical Society."

The outer surface of the molecule is mostly composed of polar residues.[27] D. W. Keizer *et al.* established their model for pilus formation based on electrostatic and hydrophobic interactions.[27] Pilins contain five distinct positive and negative regions.[27] The positively charged surface present on the face at the N terminus of the truncated α-helix interacts with the negatively charged surface present on the face at the C terminus of the α-helix. Moreover, hydrophobic interaction of the α-helices is another driving factor for pilus formation.[27] The monomers bind slightly out of register; hence, they form a helix with a left-handed twist. Fig. 3.6 shows electrostatic interactions among five K122-4 monomers to form one turn of a pilus.

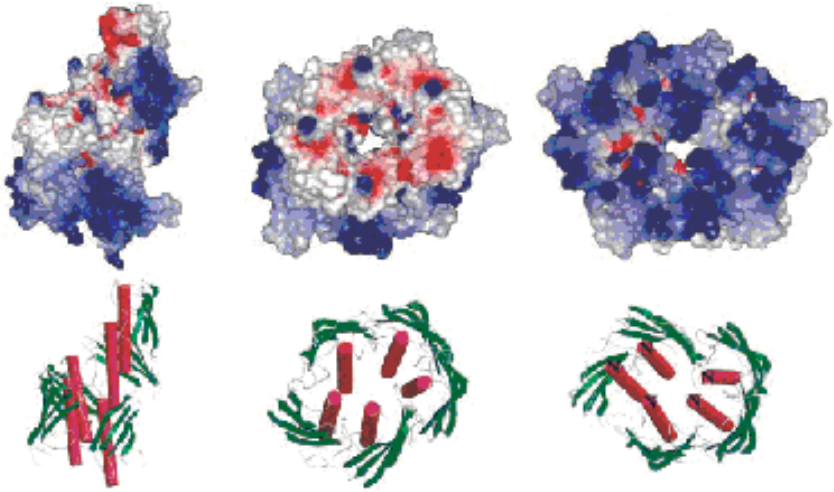

(a) (b) (c)

Fig. 3.6. (a) Side, (b) top and (c) bottom views of five ΔK122-4 pilins forming one turn of a helical pilus. Red and blue correspond to negatively and positively charged areas, respectively. Reprinted with permission from (Keizer, D. W.; Slupsky, C. M.; Kalisiak, M.; Campbell, A. P.; Crump, M. P.; Sastry, P. A.; Hazes, B.; Irvin, R. T.; Sykes, B. D. Structure of a Pilin Monomer from *Pseudomonas aeruginosa* Implications for the Assembly of Pili. *J. Biol. Chem.* **2001**, 276, 24186-24193). Copyright (2001) The American Society for Biochemistry and Molecular Biology."

Even though, normally, intact K122-4 pilins do not form fibers spontaneously, in the presence of hydrophobic compounds in the solution, truncated K122-4 pilins self-assemble to produce PNTs.[1,10] It is suggested that the PNT formation is triggered by association of hydrophobic parts of the monomers (the remaining part of the α-helices) at the hydrophobic molecules.[1,10]

ΔK122-4 protein nanotubes and K122-4 pili have some similarities: (a) antibodies that bind in particular to the side and the tip of T4P also bind to PNT, (b) both T4P and PNT bind to DNA, and biotic and abiotic surfaces, (c) ΔK122-4 PNT and K122-4 T4P have an outer diameter of ~5–6 nm, and (d) PNT does not bind to Congo red showing that the pilin subunits do not form a β-amyloid structure.[10] As a result of these observations, it

is suggested that ΔK122-4 PNT and T4P share a similar structure.[1,10] However, the length of PNTs, which can reach several hundred micrometers, is considerably longer than that of native pili (~10 μm).[10] Moreover, the truncated monomers form a hydrated channel with an inner diameter of 2 nm, while the central channel of a natural pilus has a diameter of 1.2 nm [1,10].

While ΔK122-4 pilin-based PNT formation in solution was reported [1,10], ΔK122-4 PNT formation through their attachment on a surface needs further investigation. In this research, self-assembled monolayers of different alkanethiols on Au(111) are used as a substrate to investigate the oligomerization of ΔK122-4 pilins from bacterium *P. Aeruginosa*. Hydrophobic end group of the alkanethiols, as well as the hydrophobicity of the chains, could assist pilin association and PNT formation.

Along with SAMs of pure thiols, mixtures of different alkanethiols were utilized to modify the surface of Au(111) with the goal of creating mixed alkanethiol layers, comprised of various alkyl chain lengths and functional groups, to control the surface properties, as well as to expose the chains. We also investigated the effect of SAMs defects on ΔK122-4 pilin oligomerization at the surfaces.

3.2. Experimental and Methodology

3.2.1. Materials and Reagents

Gold-coated borosilicate glass substrates with a chromium adhesion layer (250 ± 50 nm Au, 2.5 ± 1.5 nm Cr and 0.7 ± 0.1 mm glass) with 7 × 7 mm^2 surface area were purchased from Arrandee™. 1-Pentanethiol (98%), 1-octanethiol (98.5%), 1-decanethiol (96%), 16-

mercaptohexadecanoic acid (90%) and 6-mercaptohexanoic acid (90%) were obtained from Sigma-Aldrich and 1-tetradecanethiol (98%) was from Fluka Chemie AG. ΔK122-4 Pilin monomer solution was prepared by Professor G.F. Audette group, Chemistry, York University. The method of preparation is reported by G.F. Audette *et al*.[26]

3.2.2. Instrumentations

A commercial AFM instrument (Dimension 3100, NanoScope IIIa, Digital Instrument, USA) was employed to perform topographic measurements. (See section 2.2.2.2)

3.2.2.1. FT-IR External Reflection

A Nexus 870 Spectrometer (ThermoNicolet) equipped with 4X Beam Condenser (Harrick Scientific Corporation) in dry-air atmosphere was employed to collect infrared spectra with 0.96 cm^{-1} resolution. The instrument was purged with dry air half an hour before and while measurement. FT-IR external reflection spectra of self-assembled monolayers were obtained with liquid nitrogen-cooled MCT detector and a Variable Angle Specular Reflectance (VeemaxII) accessory. In external reflection spectroscopy, which is also known as specular reflectance, light is reflected from a mirror-like sample to record its spectrum. Bare Au(111) was used as the background. The bare gold substrate was cleaned freshly in H_2SO_4 (96%). Subsequently, it was annealed just before measuring the background spectrum.

3.2.2.2. Scanning Tunneling Microscope

STM imaging was performed using a Molecular Imaging PicoSPM. The experiments were carried out in constant current mode. The potential between the sample and the tip were controlled using a bipotentiostat (Picostat).

The main concept involved in STM is quantum tunneling[1]. Conductive STM tip scans the sample at a typical distance of 0.4-0.7 nm which is the equilibrium position between attractive and repulsive interactions.[28] At such a low distance, a bias (voltage difference) between the tip and the surface allows the electron to tunnel between them. The tunneling current is affected by the tip-surface distance, the applied voltage and the local density of states of the sample. A piezoelectric crystal, whose dimensions change electrically, adjusts the distance between the tip and the surface. (Fig. 3.7)

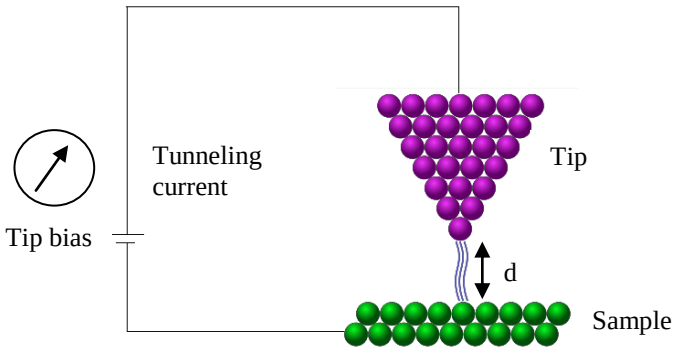

Fig. 3.7. Schematic diagram of an STM.

Two common modes of STM imaging are constant current and constant height modes.[29] In the constant current mode, a feedback loop adjusts the voltage to the piezoelectric to keep the tunneling current constant.[29] Therefore, the topographic image

[1] Quantum tunnelling refers to the quantum mechanical phenomenon where a particle tunnels through a barrier that it classically could not surmount.

is produced by the height variation, and it gives a constant charge density surface.[30] In constant height mode, the voltage and height are both held constant, while the current varies. Variations in the current, which can be related to the charge density, yield the image.[30]

3.2.3. SAM Preparation

To clean the gold substrates, we immersed them in H_2SO_4 (96%) for 5 min, rinsed with distilled water, flame annealed to an orange glow for a few minutes, and finally rinsed two times with Millipore water and ethanol.

SAMs were prepared by immersion of the Au(111) substrates in 1 or 2 mM ethanolic solutions of different alkanethiols at room temperature. Before the gold substrates were immersed in the alkanethiol solutions, they were deoxygenated for 20 minutes using argon. After incubation, the samples were rinsed with Millipore water and ethanol. For this study, long immersion times for SAM preparation (typically around 72 h) were chosen. Double-component alkanethiol SAMs were prepared via co-adsorption using ethanolic solution containing mixture of the alkanethiols.

3.2.4. ΔK122-4 Pilin Oligomerization at a SAM Surface

To oligomerize ΔK122-4 pilin-derived PNTs, the alkanethiol SAM on gold substrate was dipped in an aqueous solution containing 1 mg/mL of ΔK122-4 pilin monomers, 10 mM buffer Tris (2-amino-2-hydroxymethyl-propane-1,3-diol) and 200 mM NaCl at pH 7.4. Oligomerization was carried out at room temperature, while shaking the vial. Subsequently, the sample was rinsed thoroughly with deionized water and dried using

compressed nitrogen gas. In solution, ΔK122-4 pilin-derived PNT formation was triggered by 1-undecanethiol, as reported by G. F. Audette *et al*.[1]

3.3. Results and Discussion

Our preliminary results on ΔK122-4 pilin oligomerization were published by Professor G. F. Audette in 2009.[13] In this work, our initial findings on surface-initiated PNT growth were discussed. 1-Decanethiol-functionalized gold surface was used to trigger PNT formation. Using AFM imaging, the oligomerized PNTs were found to have an average diameter of 36 ± 3 nm and a length of up to several micrometers. In comparison with the reported values of ~6 nm for the diameter of native type IV pili [10], surface-derived PNTs were suggested to be clusters of multiple PNT filaments. However, additional controls have shown that those filaments originated most likely from the oligomerization in solution or from impurity that accumulated on the surface by repeatedly taking the sample in and out of the pilin solution.

The result section of this chapter covers: (a) the preparation and characterization of self-assembled monolayers of hydrophobic, hydrophilic, and various mixtures of hydrophobic and hydrophilic alkanethiols on gold, and (b) the investigation of ΔK122-4 pilin oligomerization at the above-mentioned SAMs.

3.3.1. Alkanethiol SAM Formation

In this section, characterization of the SAMs, prepared for our studies, will be presented. Table 3.1 summarizes the surfaces that were prepared to study surface-induced ΔK122-4 pilin oligomerization.

Table 3.1. Single- and double-component alkanethiol SAMs prepared in this study.

1	1-Pentanethiol
2	1-Octanethiol
3	1-Decanethiol
4	1-Tetradecanethiol
5	6-Mercaptohexanoic acid
6	16-Mercaptohexadecanoic acid
7	1-Octanethiol and 1-Decanethiol (50/50)
7	1-Pentanethiol and 1-Tetradecanethiol (50/50)
8	1-Pentanethiol and 16-Mercaptohexadecanoic acid (50/50)
10	1-Decanethiol and 6-Mercaptohexanoic acid (10/90 and 50/50)
11	1-Tetradecanethiol and 6-Mercaptohexanoic acid (10/90, 30/70 and 50/50)

Each SAM-modified surface was imaged by AFM, and the quality of the prepared SAMs was assessed using FT-IR. Fig. 3.8a-d show typical infrared spectra of the alkanethiol SAMs on Au(111). These spectra, covering the range of 2800–3000 cm^{-1}, show the FT-IR external reflection spectra of 1-pentanethiol-, 1-octanethiol-, 1-tetradecanethiol-derived SAMs, as well as a SAM derived from a 50/50 mixture of 1-tetradecanethiol and 6-mercaptohexanoic acid on Au(111).

The stretching mode bands of CH are assigned in the above-mentioned region. The band observed at 2955-2959 cm^{-1} is assigned to the CH_3 asymmetric in-plane CH stretching mode, noted as υ_a (CH_3, ip), and the band at 2872-2873 cm^{-1} is assigned to the CH_3 symmetric CH stretching mode, υ_s (CH_3, FR). The bands at 2918-2920 cm^{-1} and 2849-2850 cm^{-1} are assigned to the υ_a and υ_s CH_2 stretching modes, respectively. The location

of these bands is very sensitive to the lateral interactions between alkanethiol chains. For alkanethiols with longer chains, better lateral interactions shift the bands to lower wavenumbers. For example, the peak of the υ_a and υ_s CH_2 for a crystalline polymethylene chain occurs at 2920 and 2850 cm^{-1}, whereas for the liquid state they appear at 2928 and 2856 cm^{-1}, respectively.[31,32] Observation of the bands at 2918-2920 cm^{-1} and 2849-2850 cm^{-1} for the prepared SAMs confirmed the formation of well-packed SAMs with a crystalline structure. In addition to the chain length, having double component SAMs affects the lateral interactions among the alkanethiols. For instance, even though the bands at 2919 cm^{-1} and 2958 cm^{-1}, assigned for the υ_a CH_2 and CH_3 for 1-pentanethiol SAM, respectively shift to 2918 cm^{-1} and 2955 cm^{-1}, respectively for the 1-tetradecanethiol SAM, having a double component SAM of 50/50 1-tetradecanethiol and 6-mercaptohexanoic acid reduces the lateral interaction and results in blue shifts to 2920 cm^{-1} and 2958 cm^{-1}, respectively which are comparable to the bands of 1-pentanethiol SAM.

Fig. 3.9 shows the 5 μm × 5 μm AFM image of a Au(111) textured surface. This surface was prepared by thermal annealing to reveal the Au(111) texture. The image shows typical gold grains with relatively smooth top surfaces that display atomically flat Au(111) terraces.

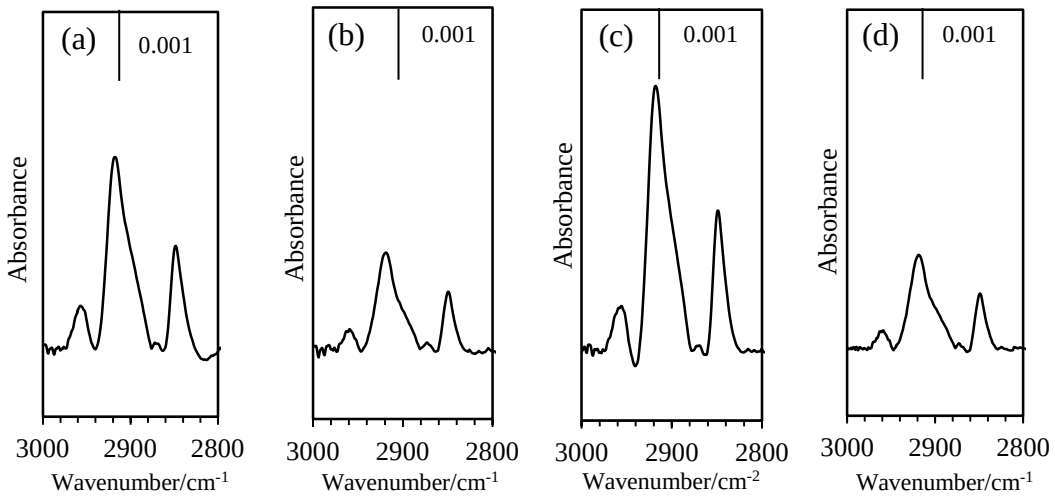

Fig. 3.8 Infrared external reflection spectra of self-assembled monolayers of (a) 1-pentanethiol, (b) 1-octanethiol, (c) 1-tetradecanethiol and (d) 50/50 mixture of 1-tetradecanethiol and 6-mercaptohexanoic acid at Au(111).

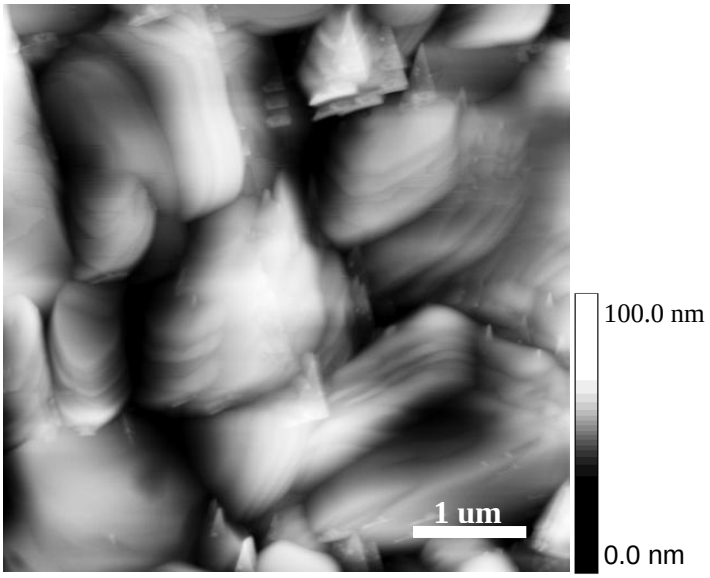

Fig. 3.9. 5 μm × 5 μm Tapping-mode AFM image of an Au(111) surface prepared by thermal annealing.

As a typical AFM image of alkanethiol SAM on a Au(111) textured surface, Fig. 3.10 shows the 100 nm × 100 nm tapping-mode AFM image of a 1-octanethiol-modified Au substrate. The average step height, 1.9 ± 0.5 Å, is comparable to 2.35 Å, the step height

expected for the height difference between two Au(111) atomic layers [33]. This image shows that the alkanethiol self-assembly produced a smooth layer at the Au surface with no effect on the step height, revealing that the thiol layer followed the morphology of the surface, and that a smooth monolayer was formed.

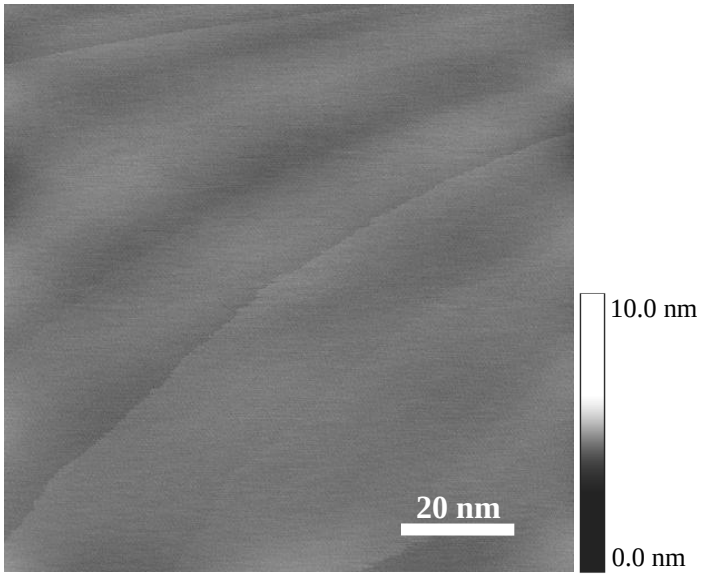

Fig. 3.10. 100 nm × 100 nm Tapping-mode AFM image of 1-octanethiol SAM on Au(111). In order to prepare the surface, the annealed gold on glass substrate was immersed in 2 mM 1-octanethiol solution for 1 min.

Fig. 3.11 shows the STM image of a 1-pentanethiol-modified Au(111) textured substrate. The image displays wide terraces covered by circular areas of lower height than the terrace plane. The size distribution histograms of the depth and full width at half-minimum of the surface holes are shown in Fig. 3.11b and 3.11c. The holes have an average depth of 0.7 ± 0.2 Å and width at half-minimum of 13 ± 3 Å. In the thiolate layer, pits with depth of 2.4 Å are consistent with the gold vacancy islands.[18] Missing thiolate molecules are another source of the pits. However, the neighbours of the missing

chains relax into the void space; hence they decrease the depth of the holes and increase their width.[21] .

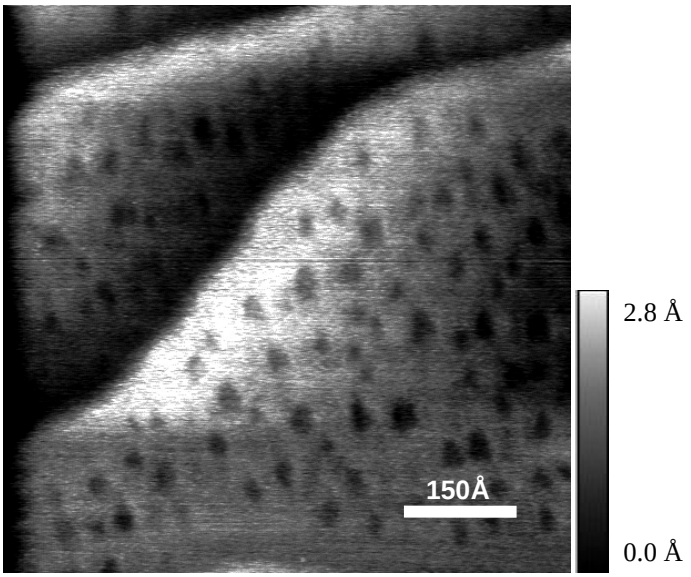

(a)

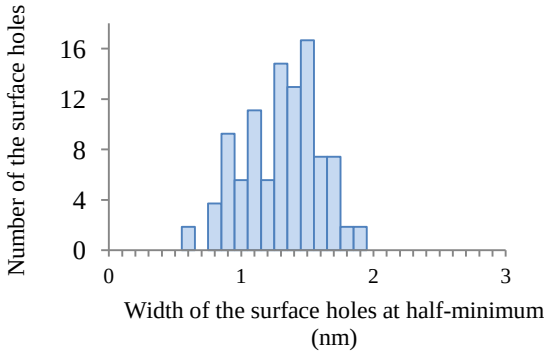

(b)

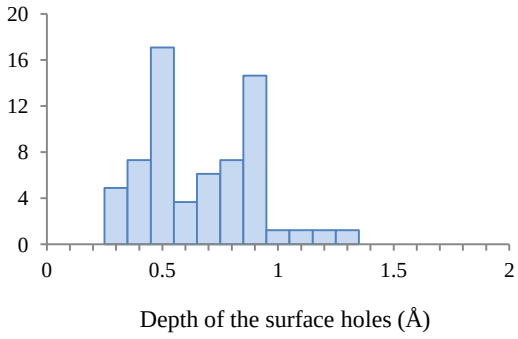

(c)

Fig. 3.11. 1-Pentanethiol SAM on Au(111). (a) 75 nm × 75 nm STM image at 0.54v bias, (b) Histogram of the width at half minimum of the surface holes. (c) Histogram of the surface holes depth.

3.3.2. SAM Stability in the Solution Used for Pilin Oligomerization

We were interested in investigating the SAMs stability in the solution used for pilin oligomerization. Therefore, prior to pilin oligomerization, the SAM stability in the buffer solution (10 mM Tris buffer and 200 mM NaCl at pH 7.4) was studied by STM. The buffer solution has the same components as the solution used to carry out pilin oligomerization, with the only difference being that the buffer solution does not contain any pilin.

Fig. 3.12a shows the STM image of a SAM on gold freshly prepared from a 50/50 mixture of 1-tetradecanethiol and 6-mercaptohexanoic acid. The average pinhole depth and full width at half-minimum are 8 ± 2 Å and 7 ± 3 Å, respectively. Fig. 3.12b shows the same surface after 3 days of immersion in the buffer solution. After immersion, the sample was rinsed, dried with a stream of N_2 gas, and imaged using STM in air. Immersion in the solution increased the pinhole depth and full width at half-minimum from 8 ± 2 Å and 7 ± 3 Å to 9 ± 2 Å and 8 ± 3 Å, respectively. However, these variations are very small and within experimental errors and show that immersion in the buffer solution did not affect the surface features significantly.

The layer formed by a mixture of 50/50 1-tetradecanethiol and 6-mercaptohexanoic acid showed deeper pinholes than those formed at the 1-pentanethiol SAM. This might be attributed to the presence of longer-chain thiols on the latter surface. On the other hand, the average pinhole width of the 1-pentanethiol SAM is larger than that of the mixed surface. The 1-pentanethiol SAM is more likely to have patches with a liquid-like phase

in the c (4 × 2) structure.[14] The liquid-like patches appear lower in height than the solid-like structure of c (4 × 2).

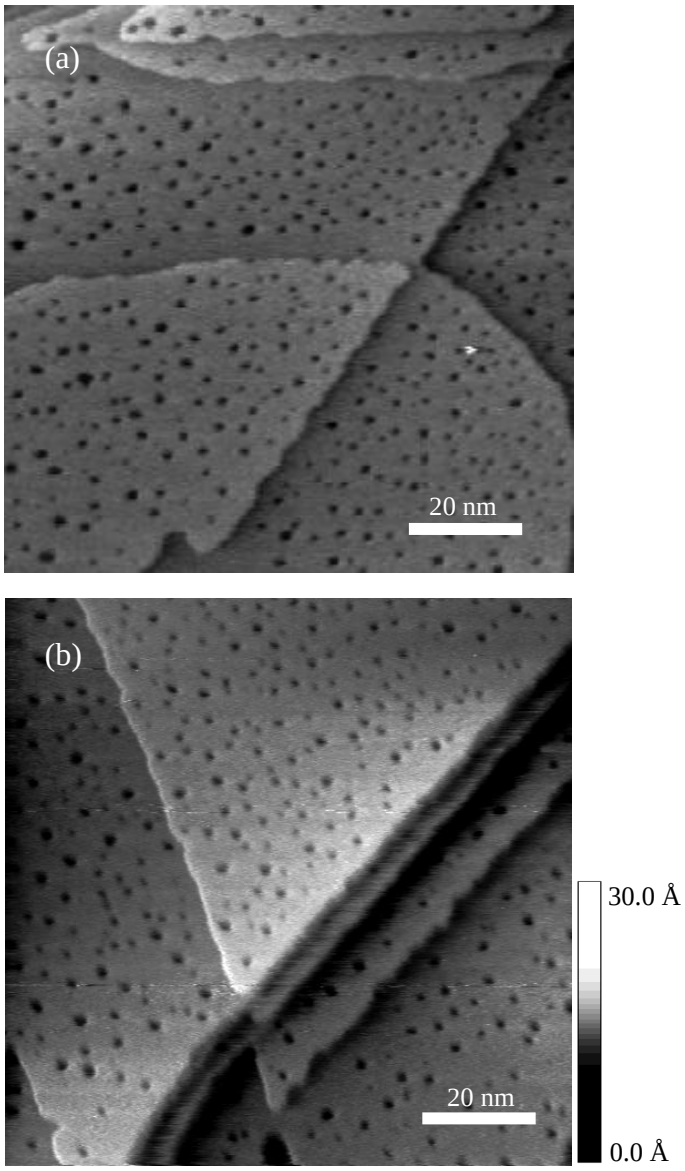

Fig. 3.12. (a) STM images of a double-component SAM of 50/50 1-tetradecanethiol and 6-mercaptohexanoic acid on Au(111) at –0.08 V bias. The SAM surface was prepared through immersion of an annealed gold on glass substrate in 2 mM solution of 50/50 1-tetradecanethiol and 6-mercaptohexanoic acid for 72 h. (b) STM image of the same surface after 72 h immersion in the solution of 10 mM Tris and 200 mM NaCl, at -0.10 V bias.

3.3.3. ΔK122-4 Pilin Oligomerization at Alkanethiol SAMs on Au(111)

Samples of different alkanethiol self-assembled monolayers on Au(111) were immersed in ΔK122-4 pilin solution for pilin oligomerization. Initially, to trigger ΔK122-4 pilin oligomerization, double-component SAMs, consisting of a mixture of long hydrophobic and short hydrophilic thiols, were used. These experiments were carried out with the goal of controlling the PNT growth site density by changing the hydrophobic chain percentage. The end groups of the hydrophobic chains were extended out and were aimed to facilitate association of the hydrophobic core of ΔK122-4 pilins. In addition to the hydrophobic terminal groups, the hydrophobicity of the long chains, exposed to the solution, may assist pilin association to start oligomerization. Fig. 3.13 shows AFM images of a double-component SAMs that consist of 10/90 1-decanethiol and 6-mercaptohexanoic acid, after immersion in 1 mg/mL ΔK122-4 pilin solution for different periods of 24, 37, 60 and 72 h. Contrary to our expectation, only a few filaments were observed. Moreover, no meaningful correlation between the number of filaments and the duration of the surface exposure to the monomer solution was observed. However, some pilin aggregations, which mostly occurred at the step edges, were detected. Two attempts were made to increase the possibility of PNT formation. The hydrophobicity of the surface was enhanced by increasing the methyl-terminated thiol percentage in the SAM. Moreover, the difference between the chain lengths of the hydrophobic and hydrophilic thiols was increased to make the hydrophobic chains more accessible to the pilins. Mixtures of 1-tetradecanethiol and 6-mercaptohexanoic acid, at different ratios of 10/90,

30/70 and 50/50, were used to investigate ΔK122-4 pilin oligomerization. The surfaces were exposed to the pilin solution for 36 and 72 h.

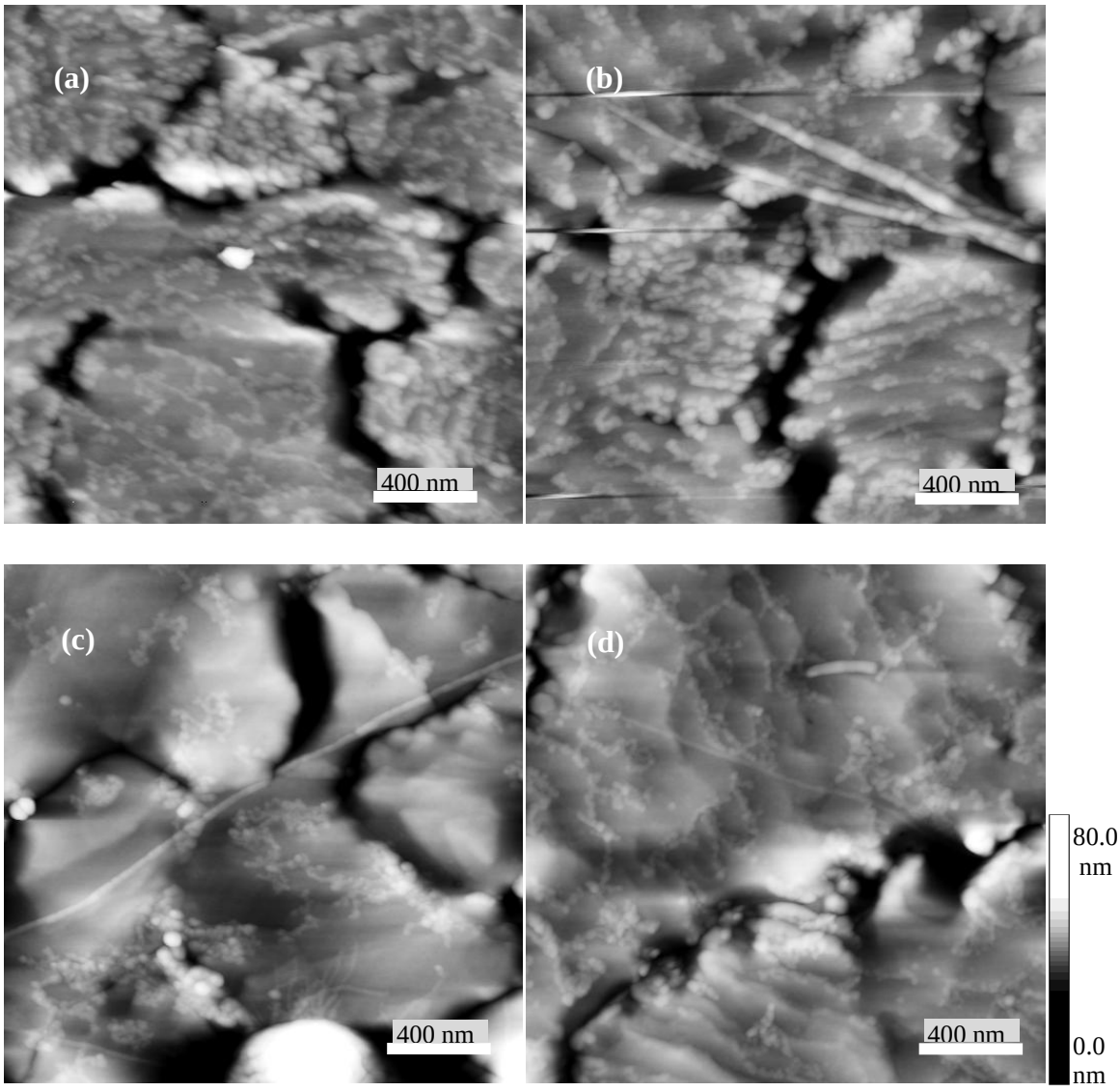

Fig. 3.13. 2 μm × 2 μm Tapping-mode AFM images of a double-component SAM of 10/90 1-decanethiol and 6-mercaptohexanoic acid on gold, after exposure to 1 mg/mL K122-4 pilin solution for (a) 24 h, (b) 37 h, (c) 60 h and (d) 72 h. The SAMs were prepared through immersion of an annealed gold on glass substrate in 1 mM solution of the alkanethiols for 1 h.

The AFM images of the above-mentioned surfaces are shown in Fig. 3.14a-f. Long filaments, along with pilin aggregations, mostly occurred at step edges and grain boundaries, are visible in Fig. 3.14a. However, only a very small number of filaments were detected. Note that features, such as the ones shown in the boxed area of Fig. 3.14b, are attributed to the pilin oligomerization rather than SAM oxidation. This was inferred, since such features were not observed at the surface when we performed a control experiment on SAM stability in the pilin solution (Fig. 3.12).

Both Fig. 3.13 and Fig. 3.14a show surfaces containing 10% hydrophobic chains. However, the differences between the numbers of carbon in the alkanethiols used to form these layers are equal to four and eight carbons, respectively. Compared to Fig. 3.14a, Fig. 3.14b and 3.14c show pilin oligomerization at a more hydrophobic SAM containing 30/70 1-tetradecanethiol and 6-mercaptohexanoic acid. After 36 h, only some aggregations formed. However, some elongated structures were observed after 72 h (Fig. 3.14c).

Increasing the hydrophobic/hydrophilic ratio to 50/50 resulted in formation of a web pattern along with some branching filaments (see Fig. 3.14d and 3.14f), even after 36 h. The boxed area of Fig. 3.14d is magnified in Fig. 3.14e, revealing a web-patterned region. The circled and boxed areas of Fig. 3.14f are fully covered by the nanoweb and branching filaments, respectively. Fig. 3.14f reveals that the filaments are mostly initiated at the grain boundaries.

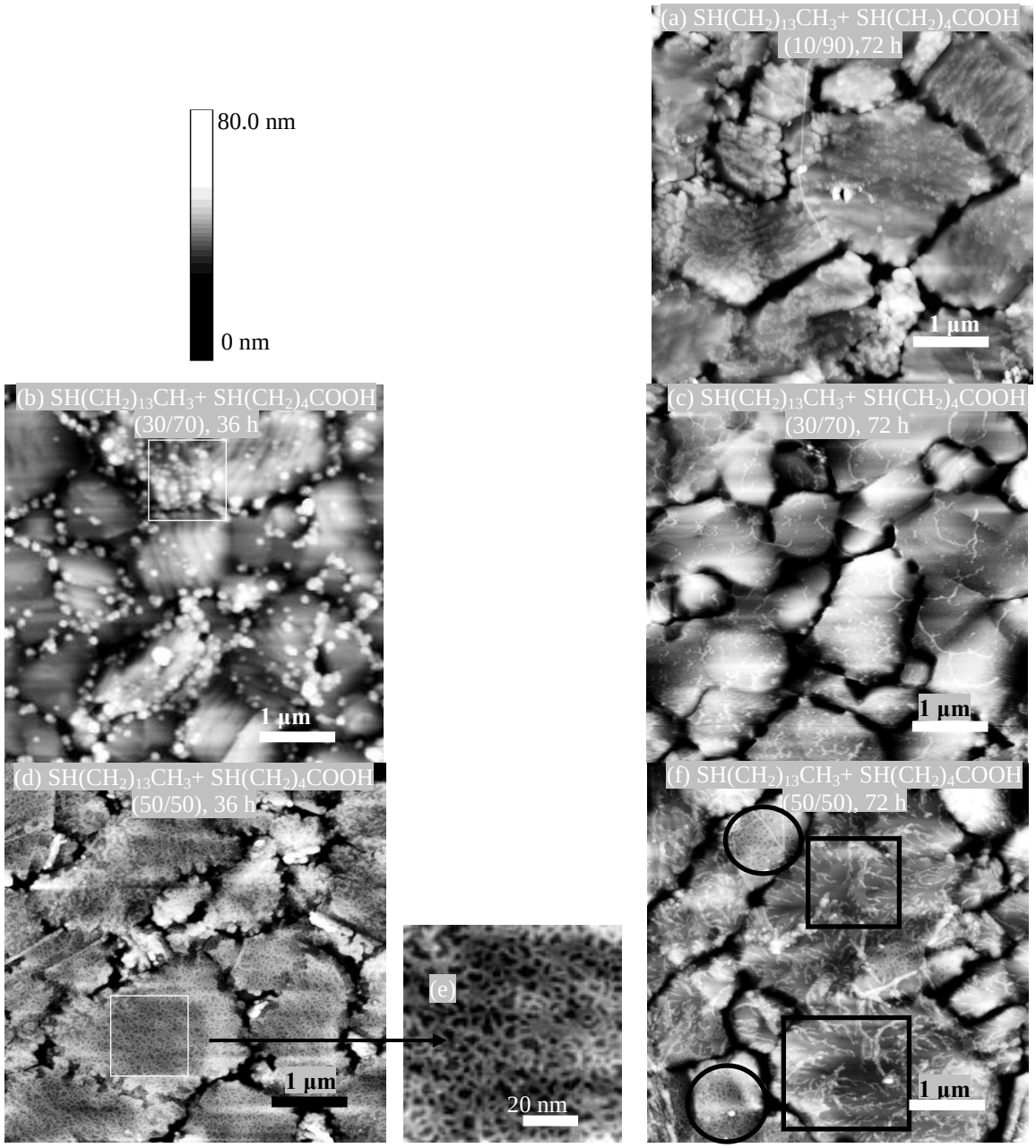

Fig. 3.14. 5 µm × 5 µm Tapping-mode AFM images of ΔK122-4 pilin oligomerization at double-component SAMs of 1-tetradecanethiol and 6-mercaptohexanoic acid. SAMs were prepared through immersion of the annealed gold substrates in 2 mM solution of the alkanethiols for 1 h. Subsequently, the surfaces were immersed in 1 mg/mL K122-4 pilin solution. The ratio of 1-tetradecanethiol and 6-mercaptohexanoic acid and the time of immersion in pilin solution were (a) 10/90 and 72 h, (b) 30/70 and 36 h, (c) 30/70 and 72 h, (d) 50/50 and 36h, and (f) 50/50 and 72 h, respectively. The boxed area (198 nm × 201 nm) of (d) is magnified in (e). Some pilin aggregations are shown in the boxed area of (b).

To illustrate the features formed at hydrophilic surfaces, Fig. 3.15a-c show tapping-mode AFM images of a 6-mercaptohexanoic acid SAM, a 16-mercaptohexadecanoic acid SAM, and annealed bare gold, immersed in 1 mg/mL K122-4 pilin solution for 3 days. Contrary to the hydrophobic SAMs, these hydrophilic surfaces resulted in pilin random aggregation covering the whole surface.

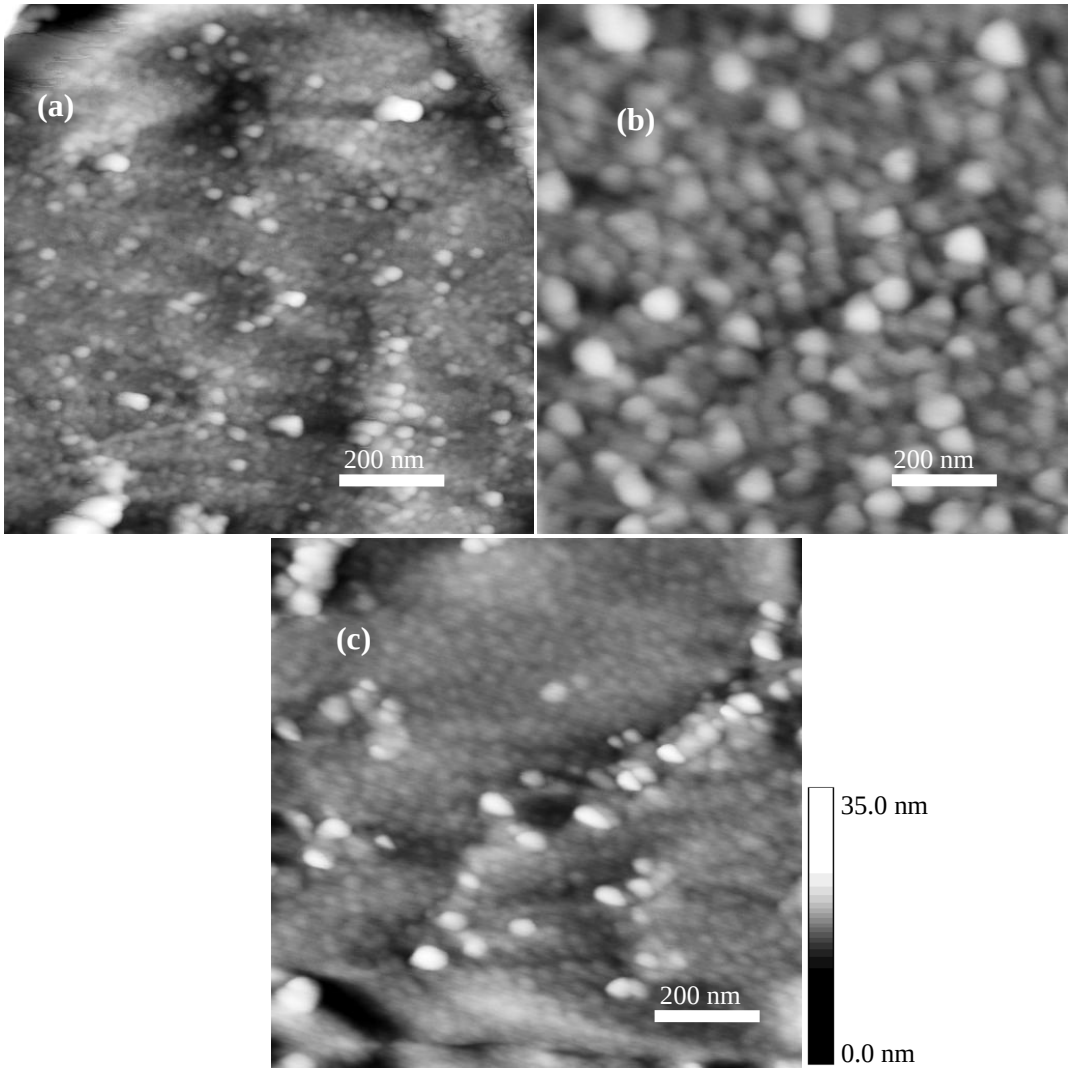

Fig. 3.15. 1 μm × 1 μm Tapping-mode AFM images of different hydrophilic surfaces of (a) 6-mercaptohexanoic acid SAM, (b) 16-mercaptohexadecanoic acid SAM and (c) bare gold after 3 days exposure to 1 mg/mL K122-4 pilin solution. The SAMs were prepared through immersion of annealed gold on glass substrates in 2 mM alkanethiol solution for 72 h.

To investigate if the end group of the longer component of the SAM had an effect on the web pattern formation, a double-component SAM containing a mixture of long hydrophilic and short hydrophobic thiols was employed. Fig. 3.16 shows the tapping-mode AFM image of a SAM comprised of 16-mercaptohexadecanoic acid and 1-pentanethiol (50/50) on Au(111), immersed in 1 mg/mL ΔK122-4 pilin solution for 72 h. Both Fig. 3.14 and Fig. 3.16 show AFM images of a surface containing 50% hydrophobic chains, but unlike Fig. 3.14, Fig. 3.16 shows the AFM image of a surface composed of short hydrophobic and long hydrophilic thiols. When this image is analyzed, one only detects pilin aggregations, while AFM images in Fig. 3.14d and Fig. 3.14f show the web pattern and some branching filaments.

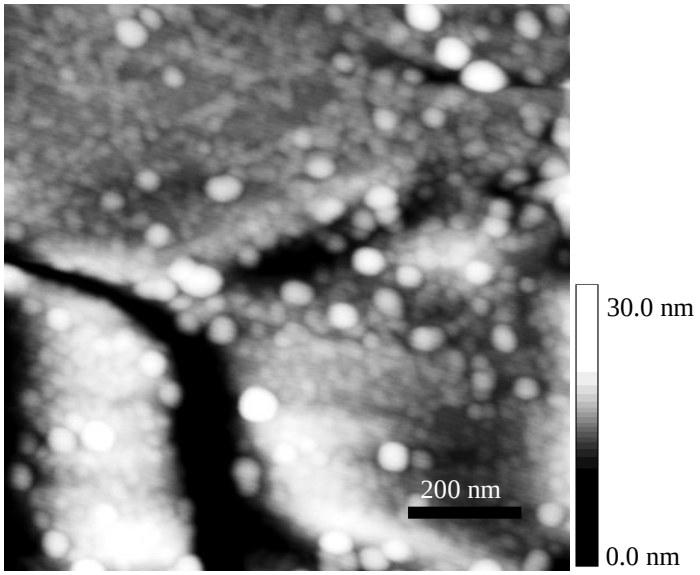

Fig. 3.16. 1μm × 1μm Tapping-mode AFM image of a double-component SAM of 16-mercaptohexadecanoic acid and 1-pentanethiol (50/50) on Au(111) after 72 h immersion in 1 mg/mL ΔK122-4 pilin solution. The SAM was prepared through immersion of an annealed gold on glass substrate in 2 mM alkanethiol solution for 1 h.

In further investigations, different hydrophobic single-component SAMs were utilized to initiate ΔK122-4 pilin oligomerization. Fig. 3.17a-c show the tapping-mode AFM images of pilin oligomerization at different hydrophobic surfaces of 1-pentanethiol, 1-decanethiol and 1-tetradecanethiol SAMs, immersed in the pilin solution for 72 h. Similar to the double-component SAM containing 50/50 1-tetradecanethiol and 6-mercaptohexanoic acid (3.14d and 3.14f), the above-mentioned surfaces resulted in the formation of a web pattern.

I have to mention that a few long filaments were observed at both hydrophobic and hydrophilic layers. For instance, Fig. 3.18a and 3.18b show some ΔK122-4 pilin-based filaments at two single-component 1-tetradecanethiol (hydrophobic) and 16-mercaptohexadecanoic acid (hydrophilic) SAMs, immersed in the oligomerization solution for 72 h. The ΔK122-4 pilin-based filaments are indicated by arrows. To identify the origin of these filaments, a control experiment was carried out. Fig. 3.19a and 3.19b show the tapping-mode AFM images of two 1-octanethiol SAM substrates, immersed in the oligomerization solution for 3 days. The first surface was imaged after 3 days, while the second one was imaged after every 24 h, and then returned to the oligomerization solution. Before and after each imaging, the sample was rinsed with distilled water. While Fig. 3.19b shows several long filaments, Fig. 3.19a detected only a few. This observation supports the idea that during sample handling, any trace of hydrophobic impurities was able to trigger PNT formation.

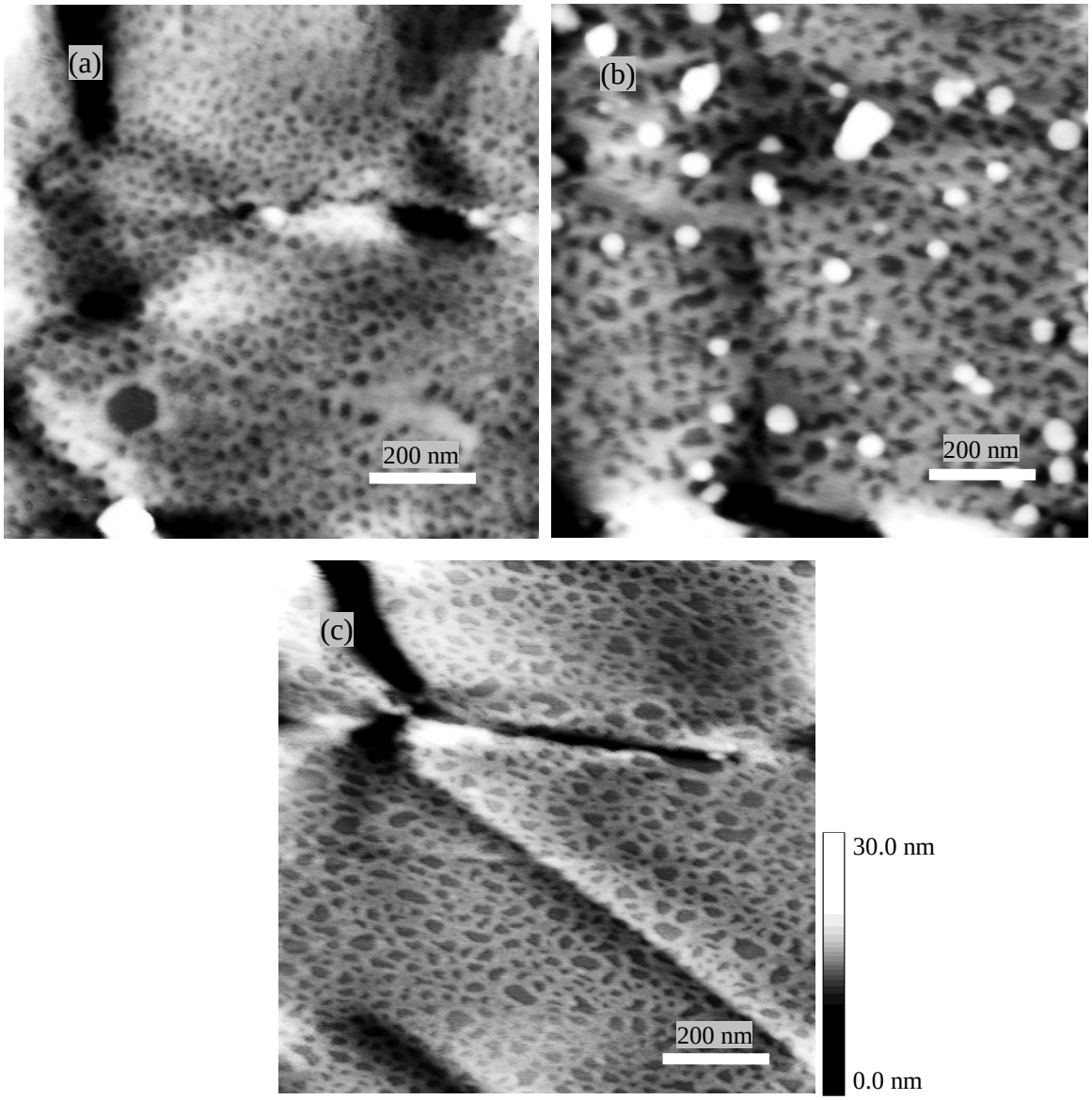

Fig. 3.17. 1 μm × 1 μm Tapping-mode AFM images of ΔK122-4 pilin-based web patter formation at different hydrophobic surfaces of (a) 1-pentanethiol, (b) 1-decanethiol and (c) 1-tetradecanethiol SAMs. The SAMs were prepared through immersion of annealed gold on glass substrates in 2 mM alkanethiol solutions for 72 h.

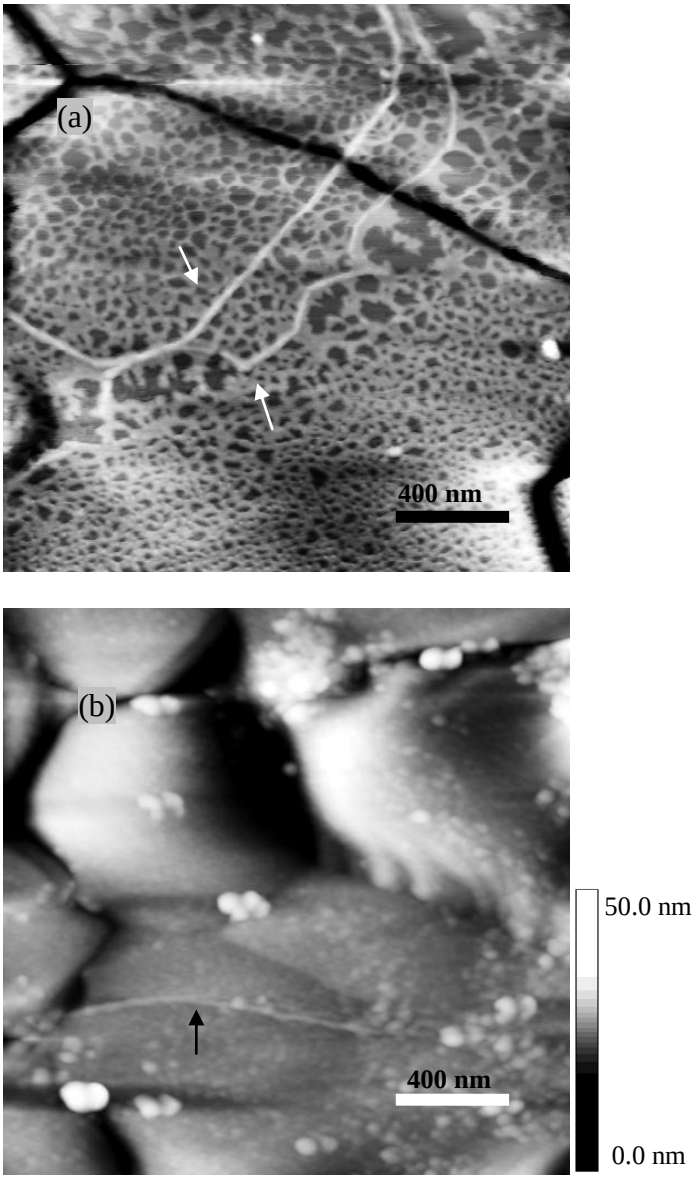

Fig. 3.18. 2µm × 2 µm Tapping-mode AFM images of ΔK122-4 PNTs at (a) 1- tetradecanethiol and (b) 16-mercaptohexadecanoic acid SAMs on gold after 3 days immersion in 1 mg/mL ΔK122-4 pilin solution. The SAMs were prepared via immersion of annealed gold on glass substrates in 2 mM alkanethiol solutions for 72 h. Arrows show ΔK122-4 pilin-based filaments.

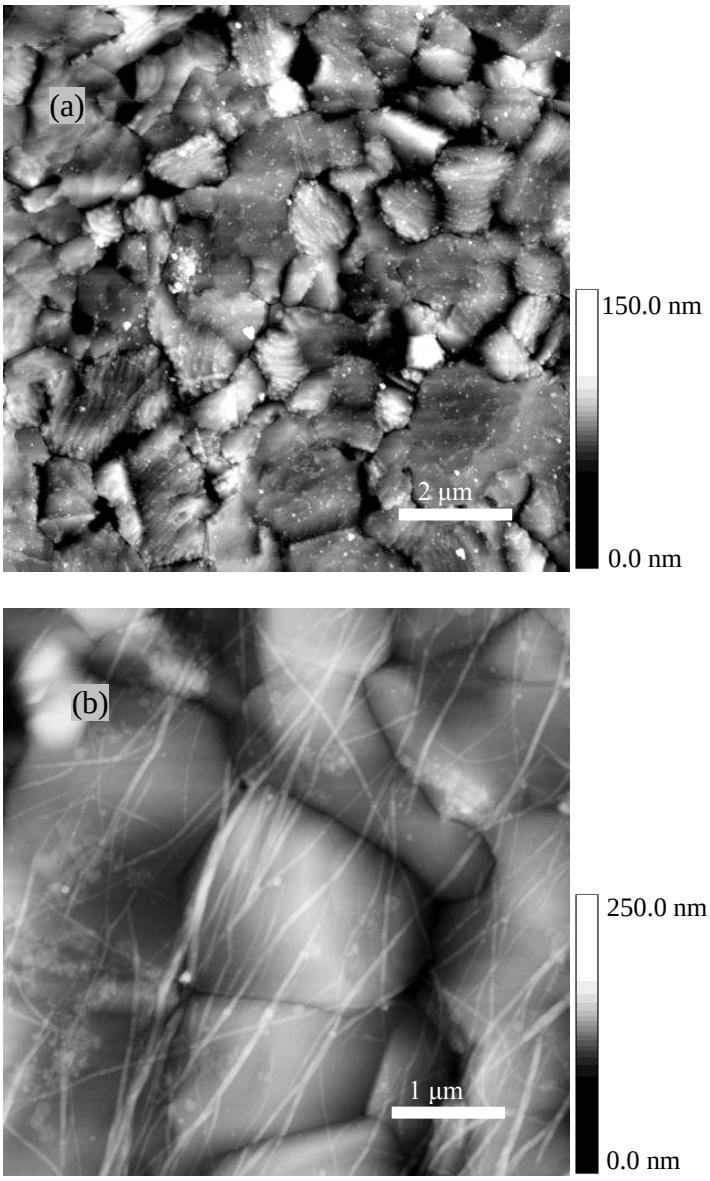

Fig. 3.19. (a) Tapping-mode AFM images of 1-octanethiol SAM on gold substrates after 3 days exposure to 1 mg/mL ΔK122-4 pilin solution. The surface shown in (b) was taken out and imaged after each day. The surface was rinsed with distilled water and returned to the monomer solution after each imaging. The SAMs were prepared through immersion of the annealed gold on glass substrates in 2 mM 1-octanethiol solution for 5 min.

Table 3.2 shows the surface coverage and thickness of the web pattern at different hydrophobic single- and double-component SAMs. The web coverage and thickness of the hydrophobic surfaces are in the range of 52-71% and 3.2–6.1 nm, respectively. As shown in Fig. 3.20, the coverage and nanoweb thickness are not affected by the length of the alkanethiols or the SAM being single- or double-component.

Table 3.2. Surface coverage and thickness of the ΔK122-4 pilin-based web pattern formed at different hydrophobic alkanethiol SAMs on Au(111).

SAM	Thickness of ΔK122-4 pilin layer (nm)	Surface coverage of ΔK122-4 pilin layer (%)
1-Pentanethiol	4 ± 1	73 ± 5
1-Octanethiol	4 ± 1	67 ± 8
1-Decanethiol	3.6 ± 0.5	68 ± 16
1-Tetradecanethiol	3.5 ± 0.9	67 ± 7
1-Tetradecanethiol and 1-Pentanethiol (50/50)	3.6 ± 0.4	64 ± 10
1-Tetradecanethiol and 6-mercaptohexanoic acid (50/50)	5 ± 1	70 ± 5
1-Decanethiol and 6-mercaptohexanoic acid (50/50)	3.6 ± 0.4	75 ± 2

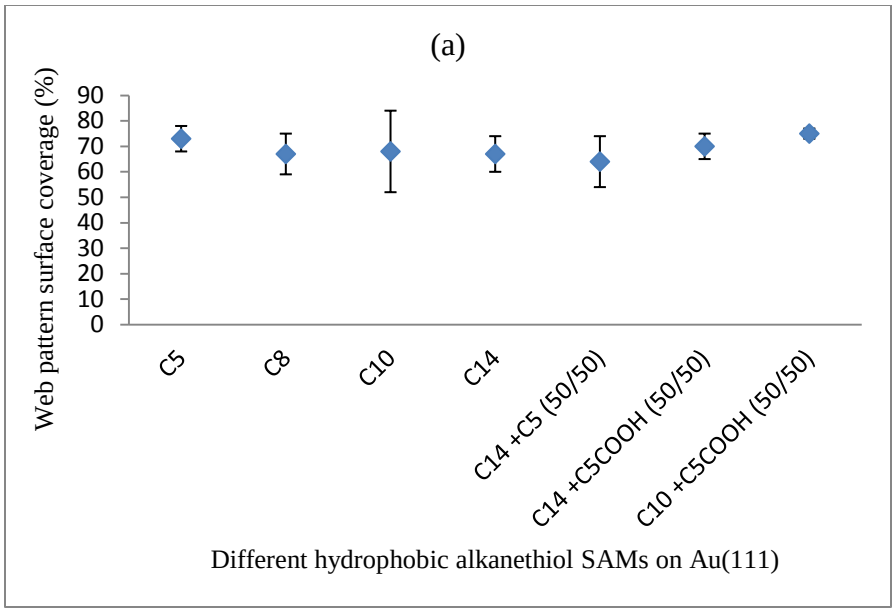

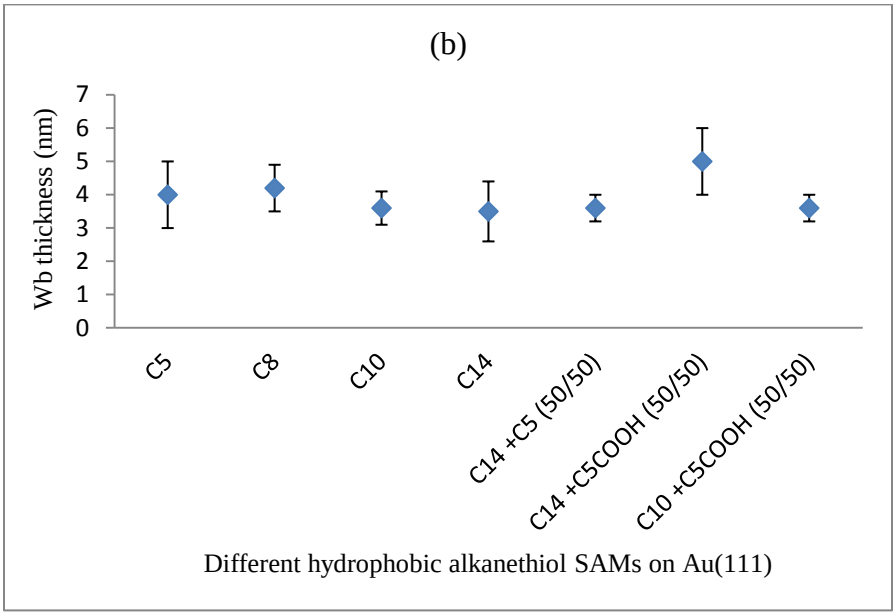

Fig. 3.20. Graphic presentation of the (a) surface coverage and (b) thickness of the ΔK122-4 pilin-based web pattern formed at different hydrophobic alkanethiol SAMs on Au(111) after 72h immersion in the pilin solution. The employed surfaces are 1-pentanethiol (C_5), 1-octanethiol (C_8), 1-decanethiol (C_{10}), 1-tetradecanethiol (C_{14}), 1-tetradecanethiol and 1-pentanethiol (50/50), 1-tetradecanethiol and 6-mercaptohexanoic acid (50/50), and 1-decanethiol and 6-mercaptohexanoic acid (50/50) SAMs.

We observed that at the hydrophilic 6-mercaptohexanoic acid SAM, 16-mercaptohexadecanoic acid SAM and annealed bare gold, ΔK122-4 pilins aggregated (Fig. 3.15a-c), whereas, a web pattern was detected at different hydrophobic 1-pentanethiol, 1-decanethiol and 1-tetradecanethiol SAMs (Fig. 3.17a-c). Double-component SAMs of 1-tetradecanethiol and 6-mercaptohexanoic acid with the ratio of 30/70 and 50/50 (Fig. 3.14c-f) were also able to trigger pilin oligomerization. However, at mixed SAMs of 10/90 1-decanethiol and 6-mercaptohexanoic acid (Fig. 3.13), and 10/90 1-tetradecanethiol and 6-mercaptohexanoic acid (Fig. 3.14a), ΔK122-4 pilins aggregated. These observations suggest that in order to trigger ΔK122-4 pilin oligomerization, it is necessary to have a SAM containing more than 10-30% hydrophobic component. Pilin aggregation at the 50/50 16-mercaptohexadecanoic acid and 1-pentanethiol SAM (Fig. 3.16) reveals that in addition to the percentage of the hydrophobic component, accessibility to the hydrophobic component is important. In the above-mentioned surface, the long hydrophilic 16-mercaptohexadecanoic acid made the short-chain 1-pentanethiol inaccessible to the pilins. It is also inferred that the hydrophobic body of the longer chains is not able to start oligomerization by itself; an accessible hydrophobic terminal group is required. Proper control experiments were also carried out to show that the observed features at hydrophobic and hydrophilic surfaces are not linked to SAM oxidation. As shown in Fig. 3.12, such features were not observed at the double-component SAM of 50/50 1-tetradecanethiol and 6-mercaptohexanoic acid, immersed in the control solution for 72 h.

The web pattern formed at the hydrophobic surfaces (Fig. 3.14, 3.17 and 3.18a) reveals the importance of the surface hydrophobicity in initiating ΔK122-4 pilin oligomerization. In order to investigate the mechanism of pilin oligomerization, two observations guided us. As shown in Fig. 3.13 and 3.14a, step edges are active sites in adsorbing the monomers. Fig. 3.14f demonstrates that grain boundaries also contributed to PNT initiation. Consequently, when a hydrophobic surface is exposed to ΔK122-4 pilin solution, there is a competition between different sites of the surface to adsorb the monomers and start pilin oligomerization.

At step edges and grain boundaries, self-assembled alkanethiol monolayers are faulted, and chains become more accessible to be surrounded by monomers to trigger pilin oligomerization. This suggests that in addition to the alkanethiol end group hydrophobicity, the accessibility of the chains, which are also hydrophobic, can facilitate ΔK122-4 pilin oligomerization.

The importance of surface hydrophobicity suggests that the mechanism, which governs ΔK122-4 PNT formation in a solution containing hydrophobic molecules, also controls surface ΔK122-4 pilin oligomerization. Therefore, it is concluded that hydrophobic association of the remaining part of the ΔK122-4 pilins α-helices is the main factor involved in surface pilin oligomerization. This hydrophobic association is motivated by water exclusion from the hydrophobic parts. Moreover, electrostatic interaction between the oppositely charged areas of monomers assists PNT formation.

The mechanism of the ΔK122-4 pilin-based web pattern formation at a hydrophobic surface can be enlightened by ΔK122-4 pilin oligomerization in solution. The TEM

images of Fig. 3.1a and 3.1b illustrate the formation of two thick filaments with average diameters of 23 ± 3 nm and 16 ± 2 nm, respectively along with a single PNT with a diameter of 8 ± 1 nm (shown by arrows in Fig. 3.1b). These filaments are formed because of ΔK122-4 pilin oligomerization in a solution containing 1- undecanethiol. If the thick filaments are made of bundles of ΔK122-4 PNTs, the same process may be involved in the development of the web pattern.

According to our hypothesis, adjacent tubes with the same direction can stick together to form a bundle. On the other hand, once joined, the tubes developing in different directions may grow in a new direction. When this process occurs repeatedly, it results in the nanoweb formation. Freedom of the tubes in the solution enables them to attach together along their whole length. On the other hand, when anchored to the surface from one side, the tubes do not possess such freedom.

Fig. 3.1c shows a branching filament developed due to the ΔK122-4 pilin oligomerization in solution. Fig. 3.14c and 3.14d illustrate that branching of filaments occurs at the surface too. In a crowded area, branching of the filaments could also give rise to a web pattern. While a single pilin-based PNT or a bundle of the filaments grows, there is a competition between their body and their terminus to adsorb the free monomers. Adsorption of the monomers at their body results in branching, while elongation is due to the pilin adsorption at the tip. Continuous filament branching, along with their joining each other, results in the web pattern formation.

A few long PNTs, observed at both hydrophobic and hydrophilic layers, are suggested to be initiated in the solution. Surfaces shown in Fig. 3.18a and 3.18b are examples of

hydrophobic (1-tetradecanethiol) and hydrophilic (16-mercaptohexadecanoic acid) layers reflecting this observation. In our preliminary research, we assumed that they originated at the surface.[13]

Alkanethiol self-assembled monolayers on gold are dynamic.[14] When exposed to the pilin solution, some of the alkanethiol molecules can enter the solution and start pilin oligomerization. Moreover, any trace of hydrophobic impurities can initiate the tube formation. Comparison between Fig. 3.19a and 3.19b justifies this explanation. The surface shown in Fig. 3.19a was imaged only once after three days of immersion in ΔK122-4 pilin solution. On the other hand, the surface shown in Fig. 3.19b was imaged twice before the final imaging on day three. The latter surface shows many long filaments, similar to the solution-based ΔK122-4 PNTs. Although the surface was rinsed with distilled water before returning the sample to the protein solution, it is conceivable that the sample handling and imaging introduced enough hydrophobic impurities on the sample to initiate ΔK122-4 PNT formation in solution once the sample was returned to the solution. Via insertion of the surface to the solution, some of the solution-based PNTs bound to the surface. Because of their different appearances, these solution-initiated filaments, and the surface-based web pattern can be easily recognized. As shown in Fig. 3.20a and 3.20b the coverage and thickness of the nanoweb formed at different single- and double-component hydrophobic SAMs are independent of the surface chemistry, as long as a sufficient number of hydrophobic chains are accessible. Therefore, it is inferred that the nucleation of the nanoweb is very fast.

3.4. Conclusions

We employed hydrophobic surfaces to oligomerize engineered K122-4 pilins from bacterium *P. aeruginosa* into PNTs. Self-assembled monolayers of different alkanethiols on Au(111) were used to initiate pilin oligomerization at various incubation periods of 24-72 h. Different double-component SAMs, containing short hydrophilic and long hydrophobic chains, were employed to limit the hydrophobic sites that are able to initiate pilin oligomerization. Because solution-initiated PNTs are difficult to handle, we aimed to produce surface-initiated PNTs to facilitate their handling. Unlike our expectation, surface-initiated pilin oligomerization formed features which appeared to be different from the solution-initiated PNTs. However, because of possible biosensor and bioseparation applications, the web pattern formed at the hydrophobic SAMs interested us.

Using different single- and double-component alkanethiol SAMs, we learned that only at hydrophobic SAMs, with more than 10-30% accessible hydrophobic component, ΔK122-4 pilins are able to oligomerize into a nanoweb. At the SAMs with less hydrophobicity, the pilins aggregate randomly. The web coverage at the hydrophobic SAMs was ranging from 52 to 71%, while the thickness varied from 3.2 to 6.1 nm.

It was observed that surface step edges and grain boundaries are active sites in adsorbing ΔK122-4 pilin monomers to initiate oligomerization. These areas are highly defective and may expose the hydrophobic alkanethiol chains to the pilins more effectively. It is suggested that ΔK122-4 pilin oligomerization at a hydrophobic surface is triggered by hydrophobic association of the remaining part of the truncated pilins α-helices to form

PNTs. This hydrophobic association is motivated by water exclusion from the hydrophobic parts. Moreover, electrostatic interaction between the oppositely charged areas of the pilins assists oligomerization of the truncated pilins into PNTs, which finally results in the nanoweb formation.

We suggest that at a hydrophobic surface, oligomerization of ΔK122-4 pilins to a web pattern occurs because of the attachment of individual PNTs. While the tubes develop at a hydrophobic surface, adjacent tubes with the same direction stick together to form bundles and grow as thick filaments. When tubes or bundles with different directions join, they continue to grow in a new direction. This process can result in the nanoweb formation.

Another possible reason for the observation of the web pattern is related to the branching PNTs. While ΔK122-4 pilin oligomerization, if pilins bind to the tip, the PNTs grow, but attachment of the monomers at the side of the PNTs results in branching. Continuation of branching along with joining filaments with different directions leads to formation of the web pattern.

Chapter 4: Characterization of the capacitive behaviour of the K122-4 pilins assembly at SAMs

4.1. Introduction

Electrochemical impedance spectroscopy (EIS) characterizes electrochemical systems and solid state interfaces by measuring the impedance over a range of frequencies to illustrate the frequency response of the system.[1-4] In order to measure the dielectric properties of the medium as a function of frequency, EIS is employed to determine the interaction of an external field with the electric dipole moment of the sample.

Electrochemical impedance spectroscopy is a powerful method to investigate solid/liquid interfacial behavior of surface-adsorbed materials. For instance, a wide range of research employed this technique to probe alkanethiol [5-8] and DNA self-assemblies [9-11], as well as protein adsorption [12-16] at solid/liquid interfaces. In this chapter, impedance spectroscopy is employed to study the layer formed by ΔK122-4 pilins at the hydrophobic and hydrophilic SAMs. The aim of these measurements was to investigate whether the web pattern, formed at the hydrophobic surfaces, is a structured layer or it occurs by pilin aggregation.

4.1.1. Electrochemical Impedance Spectroscopy

Electrochemical impedance spectroscopy measures impedance of a cell or electrode at alternating currents (AC) with different frequencies (f). Interpretation of the data using an equivalent circuit gives important information about the interfacial phenomena. Consider

the application of an arbitrary alternative potential E(t) to a series connection of a resistance (R) and a capacitance (C). A purely sinusoidal voltage may be expressed as: [17]

$$E = E_0 \sin(\omega t) \quad (1)$$

in which ω represents angular frequency and t stands for time. Current (i), as the response of the system, is also sinusoidal and can be expressed as:

$$i = i_0 \sin(\omega t + \varphi) \quad (2)$$

Potential and current are assumed to be projections of rotating vectors (phasors) at the abscissa. The length of the rotating vectors of potential and current is E_0 and i_0, respectively. Two vectors of **E** and **i** rotate with the same constant angular frequency, with steady phase angle (φ) between them. Fig. 4.1 represents the vectors at a rotating frame while taking **E** as the reference.[17]

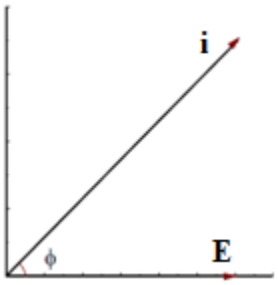

Fig. 4.1. Representation of voltage and current phasors in impedance spectroscopy.

For a pure resistor, as Ohm's law holds, the current equals to $(E_0/R) \sin(\omega t)$, or in phasor notation:

$$\mathbf{i} = \mathbf{E}/R \quad (3)$$

Therefore, as shown in Fig. 4.2, the phase angle between **E** and **i** is zero.[17]

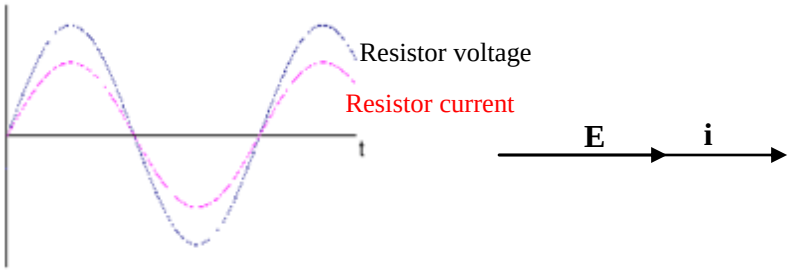

Fig. 4.2. Illustration of an alternative voltage across an Ohmic resistor and the current through it.

For a pure capacitor, taking into account that i = dq/dt and E = q/C (q is electric charge), i can be expressed as: [17]

$$i = \omega C E_0 \cos(\omega t) \quad (4)$$

$$i = \omega C E_0 \sin(\omega t + \pi/2) \quad (5)$$

The phase angle between **E** and **i** is π/2, while **i** is forward (Fig. 4.3). Assuming abscissa as the real and ordinate as the imaginary axis, the result may be expressed using complex notation:

$$\mathbf{i} = j\,\omega C\mathbf{E} \quad (6)$$

where $j = \sqrt{-1}$.

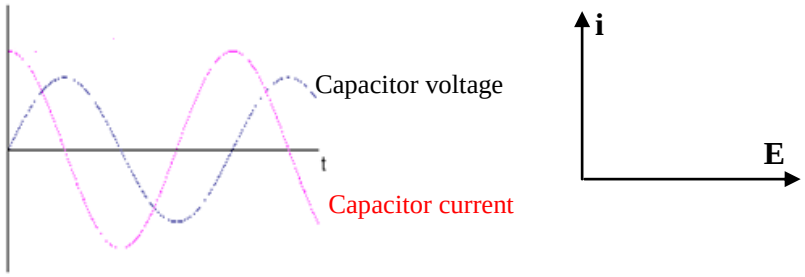

Fig. 4.3. Relationship between an alternative voltage across a capacitor and the current through it.

For an in-series RC system, the potential across the system equals the sum of potentials across the components as: [17]

$$\mathbf{E} = \mathbf{E}_R + \mathbf{E}_C \quad (7)$$

$$\mathbf{E} = \mathbf{i}\,(R_\Omega - j/\omega C) \quad (8)$$

$$\mathbf{Z} = R_\Omega - j/\omega C \quad (9)$$

where **Z** is impedance.

$$\mathbf{E} = \mathbf{i}\,\mathbf{Z} \quad (10)$$

In complex notation, $\mathbf{Z}$[1] may be represented as the sum of imaginary and real part of the impedance:

$$\mathbf{Z} = \mathbf{Z}_{Re} + j\mathbf{Z}_{Im} \quad (11)$$

The phase-angle between **E** and **i** equals: [17]

$$\varphi = \arctan(-j/R_\Omega \omega C) \quad (12)$$

Fig. 4.4a shows the phasor diagram, and Fig. 4.4b represents the Nyquist plot of a series connection of a resistance and a capacitance. In a Nyquist diagram Z_{Im} is plotted against Z_{Re} while the frequency is swept.

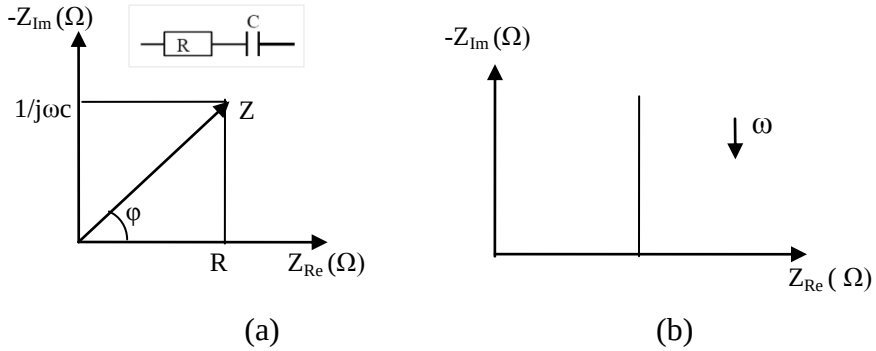

Fig. 4.4. (a) Phasor and (b) Nyquist diagrams of a series of RC.

[1] For the absolute value of the impedance of an in-series RC system the following equation may be used:
$Z^2 = (Z_{Re})^2 + (Z_{Im})^2 = R_\Omega^2 + (j/\omega C)^2$

For an individual resistance, the phase shift is zero, while that of a capacitor is $\pi/2$. However, once both components are present, an in-between phase shift occurs. Fig. 4.5 illustrates the Nyquist plot of an in-parallel RC system. While for an in-series RC model, the total impedance is equal to the sum of the impedances of the components, for a parallel system the overall admittance, reciprocal of the impedance, is up to sum of the admittances of the components.

$$\mathbf{Y} = 1/R_{\Omega} + jC\omega \quad (13)$$

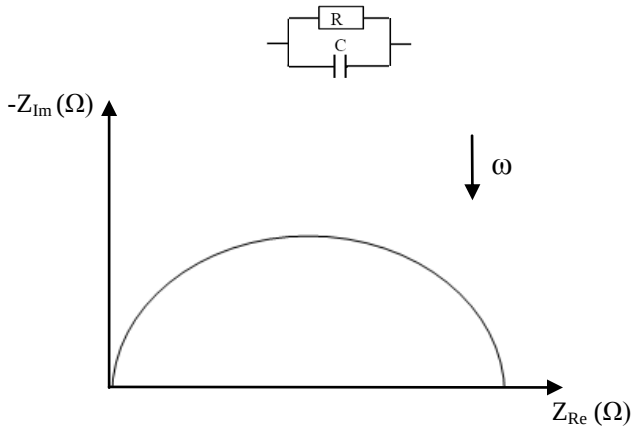

Fig. 4.5. Nyquist diagram of an in-parallel RC model.

4.1.2. Electrochemical Cells

Components of the equivalent circuit of an electrochemical cell represent various phenomena which occur in the cell. Theoretically, an ideally polarized electrode behaves as an ideal capacitor. When the electrons pass through the external circuit and reach the solution-electrode boundary of an ideally polarized electrode, they remain at the electrode surface and increase the charge of the double layer.[18]

In the case of a non-polarized electrode, electrons leave the electrode surface and transfer to a species in the solution to give rise to a faradaic current. Randles equivalent circuit is

a commonly used model for an electrochemical cell containing an electroactive species.[17] This model is shown in Fig. 4.6a. The parallel elements of Z_f and C_{dl} demonstrate the contributions of faradaic process and double layer charging in the total current at the working electrode. Unlike in a real capacitor, the double layer capacitance (C_{dl}) is often a function of potential.[17] One proposed model for a faradaic process is shown in Fig. 4.6b. The model illustrates a resistance R_s in series with a pseudo-capacitor (C_s) to characterize charge transfer and mass transfer processes, respectively. Because the current passes through the solution, a resistance (R_Ω), in series with other components, is used to demonstrate the resistance of the solution.[17]

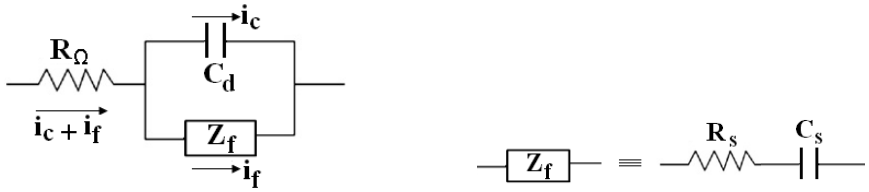

Fig. 4.6. (a) Equivalent circuit of an electrochemical cell with a faradaic process. (b) Two representations of the faradaic process. "Reprinted with permission from (Bard, A. J.; Fulkner, L. R. Electrochemical Methods Fundamental and Applications; 2nd Ed.; 864 pages, ISBN: 978-0-471-04372-0, http://ca.wiley.com/WileyCDA/WileyTitle/productCd-0471043729.html) Copyright (2001) John Wiley and Sons."

The classical model for an ideally polarized electrode is simpler and consists of the solution resistance (R_Ω) in series with the double-layer capacitance (C_{dl}).[4] However, generally speaking, at a solid electrode, the electrical double-layer cannot be modeled as a pure capacitor, but rather as a constant phase element (CPE), with a phase angle different from 90° and independent of the frequency.[19] The CPE is due to the presence of surface inhomogeneity which introduces a distribution of current density along the

electrode surface. In the absence of the faradaic process, the Nyquist diagram acquires an angle smaller than 90° with the vertical line[1] (dashed line in Fig. 4.7).[19] In this situation, the classical representation of the impedance for a polarized system (Eq. 9) is replaced by: [19]

$$Z = R_{\Omega} + (j\omega)^{-n}Q^{-1} \qquad (14)$$

where Q, representing the CPE, is a constant with unit of $\Omega^{-1}s^{n}$. The deviation from the vertical line (capacitive behavior) occurs by (1-n) × 90° clockwise.[19] The dimensionless parameter n has a value between zero and one. When n = 1, the CPE transforms to a pure capacitor.

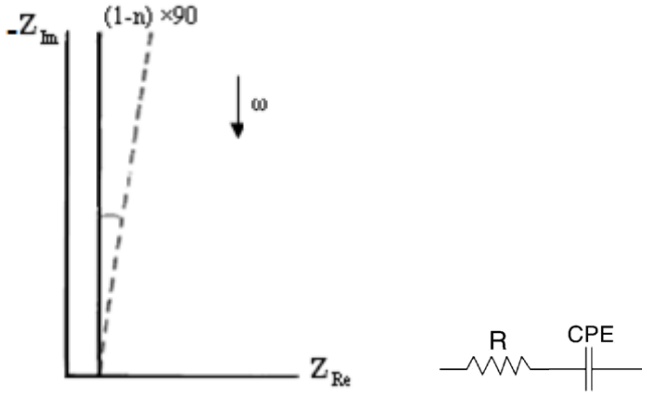

Fig. 4.7. (a) Impedance plot (- - -) for an ideally polarized electrode with surface inhomogeneity. (d) The equivalent circuit for this system.

In the presence of a faradaic process, the curved complex plane plot of the classic model shows a depression. Fig. 4.8 shows the impedance of an electrochemical system with a simple faradaic reaction without diffusion. This system is modeled by a resistance (R_{Ω})

[1] This behavior is also observed in porous electrodes containing intentional inhomogeneity.[20]

related to the solution in series with a parallel combination of a resistance and a CPE which take place due to charge transfer (R_t) and double layer charging, respectively.[19]

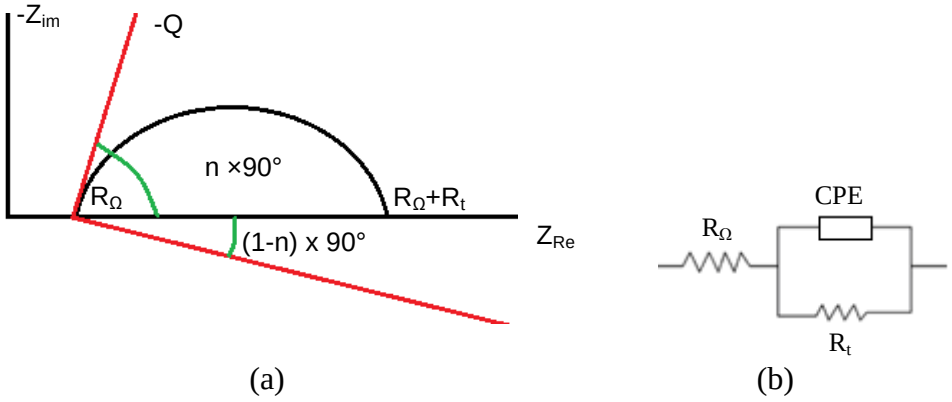

Fig. 4.8. (a) Nyquist diagram of a non-ideally polarized electrode with a simple faradaic reaction without diffusion. The diagram shows a depression due to the surface roughness. (b) The equivalent circuit for the above-mentioned system which comprises a resistance representing the solution resistance (R_1) in series with a parallel combination of a resistance (R_t) and a CPE which are due to charge transfer and double layer charging, respectively.

Due to replacement of the double layer capacitor by a CPE, the vertical axis (shown in pink) makes an angle of (n × 90°) with the x-axis when n is not equal to one. The center of the semicircle is depressed by an angle of (1-n) 90.[20]

G. J. Brug *et al.* formulated the impedance as: [19]

$$Z(\omega) = R_\Omega + R_t / (1 + (j\omega)^n Q R_t) \quad (15)$$

When $\omega \rightarrow \infty$, Z tends to R_Ω (the solution resistance).

4.1.3. Equivalent Circuit for SAMs

The dielectric behavior of alkanethiol SAMs on gold can be investigated via electrochemical impedance spectroscopy.[1-8] In the absence of faradaic current, the SAM is most often modeled as an Ohmic resistance representing the solution resistance

in series with a parallel combination of a CPE to demonstrate the leaky capacitor characteristic of the SAM, and an R_{SAM} to show the resistance of the SAM to charge transfer.[5-7,21]

Pinholes type defects in an alkanethiol self-assembled monolayer make the film somewhat permeable to the electrolyte solution, such that the SAM behaves as a CPE rather than a pure capacitor.[5-7] This behavior results in an increase in the capacitance of the SAM. It is known that only in a very narrow range of potentials, alkanethiol SAMs on gold can be assumed to be impermeable to the aqueous electrolyte.[22] Out of this range, SAMs behave as leaky capacitors. For example, in 50 mM K_2HPO_4 and at pH 7, potentials more cathodic than -350 mV (vs. Ag/AgCl) alter 1-hexadecanethiol SAM from an impermeable to a leaky layer for ion penetration.[22]

To extract the SAM capacitance, we need to quantify the CPE associated to the organic layer. B. Hirschorn *et al.* suggested that CPE is created by two types of time-constant distributions because of the variation of the surface properties, either along the surface or normal to the surface of an electrode.[21] SAMs are mostly modeled by the former. (Fig. 4.9) In the time-constant distribution along the surface, the local admittance, Y_i, includes an Ohmic resistance ($R_{\Omega,i}$) representing local Ohmic resistance in series with a parallel combination of R_i and C_i, corresponding to local surface properties.[21] In this case, the total admittance is equal to the sum of the admittances as:

$$Y = \Sigma_i Y_i = \Sigma_i (R_{\Omega,i} + R_i/(1 + j\omega R_i C_i))^{-1} \quad (16)$$

The impedance vs. CPE can be express as Eq.15.

For this model, the effective capacitance, associated with the CPE, is expressed as: [21]

$$C_{eff} = Q^{1/n}(R_\Omega R_t/(R_\Omega + R_t))^{(1-n)/n} \quad (17)$$

G. J. Brug *et al.* derived the same equation for a non-ideally polarized electrode.[19]

When R_t becomes infinitely large, Eq. 17 can be expressed as:

$$C_{eff} = Q^{1/n} R_\Omega^{(1-n)/n} \quad (18)$$

representing a blocking electrode.[19]

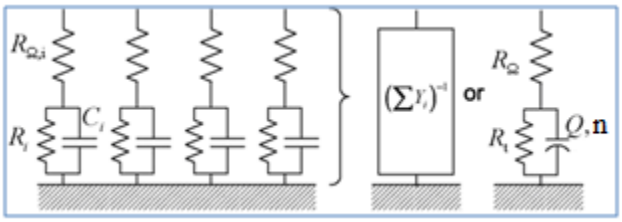

(a)

Fig. 4.9. Schematic representation of a time-constant distribution along an electrode surface, proposed by B. Hirschorn *et al.* "Reprinted from Electrochimica Acta, 55 , Hirschorn, B.; Orazem, M. E.; Tribollet, B.; Vivier, V.; Frateur, I.; Musiani, M., Determination of Effective Capacitance and Film Thickness from Constant-Phase-Element Parameters, 10 pages, Copyright (2010), with permission from Elsevier."

The object of the research presented in this chapter is to investigate the alkanethiol SAMs characteristics, i.e., coverage, defects, as well as the properties of the ΔK122-4 pilin layer at the hydrophobic and hydrophilic SAMs. In the previous chapter, AFM and FT-IR were used to achieve this goal. We showed that truncated K122-4 pilins from bacterium *P. aeruginosa* oligomerize into a web pattern at hydrophobic surfaces, while at hydrophilic ones random aggregation occurs.

In this chapter we analyzed the acquired EIS data for the hydrophobic and hydrophilic SAMs to investigate the properties of the surfaces. We also used EIS to see whether the web pattern formed at hydrophobic SAMs is a structured layer or an aggregation of the pilins. To study ΔK122-4 pilin oligomerization at hydrophobic and hydrophilic films,

alkanethiols with 10 carbons (m = 9) were chosen. The reason is that the alkanethiols with m ≥ 9 have less defects and show almost perfect blocking properties, while SAMs formed by shorter alkanethiols (m < 7) have more defects forming pinholes.[7,23]

4.2. Experimental

Au(111) substrates and alkanethiol SAMs on gold were prepared according to the method explained in section 3.2.3. To prepare the SAMs, 2 mM alkanethiol solutions were employed. To form the pilin layer, the SAMs were immersed in ΔK122-4 pilin solution as described in section 3.2.4.

4.2.1. Electrochemical Impedance Spectroscopy

The electrochemical impedance spectroscopy and cyclic voltammetry measurements were carried out using Voltalab PGZ 402 (Radiometer Copenhagen). A capped PTFE cell with a hole at the bottom (0.35 cm in diameter) was used to expose the sample which acted as the working electrode. A platinum mesh and a saturated calomel electrode (SCE) were used as counter and reference electrodes, respectively. A phosphate buffer with 10 mM concentration and 154 mM ionic strength at pH 7 was used as the electrolyte. The electrolyte was bubbled with argon gas for 30 min before each experiment. The experiments were performed under a blanket of argon gas without disturbing the solution. A potentiostat set the potential difference between the working and reference electrodes to the desired value by adjusting the voltage across the working electrode-counter electrode pair.[24] The current did not flow through the reference electrode to prevent

polarization. Fig. 4.10 shows a simplified diagram of the electrochemical setup using a potentiostat.

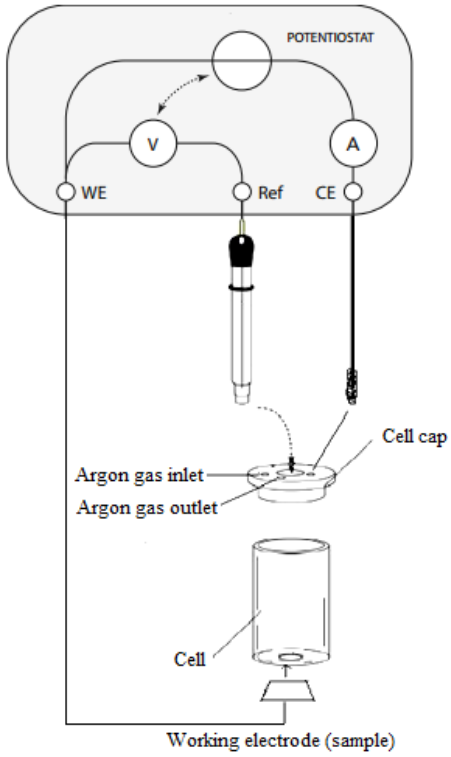

Fig. 4.10. The designed cell and simplified setup used for the electrochemical experiments of this research. The dashed arrow indicates the link between the voltage shown by the voltmeter (controlled voltage between the working and the reference electrodes) and the voltage between the working and the counter electrodes delivered by the power supply.

EIS was performed at an ac amplitude of 10 mV and a potential ranging from -150 to +150 mV_{SCE} to prevent any charge transfer activity. For the Au(111) substrates, the experiments were carried out using the frequency of 100 kHz-100 mHz. The frequency range of 100 kHz- 1 Hz was used for the Au/SAM and Au/SAM/pilin samples. Using EIS Spectrum Analyzer software, the obtained data was fitted to different equivalent circuits.

4.3. Results and Discussion

This section will present electrochemical impedance spectroscopy of (a) Au(111), (b) Au(111)/SAM and (c) Au(111)/SAM/ΔK122-4 pilin substrates. The EIS was employed to characterize the SAMs and the pilin layer formed at hydrophobic and hydrophilic SAMs.

4.3.1. Bare Au(111)

As a control, we performed EIS of Au(111). In order to investigate the capacitance of the double layer at the Au(111)/electrolyte interface, we tried to carry out the experiment employing a DC voltage which prevents charge transfer activity and hence simplifies the equivalent circuit. Fig. 4.11 shows cyclic voltammetry of Au(111), performed at potentials between -200 and +200 mV. This voltammogram reveals some capacitive current as a result of potential change, which charges/discharges the electrical double layer capacitance. The above-mentioned figure shows that this range of potential does not result in any chemical reaction. In the EIS experiments, a +100 mV_{SCE} potential was used.

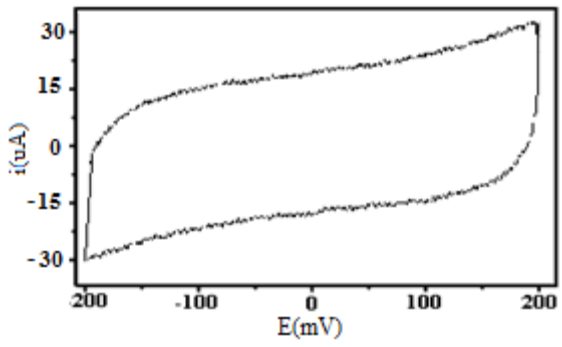

Fig. 4.11. Cyclic voltammogram of Au(111) on glass (0.38 cm^2) in 10 mM buffer phosphate with pH of 7 and ionic strength of 154 mM. Scan rate was 50 mVs^{-1} and an SCE was used as the reference electrode.

Fig. 4.12a-c show diagrams of Z_{Im} versus Z_{Re}, as well as the |Z| and phase shift against logf for impedance spectroscopy of Au(111). The red dots display experimental data. The Nyquist diagram, shown in Fig. 4.12a, illustrates a huge semi-circle representing slow charge transfer activity. This diagram reveals a deviation from an ideally polarized electrode.

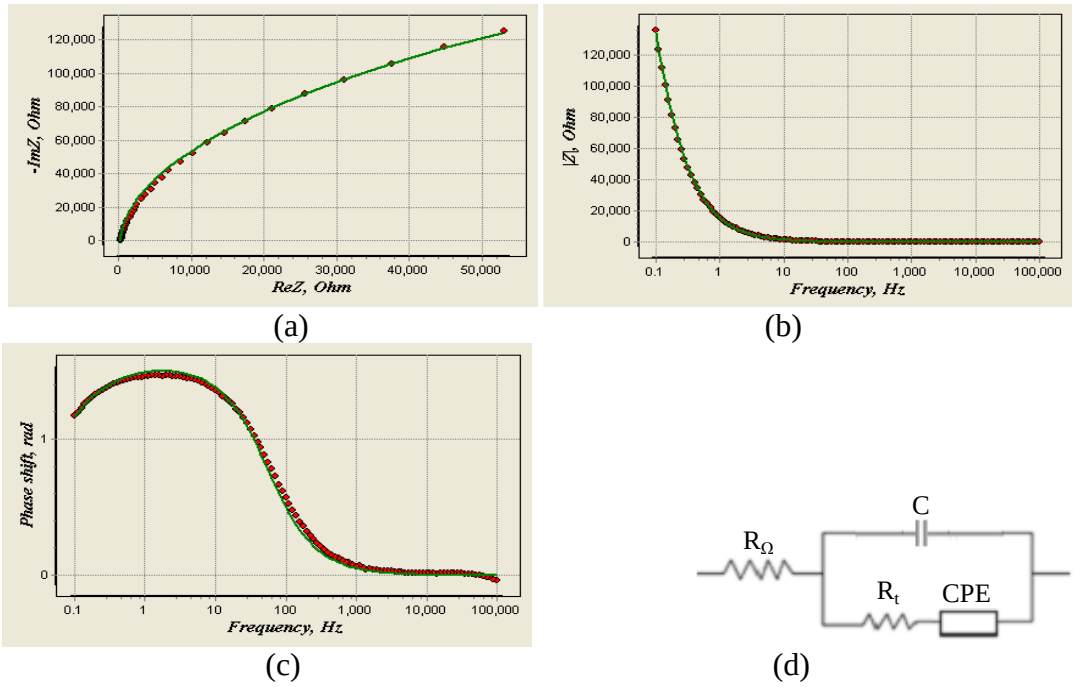

Fig. 4.12. (a) Nyquist, (b) |Z| and (c) phase shift vs. logf of electrochemical impedance spectroscopy of Au(111) on glass at +100 mV_{SCE} potential in 10 mM buffer phosphate with pH of 7 and ionic strength of 154 mM. The red dots are experimental data and the green lines show the fitted impedance data in the proposed equivalent circuit of d.

The models presented in Fig. 4.7b and 4.8b do not fit the above-mentioned experimental EIS data. These models represent ideally and non-ideally polarized electrodes with surface inhomogeneity in the absence of diffusion. Several other models were also investigated to fit the EIS data and to show the phenomena occurred at the surface. It was found that the best equivalent circuit to fit the data is Randles model comprising a

resistance in series with a parallel combination of a capacitor and an element which consists of a resistance in series with a CPE.

This model is shown in Fig. 4.12d. R_Ω demonstrates the solution resistance, and C represents the double layer capacitance at the gold surface. Components representing a faradaic process, R_t and CPE, illustrate charge and mass transfer activities. The red dots in Fig. 4.12a-c display experimental data, whereas green lines illustrate fitted impedance data in the proposed equivalent circuit. The diagrams reveal the model fitted the experimental data.

We also performed the experiment at different potentials. The superimposition of the Nyquist diagrams is shown in Fig. 4.13a. At -150 and 0 mV_{SCE} potentials, the Nyquist diagram shows a huge semicircle representing slow charge transfer activity, while at 50, 100 and 150 mV_{SCE}, a smaller semicircle is followed by a line which makes an angle smaller than 90° with the vertical line. The latter section demonstrates that the process is controlled by the diffusion process in the related frequency range.

The capacitance of the double layer at different potentials was identified by fitting the impedance data in the equivalent circuit shown in Fig. 4.12d. For example, the double layer capacitance at potentials of 150 and 100 mV was found to be 27 ± 14 and 21 ± 8 $\mu F/cm^2$, respectively. These values are in agreement with the literature [25,26] revealing 20-50 $\mu F/cm^2$ for the double layer capacitance of a bare gold electrode. This variation is due to the applied potential and the electrolyte used.

The double layer capacitance at a metal surface depends on the charge of the electrode which is affected by the applied potential. [27] Therefore, the capacitance is expected to

show a minimum corresponding to the pzc. The double layer capacitance at the Au(111) surface versus the applied potential is shown in Fig. 4.13b. A large standard deviation, which is common for the bare gold, was observed. The diagram shown in Fig. 4.13b does not reflect a minimum related to the pzc. These observations can be explained by the face changes occurred on the gold surface. It is known that the pzc is highly dependent on the metal crystalline face.[27] Annealing of the gold substrates produced a textured surface which can be gradually altered as the experiment proceeded, i.e., as the potential is scanned in the gold oxidation region.

Prior to each annealing, the substrate was immersed in 96% sulfuric acid for 5 min, and then it was rinsed. Although this treatment has been shown to be very efficient, the presence of trace contaminants cannot be ruled out. Moreover, trace presence of oxygen is possible. However, gold surface is very active to catalyze oxygen reduction.[28-32] The suggested model for the gold surface (4.12d) contains components reflecting the occurrence of a faradaic process. This model is in conformity with the above-mentioned hypothesis which suggests that it is very difficult to avoid the presence of some electroactive species in the solution. The above-mentioned facts, along with the face change and the possible presence of scratches on the surfaces, which were reused a few times, can explain the large standard deviation of the measured double layer capacitance.

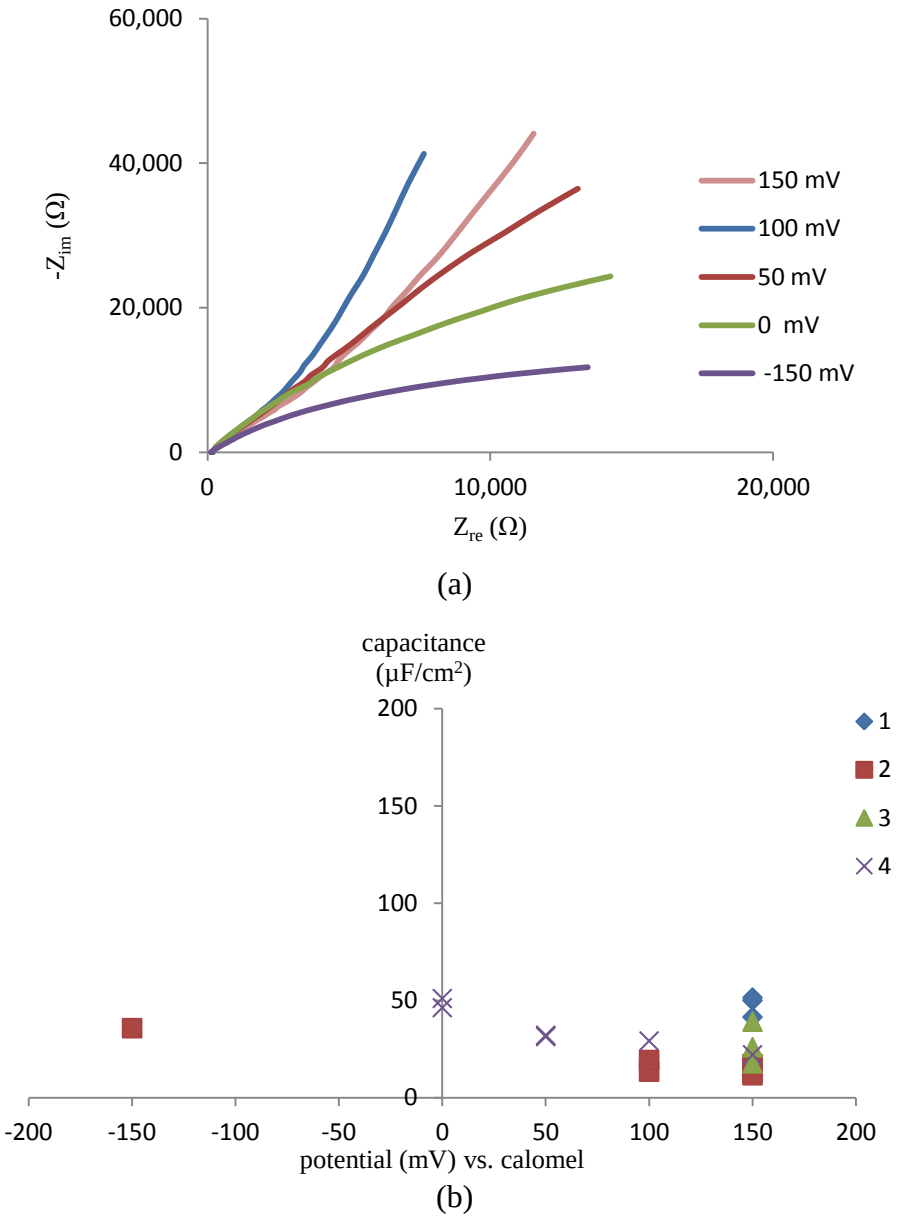

Fig. 4.13. (a) Superimposition of the Nyquist diagrams of electrochemical impedance spectroscopy of Au(111) on glass at different potentials vs. SCE in 10 mM buffer phosphate with pH of 7 and ionic strength of 154 mM. Employed potentials are shown in the legend of the figure. (b) The double layer capacitance of four Au(111) substrates against the applied potentials.

4.3.2. SAMs on Au(111)

EIS was employed to perform another control experiment, as well as to study the SAMs quality. As for hydrophobic and hydrophilic layers, 1-decanethiol and 10-mercaptodecanoic acid SAMs were investigated. The EIS experiments were performed at a DC potential between 0 and 100 mV to prevent charge transfer activity, and to be slightly positive to the pzc (~ -200 mV_{SCE} [5]) of the alkanethiol layers.

It is known that at positive potentials to the electrode pzc, alkanethiol SAMs with $m \geq 9$ are generally assumed to be reasonably impermeable to ions.[5-7,23] This observation is explained by the SAMs dipole moment and the electric field at the interface.[5] At potentials positive to the pzc, the electric field is almost parallel to the layers dipole moment, which is pointed towards the gold surface. This can strengthen the SAMs order. Thus, R_{SAM} is large and does not decrease with a reasonably wide range of increase in potential and temperature.[5]

On the contrary, at potentials negative to the pzc, the electric field direction is approximately antiparallel to the direction of the SAM dipole moment. Hence, the electric field applies a torque[1] on the head group region. This torque can alter the SAM conformation and make it more ion-penetrable and sensitive to potential changes. The conformational change can be bigger at domain boundaries, where chains have more freedom. Even though this distortion is limited to the first few methylenes near the sulfur

[1] $\tau = p\xi\sin\theta$

where p is the dipole moment and ξ is the magnitude of the electric field.

head group, it is still enough to increase the penetration of the ions into the monolayer and decrease the R_{SAM}.

To fit the EIS experimental data of 1-dacanethiol and 10-mercaptodecanoic acid SAMs, we employed the equivalent circuit shown in Fig. 4.14a. SAMs are commonly represented by this model.[5-7,21] To represent the leaky capacitor of the SAMs, a constant phase element is employed (CPE_{SAM}). The resistance of the layer is shown by an Ohmic resistance (R_{SAM}) in parallel to CPE_{SAM}. The solution resistance is taken into account by adding another resistance (R_{Ω}) in series with the parallel combination of the resistance and the CPE of the SAMs. As shown by G. J. Brug *et al*.[19], in this equivalent circuit, the impedance of the CPE can be expressed as Eq. 15. The resistance of the layer is used as R_t in Eq. 15.

In addition to the alkanethiol SAM, the double layer can be modeled as another capacitor, in series with that of the SAM. For in-series capacitors, the total admittance is equal to the sum of the reciprocal capacitances. Therefore, the capacitance of the double layer which could be even ~20 times bigger than that of the SAM can be ignored.

As an example, Fig. 4.14b-d show the diagrams of Z_{Im} versus Z_{Re} , as well as the $|Z|$ and phase shift against logf of the impedance spectroscopy of 1-dacanethiol SAM on gold. In these diagrams, the red dots show experimental data, while the green lines illustrate fitting the above-mentioned equivalent circuit (Fig. 4.14a) in the impedance data. The diagrams illustrate that this model is a good fit for the experimental data. Fig. 4.14e compares the Nyquist diagrams of Au(111) and 1-decanethiol SAM on gold. This diagram illustrates that the SAM formation has increased the impedance considerably.

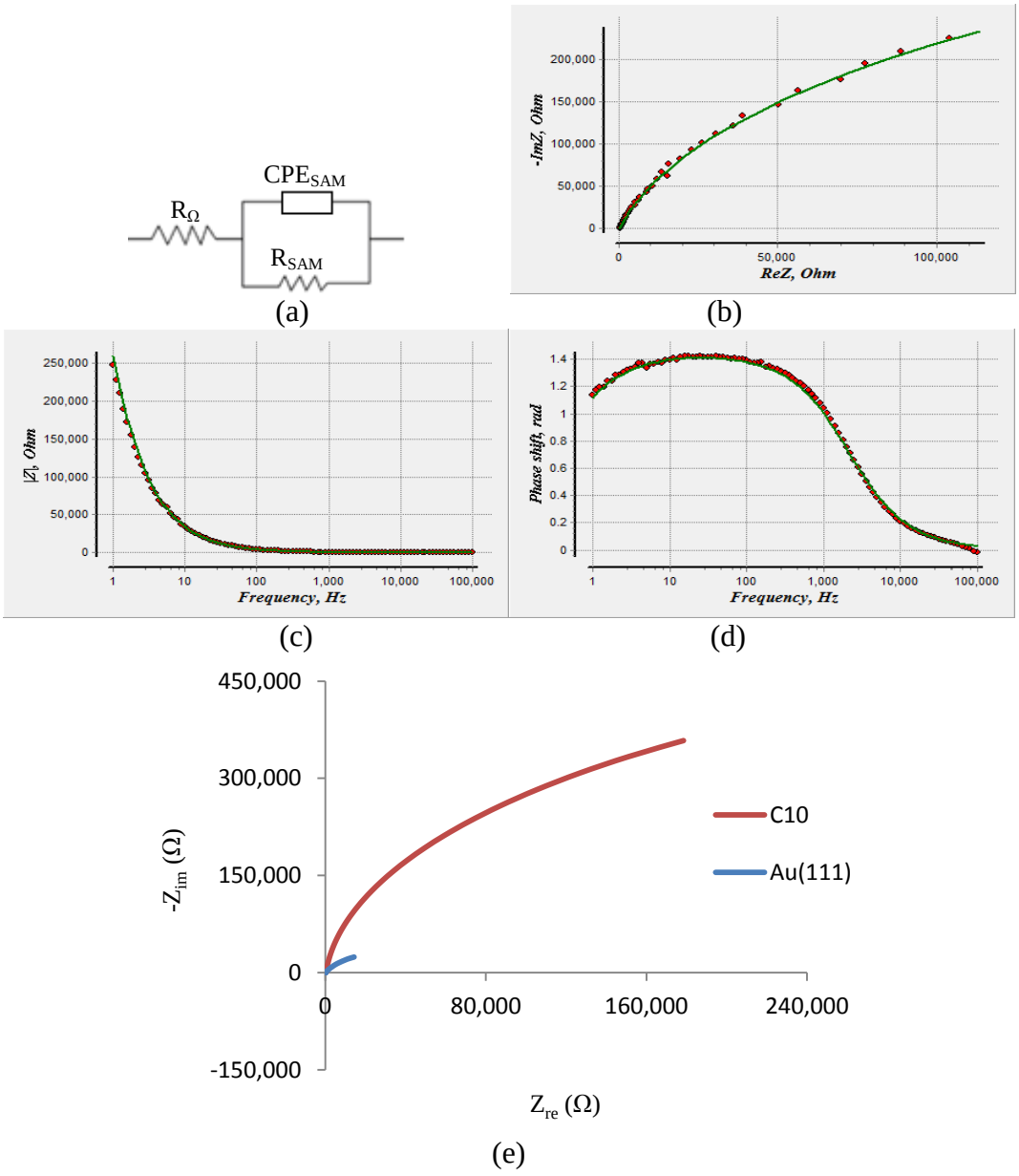

Fig. 4.14. (a) Equivalent circuit used to model Au/SAM/solution, the (b) Nyquist, (c) ıZı and (d) phase shift vs. logf of electrochemical impedance spectroscopy of 1-decanethiol SAM on gold, and (e) superimposition of the Nyquist diagrams of Au(111) and 1-decanethiol SAM on gold. The experiments were carried out at 0 mV_{SCE} potential and in 10 mM buffer phosphate with pH of 7 and ionic strength of 154 mM. In b, c and d, the red dots are experimental data and the green lines show fitted impedance data in the proposed equivalent circuit of a.

Eq. 19 shows the relationship between the capacitance and the film thickness.

$$C = A \varepsilon \varepsilon_{\circ}/d \quad (19)$$

A, ε, $\varepsilon_{\circ}$ and d correspond to the electrode surface area, dielectric constant, space permittivity constant (8.84×10^{-8} μF/cm) and the plates distance, respectively. The film thickness (d) was calculated using the layers capacitance.

Higher defect density makes the SAMs penetrable to the electrolyte; therefore, it results in a bigger capacitance and a lower resistance of the layers. On the other hand, defects decrease the lateral interactions between the alkanethiol chains. Hence, the defects prevent the formation of a solid-like structure with all-trans conformation. This causes a lower SAMs thickness resulting in the increase of the layers capacitance. Consequently, the SAMs capacitance is a factor defining their quality.

4.3.2.1. EIS Data Analysis for 1-Decanethiol SAM

Table 4.1 summarizes the information obtained by fitting the EIS spectra of several 1-decanethiol SAM substrates using the proposed model (Fig. 4.14a) for SAMs. The average values of 262 ± 6 Ω, (2.4 ± 0.1) 10^6 Ω/cm^2, 1.2 ± 0.1 μF/cm^2 and 0.960 ± 0.003 were obtained for R_{Ω}, R_{SAM}/A, Q_{SAM}/A and n_{SAM}, respectively. n_{SAM} is close to the maximum value (1) showing that the SAM has a very small amount of defects. With this in mind, CPE_{SAM} can transform to a capacitor and then Q_{SAM} is equal to the layer capacitance (C_{SAM}). Compared to the value reported by M. D. Porter *et al*. for SAMs with m = 9, 1.4 μF/cm^2 [23], the capacitance of the layers is found to be low, while their resistance is high, which are the characteristics of well-packed SAMs with a low density of defects.

Table 4.1. Parameters of the Au/SAM/electrolyte equivalent circuit of 1-dacanethiol SAM. Electrochemical impedance spectroscopy was carried out using an electrolyte containing 10 mM buffer phosphate with ionic strength of 154 mM at pH 7. To model the surfaces the equivalent circuit of Fig. 4.14a is used.

1-Decanethiol Samples	Potential Vs. SCE	R_{Ω} (Ω)	R_{SAM}(Ω)	R_{SAM}/A (Ω/cm^2)	n_{SAM}	C_{SAM}/A (μF/cm^2)
1	+50 mV	265 ± 7	(1.00 ± 0.02) × 10^6	(2.6 ± 0.1) × 10^6	0.968 ± 0.003	1.0 ± 0.1
2	+50 mV	261 ± 5	(6.0 ± 0.1) × 10^5	(2 ± 1) × 10^6	0.933 ± 0.002	1.5 ± 0.1
3	+50 mV	252 ± 3	(1.00 ± 0.02) × 10^6	(2.6 ± 0. 1) × 10^6	0.936 ± 0.001	1.4 ± 0.1
4	0 mV	266 ± 7	(1.00 ± 0.02) × 10^6	(2.6 ± 0.1) × 10^6	0.997 ± 0.003	1.0 ± 0.1
5	+100 mV	265 ± 7	(1.00 ± 0.02) × 10^6	(2.6 ± 0.1) × 10^6	0.968 ± 0.003	1.0 ± 0.1
Average		262 ± 6	(9.2 ± 0.2) × 10^5	(2.4 ± 0.1) × 10^6	0.960 ± 0.003	1.2 ± 0.1

The SAM is assumed to behave according to Helmholtz model, in which the layer acts as an ideal parallel capacitor. Consequently, Eq. 19 can be employed to calculate the film thickness using the capacitance. Considering 1.2 ± 0.1 μF/cm^2 and 2.1 [33,34] for C_{SAM}/A and ε_{SAM}, Eq. 19 results in the 1-decanethiol SAM thickness of 1.6 ± 0.1 nm. This value is in a good agreement with 1.7 nm [23], which is the thickness of fully extended SAMs with m = 9.

The data for the 1-decanethiol SAM thickness, capacitance and resistance, which is in conformity with the work done by M. D. Porter *et al.*[23] and B. O'Brien *et al.*[5], convinced us that we have produced a good quality 1-decanethiol SAM. Note that high

density of the defects decreases the resistance, increases the capacitance and would lead to a lower SAM effective thickness.

4.3.2.2. EIS Data Analysis for 10-Mercaptodecanoic Acid SAM

The model shown in Fig. 4.14a was also employed for EIS analysis of 10-mercaptodecanoic acid SAMs on gold. Average of several experiments resulted in the following equivalent circuit values: 481 ± 5 Ω, (1.5 ± 0.1) 10^6 Ω/cm^2, 3.2 ± 0.2 μF/cm^2 and 0.878 ± 0.003 for R_Ω, R_{SAM}/A, Q_{SAM}/A and n_{SAM}, respectively. (Table 4.2)

The 10-mercaptodecanoic acid SAM resistance of (1.5 ± 0.1) 10^6 Ω/cm^2 is also high and comparable to the resistance of the 1-decanethiol SAM, i.e., (2.4 ± 0.1) 10^6 Ω. The obtained value for n_{SAM} is not as close as that of 1-decanethiol SAMs to 1; therefore, the layer capacitance is not approximated to be equal to Q_{SAM}. To interpret CPE_{SAM} and to calculate C_{SAM}, Eq. 18 was used. This equation resulted in the C_{SAM}/A of 1.1 ± 0.1 μF/cm^2. The 10-mercaptodecanoic acid SAM shows a capacitance per surface unit close to that of the 1-decanethiol layer (1.2 ± 0.1 μF/cm^2). 1-Decanethiol and 10-mercaptodecanoic acid have the same number of carbons. Therefore, similar capacitances were expected. Using 2.1 for the dielectric constant, the 10-mercaptodecanoic acid film thickness will be 1.6 ± 0.1 nm. This is the same thickness obtained for the 1-decanethiol SAM, also in good conformity with the value of 1.7 nm reported for the thickness of all-extended alkanethiol SAMs with m = 9 [23].

Table 4.2. Components of the suggested equivalent circuit for 1-decanethiol and 10-mercaptodecanoic acid SAMs before and after ΔK122-4 pilin oligomerization/aggregation. Electrochemical impedance spectroscopy was carried out using an electrolyte containing 10 mM buffer phosphate with ionic strength of 154 mM at pH 7. Eq. 18 (G. J. Brug *et al.*[19]) is used to calculate the C of 10-mercaptodecanoic acid SAM on gold.

	1-Dcanethiol SAMs on gold	ΔK122-4 pilin oligomerization at 1-decanethiol SAMs on gold	10-Mercaptodecanoic acid SAMs on gold	ΔK122-4 pilin aggregation at10-mercaptodecanoic acid SAMs on gold
R_Ω (Ω)	262 ± 6	272 ± 4	481 ± 5	161 ± 5
$R_p/A(\Omega/cm^2)$	____	$(2.4 \pm 0.4) \times 10^6$	____	$(7 \pm 1) \times 10^5$
$Q_p/A(\mu F/cm^2)$	____	2.5 ± 0.2	____	3.7 ± 0.4
n_p	____	0.974 ± 0.004	____	0.99 ± 0.01
$R_{SAM}/A(\Omega/cm^2)$	$(2.4 \pm 0.1) \times 10^6$	$(2.4 \pm 0.4) \times 10^6$	$(1.5 \pm 0.1) \times 10^6$	$(1.1 \pm 0.2) \times 10^6$
$Q_{SAM}/A(\mu F/cm^2)$	1.2 ± 0.1	2.6 ± 0.2	3.2 ± 0.2	3.8 ± 0.5
n_{SAM}	0.960 ± 0.003	0.980 ± 0.004	0.878 ± 0.003	0.97 ± 0.01

4.3.3. ΔK122-4 Pilin Oligomerization at SAMs on Gold

In our first approach to find an equivalent circuit for Au/SAM/ΔK122-4 pilin/electrolyte samples, we assumed that the pilin film forms a dielectric layer over that of the SAM. Hence, the EIS data was modeled by adding another parallel combination of a leaky capacitor (CPE_p) and an Ohmic resistance (R_p) in series with the parallel combination of the CPE (CPE_{SAM}) and the resistance (R_{SAM}) representing the SAM. Because the pilin layer and the SAM have different dielectric constants, they cannot be modeled by a unique capacitor.[35]

To take the pilin layer and the SAM permeability into account, a CPE, rather than a pure capacitor, is used to represent each layer. The resistance of the pilin layer and alkanethiol SAM is represented by R_p and R_{SAM}, respectively. As it was the case before, the solution resistance is modeled by an Ohmic resistance (R_Ω) in series with the rest of the circuit mentioned above. The resulting equivalent circuit model is shown in Fig. 4.15a. The capacitance of the double layer, which is considerably higher than that of the SAM and the pilin layer, is ignored.

Superimposition of the fitted Nyquist diagrams of the 1-decanethiol and 10-mercaptodecanoic acid SAMs on gold, with and without the ΔK122-4 pilin layer, is shown in Fig. 4.15b. For each SAM, comparison between the Nyquist diagram of the Au/SAM/electrolyte and Au/SAM/ΔK122-4 pilin layer/electrolyte systems reveals that the presence of the pilin layer increased the size of the semicircle. This occurs because the presence of the pilin layer has increased the charge transfer resistance of the electrode, i.e., decrease the rate of electron transfer at the interface.

Table 4.2 compares the average values (for several samples) of the equivalent circuit components of the methyl and carboxylic acid terminated SAMs before and after ΔK122-4 pilin layer formation. For the R_{SAM}/A and Q_{SAM}/A of the SAM of Au/10-mercaptodecanoic acid SAM/ ΔK122-4 pilin layer/electrolyte model, $(1.1 \pm 0.2)10^6\ \Omega/cm$ and $3.8 \pm 0.5\ \mu F/cm^2$ were obtained. As expected, these values are in good agreement with $(1.5 \pm 0.1)\ 10^6\ \Omega/cm$ and $3.2 \pm 0.2\ \mu F/cm^2$ for the R_{SAM}/A and Q_{SAM}/A of the carboxylic acid SAM with no ΔK122-4 pilin layer. However, because the uniform pilin layer closed the 10-mercaptodecanoic acid SAM pinholes, it improved the SAM via

reducing Q_{SAM}/A and increasing R_{SAM}/A. Moreover, the n_{SAM} has increased from 0.878 ± 0.003 to 0.97 ± 0.01.

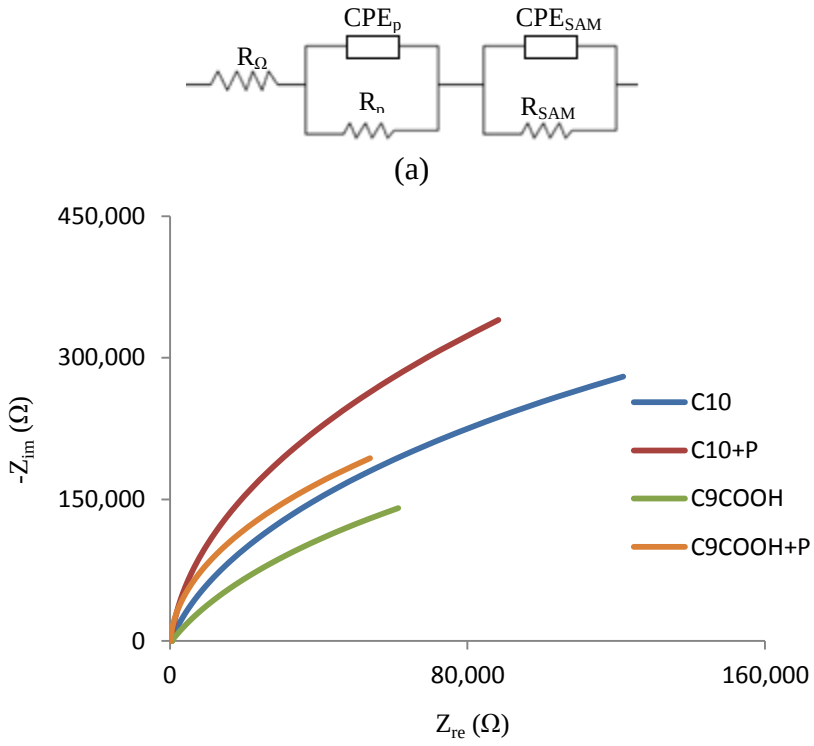

Fig. 4.15. (a) Equivalent circuit used to model Au/SAM/pilin/solution. (b) Superimposition of the fitted Nyquist diagrams of 1-decanethiol (C_{10}) and 10-mercaptodecanoic acid (C_9COOH) SAMs on gold before and after ΔK122-4 pilin (P) oligomerization/aggregation. To model the Au/SAM/solution, the equivalent circuit shown in Fig. 4.14a was employed.

Table 4.2 shows that for the R_{SAM}/A of 1-decanethiol SAM, similar values were obtained for the equivalent circuits of the Au/SAM/ΔK122-4 pilin layer/electrolyte and Au-SAM/electrolyte. On the other hand, pilin oligomerization at the surface increased the SAM capacitance from 1.2 ± 0.1 to 2.6 ± 0.2 μF/cm^2. This can be explained by the effect of the pilin solution on the 1-decanethiol SAM. As mentioned before (Fig. 3.12), the pilin

solution can increase the size of the SAM pinholes. This results in an increase in the layer capacitance. While at hydrophilic SAMs, pilin aggregation forms a uniform layer which can protect the surface from the pilin solution deteriorating effects; at hydrophobic surfaces, ΔK122-4 pilins form a web which does not cover the whole surface.

Capacitance values of 3.7 ± 0.4 μF/cm^2 and 2.5 ± 0.2 μF/cm^2 were obtained for the aggregated pilins at 10-mercaptodecanoic acid SAM and the web pattern formed at 1-decanethiol SAM, respectively. Compared to the web pattern at hydrophobic substrates, the pilin layer at hydrophilic surfaces was observed to be of a higher thickness. Because of the higher thickness, the pilin aggregate was expected to have a smaller capacitance. However, this layer was found to have a higher capacitance. This occurrence could convey the presence of water in the pilin aggregation.

In order to obtain the ε of the ΔK122-4 pilin layer at a hydrophobic surface, we employed the average thickness of ΔK122-4 pilin oligomerization at 1-decanethiol SAM measured by AFM, and the C_p/A acquired via EIS. Image SXM software was employed to measure the average thickness of the pilin layer by deducting the average height of the background (with no pilin) from the average height of the surface with the pilin layer. At the 1-decanethiol SAM, the ΔK122-4 pilin layer thickness (d_p) turned out to have an average of 1.8 ± 0.1 nm. To calculate ε of the pilin layer (ε_p), 8.84 × 10^{-8} μF/cm, 2.5 ± 0.2 μF/cm^2 and 1.8 ± 0.1 nm were used as $\varepsilon_\circ$, C_p/A and d_p in Eq. 19. 5.1 ± 0.7 was obtained for the ε_p.

The dielectric constant of proteins has been reported to have values ranging from 2 to 40.[36-40] In addition to the effects of the protein structure on ε, one source of the

diversity is the method employed to find the dielectric constant.[36] Moreover, larger values are generally obtained because of the presence of the solvent.[36] For the dielectric constant of protein powders, S. Bone *et al.* reported the range of 2-4.[37,38] This is in conformity with 2.5-4, the theoretical estimation for the dielectric constant of a folded protein reported by M. K. Gilson *et al.*[36]

Considering the above-mentioned values and high dielectric constant of water (78.3 [41]), our small ε_p, 5.1 ± 0.7, reveals that the ΔK122-4 pilin-based web pattern does not contain a considerable amount of water, showing that it is a structured layer rather than a simple aggregate that incorporates water molecules. Even crystallographic analysis of K122-4 pilins showed around 33% of water content.[42] Hence, the ε of the pilin aggregation is expected to be significantly larger than 5.1 ± 0.7.

4.4. Conclusions

For the first time, we investigated ΔK122-4 pilin oligomerization/aggregation at alkanethiol self-assembled monolayers on gold using electrochemical impedance spectroscopy. For ΔK122-4 pilin oligomerization at hydrophobic and random aggregation at hydrophilic SAMs, we suggested an equivalent circuit in which a pure resistance was used to model the solution resistance. In series with the Ohmic resistance, two other components were used to represent the pilin layer and the SAM. Each component consists of a CPE in parallel with an Ohmic resistance. The leaky capacitor of each of the pilin layer and the SAM is represented by a CPE (CPE_p and CPE_{SAM}). Via the capacitance of the pilin layer at the 1-decanethiol SAM, dielectric constant of the ΔK122-

4 pilin-based web pattern turned out to be 5.1 ± 0.7. The low value of the ε convinced us to conclude that at the hydrophobic surfaces, ΔK122-4 pilins form a structured layer, rather than a simple aggregate that incorporates water molecules.

Similar components, representing the 10-mercaptodecanoic acid SAM, were obtained for the equivalent circuits of both Au/SAM/ΔK122-4 pilin layer/solution and Au-SAM/solution. On the other hand, the pilin oligomerization at the 1-dacanethiol SAM increased the capacitance of the SAM. This is attributed to the deteriorating effect of the pilin solution on the SAM pinholes. While the pilin solution increases the size of the hydrophobic SAM pinholes, the uniform pilin layer prevents the solution to affect the the10-mercaptodecanoic acid SAM.

As a control, the capacitance of the double layer at Au(111) was studied by electrochemical impedance spectroscopy at different potentials. The capacitance was in good agreement with the literature.[25,26] The quality of 1-decanethiol and 10-mercaptodecanoic acid SAMs were confirmed by the EIS.

Chapter 5: ΔK122-4 Protein Nanotube Metallization

5.1. Introduction

In fields like electronics, the increasing interest in developing nanostructures with specific mechanical and electrical properties makes the topic of metal deposition on nanometer-size objects fascinating. Metalized nanostructures can have potential applications in data storage, imaging and sensing of chemical and biochemical species.[1] Biological templating is a new and promising field for developing nanostructures with electrical conductivity. Numerous biomolecules and biomolecular assemblies, including DNA [2,3], proteins, [4] viral particles [5] antibodies [6] and microtubules [7] have been used as templates for inorganic material deposition. For instance, Y. Eichen *et al.* suggested an assembly of a DNA network to prepare nanometer-scale electronics.[8] They formed a network of DNA which could gain desirable electronic properties if functionalized appropriately.[8] Through another study, K. Ijiro *et al.* synthesized uniform silver nanowires, employing a stretched double-stranded DNA structure.[9] Using electroless metal deposition, they employed cis-platin to catalyze silver metal deposition at DNA molecules.[9]

Because galvanic methods cannot be used to deposit metal on insulators, for a long time electroless metal deposition has been used to metalize the electrically nonconductive substrates such as plastics and ceramics.[10] Through this method, a metal is deposited on a nonconductive surface by using a reducing agent in the absence of an external current.[7,11-14] Electroless metal deposition is an autocatalytic process which occurs

only on a properly activated surface, and it does not happen in the bulk of the solution.[7,12-14]

The following reaction can be used to represent the ELD:

$$M^{n+}_{solution} + Red_{solution} \xrightarrow{\text{activated surface}} M_{lattice} + Ox_{solution} \quad (1)$$

This reaction occurs as long as the reduction potential of the Ox species is more negative than that of M^{n+}. Pourbaix diagrams[1] are useful to determine the conditions for the metal deposition at equilibrium. For example, the Pourbaix diagram for a copper-water system shows that Cu^{2+} is the most thermodynamically stable species of copper in an acidic solution and at potentials greater than +0.337 V versus saturated hydrogen electrode (SHE).[15] Therefore, in order to deposit copper, a potential lower than the above-mentioned value is required.

In order to prevent homogenous metal ion reduction in the solution, it is essential to avoid any large difference between the redox potential of the reducing agent and M^{n+}.[12,16] Ligands are able to decrease this difference through the formation of coordination complexes, which lower the metal redox potential.

Here, we present our attempts at metalizing ΔK122-4 pilin-based protein nanotubes using electroless copper deposition to fabricate conductive nanowires. The electrical conductivity of copper is high, and its electroless deposition is well studied.[12,14,16-19] We employed the method described by S. Balci *et al*. for the fabrication of copper nanowires within the central channel of tobacco mosaic virus particles [12].

[1] A Pourbaix diagram is an electrode potential versus pH diagram which shows possible stable phases of an aqueous electrochemical system at equilibrium.

We employed transmission electron microscope to characterize self-assembled ΔK122-4 PNTs before and after copper deposition. The goal was to develop a suitable method to metalize PNTs and to characterize the metallization process. This study represents the first attempt at metalizing ΔK122-4 PNTs.

5.2. Experimental and Methodology

5.2.1. Materials and Reagents

$CuSO_4 \cdot 5H_2O$ (99.999%), Na_2H_2EDTA (ethylenediaminetetraacetic acid disodium salt, ≥ 98.5%) and TEA (triethanolamine, ≥ 99.0%) were purchased from Sigma, and DMAB (dimethylamine borane, 97%) and Na_2PdCl_4 (99.95%) were from Alfa Aesar. NaCl (99.9%), MPD (2-methyl-1,3-propanediol, 99%) and Tris (99.9%) were from EM Science, Aldrich and BioBasic, respectively. Ultrapure water (Millipore, 18MΩcm, 1μg/l total oxidizable carbon (TOC)) was used to prepare the solutions.

5.2.2. ΔK122-4 Pilin-Based Protein Nanotube

ΔK122-4 PNTs were prepared in Professor G.F. Audette's lab, Chemistry, York University. In order to cultivate ΔK122-4 protein nanotubes, 100 μl of 1 mg/mL ΔK122-4 pilin solution and 66.6 μl MPD were added to 900 μl 10 mM Tris with the final pH being 7.4. The solution was shaken for 3-8 days at room temperature.

5.2.3. Copper Deposition

Initially, ΔK122-4 PNTs were rinsed with deionized water twice. Two rinsing methods were applied. Through the first method, the PNT suspension was centrifuged in a 30 kDa

Amico concentrator for 15 min at 14000 rpm and 4ºC. After adding deionized water, the sample was centrifuged for another 15 min at 14000 rpm and 4ºC. Each time after centrifugation, the supernatant was removed. Through the second method, instead of an Amico concentrator, an Eppendorf vial was used.

The rinsed ΔK122-4 PNTs were sensitized with aqueous Pd(II). 500 µl of PNT suspension in water was added to the same amount of freshly prepared aqueous solution of 1.36 mM Na_2PdCl_4 and 1M NaCl at pH 5. After 10 min, the Pd(II)-sensitized ΔK122-4 PNTs were rinsed applying either of the above-mentioned methods.

Then, in order to metalize the PNTs with copper, the Pd(II)-sensitized ΔK122-4 PNT suspension was mixed with an equal volume of a copper electroless deposition solution for 30 min in room temperature. This solution contains 0.032M $CuSO_4.5H_2O$, 0.04M Na_2H_2EDTA, 0.05M TEA and 0.067M DMAB in water at pH ~7.5. The samples were kept in the fridge at 4ºC for 2-7 days before imaging.

5.2.4. TEM Sample Preparation

In order to characterize ΔK122-4 PNTs and the subsequent copper-deposited PNTs by TEM, 10 µl of ΔK122-4 PNT suspension was deposited on copper grids (200 mesh, Gilder) for 10-20 min. Then, using a filter paper touching the side of the grid, the extra suspension was dried. To image ΔK122-4 PNTs (with no copper deposition), they were stained by deposition of 10 µl of 4% uranyl acetate on the grid. After ~10 min, the liquid was dried off, using a piece of filter paper.

5.2.5. Transmission Electron Microscope

TEM imaging was performed using a Philips EM201 microscope operating at 80 kV. Here, we would like to thank Karen Rethoret, at York University, Imaging Facility, for her contribution to the TEM measurements.

The principles of transmission electron microscopes are the same as light microscopes, except that in electron microscopes, electrons, rather than light are used. The maximum resolution of a light microscope is limited by the light wave length.[20] Since the wavelength[1] of accelerated electrons is much smaller than that of light, electron microscopes can give a resolution (of the order of a few angstroms) a thousand times better than a light microscope.[21]

Fig. 5.1 shows a schematic demonstration of a transmission electron microscope. In TEMs, electrons are produced either by thermionic emission of a filament, usually tungsten, or by field electron emission. The electrons are produced at the top of the microscope and travel down in a column in vacuum. They are accelerated by an electric potential and are focused by electromagnetic lenses[2]. Then, the electron beam passes through the sample to be probed. Because the condenser samples scatter more electrons, the contrast of the image is the result of the specimen density and composition.

---

[1] The wave length of accelerated electrons can be calculated as: [21]

$\lambda e \approx h/ (2m_0E(1+ E/(2m_0c^2)))^{1/2}$

where, h is Planck's constant, m_0 is the rest mass of an electron and E is the energy of the accelerated electron.

[2] An electromagnetic lens consists of several electromagnets arranged in a way to manipulate a charged particle beam.

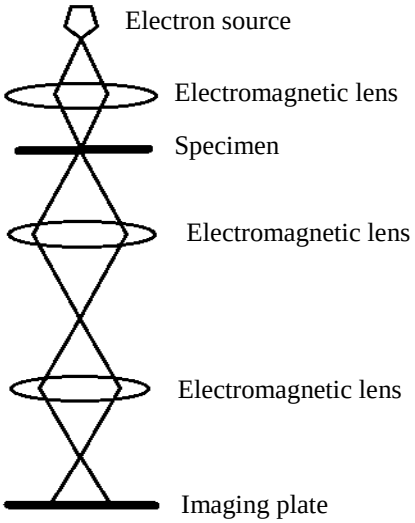

Fig. 5.1. Schematic outline of a TEM.

5.3. Rationale for ELD Bath Composition

Electroless copper deposition, carried out in this research, can be formulated as: [12]

$$4(CH_3)_2NHBH_3 + 12[CuEDTA]^{2-} + 9OH^- \rightarrow$$

$$HB_4O_7^- + 12Cu + 4(CH_3)_2NH_2^+ + 12[HEDTA]^{3-} + 2H_2O \quad (2)$$

$CuSO_4$ was employed as a source of copper, and Na_2H_2EDTA, TEA and DMAB were used as complexing, buffering and reducing agents, respectively. In order to prevent denaturation of the protein structure of ΔK122-4 nanotubes, copper deposition was carried out at pH ~7.5, employing TEA.

5.3.1. Complexing Agent

To avoid random copper deposition at pH ~7.5, the solution was stabilized by disodium EDTA. It is known that to deposit copper at a favorable surface, without spontaneous metal deposition in the solution, it is essential to avoid large difference between the redox potential of the reducing agent and the metal.[12,16] Ligands via complex formation are

able to decrease this difference by reducing the metal redox potential. In the ELD bath, among commonly used complexing agents such as EDTA, malic acid, succinic acid, tartrate, citrate, triethanolamine and ethylenediamine, it is known that $[CuEDTA]^{2-}$ has the lowest reduction potential.[16]

At pH 7, complexation with EDTA reduces the required reduction potential from 0.34 V_{SHE} for Cu^{2+} [15] to below -0.22V_{SHE} for $[CuEDTA]^{2-}$ [22]. Basically, the high copper-EDTA complex formation constant ($10^{18.8}$) prevents the existence of any free Cu^{2+}.[12]

5.3.2. Catalyst for ELD

Even though ELD is thermodynamically possible, the kinetic barrier is so high that, without a catalyst, the reaction does not happen spontaneously.[12] Pd^{2+} and Pt^{2+} are catalysts often employed to activate nonconductive surfaces.[12,23] These two noble metals, which do not corrode easily, provide nucleation sites for the Cu growth. They lower the activation barrier for the crystallization by producing a seed layer to initiate the reaction. Subsequently, the autocatalytic growth takes place.[24]

In this research, ΔK122-4 PNT sensitization is carried out using palladium as Na_2PdCl_4 at pH 5. In the ELD bath, Pd^{2+} is reduced to Pd^0. It is known that only metallic Pd^0, rather than Pd^{2+} or any other species such as hydroxo complexes, acts as an effective ELD catalyst.[11] The chemistry of $PdCl_4^{2-}$ in aqueous solution is affected by the hydrolysis of the Pd^{2+} at pH above ~2.[11,25] The hydrolysis is enhanced by the increase in pH which eventually leads to precipitate Pd(II) as a complex oxobridged polymer.[25] Eq. 3-7 show the mechanism for the precipitate formation suggested by Dressick *et al.*[25] As shown in Eq. 3 and 4, the Cl^- ligands of $PdCl_4^{2-}$ are replaced by H_2O, one after another, at pHs

above ~2 and at low concentrations of Cl^-.[11,25] Then, deprotonation of the hydrolyzed species ($PdCl_3(H_2O)^-$ and $PdCl_2(H_2O)_2$) forms hydroxo complexes (Eq. 5 and 6).[11,25] These complexes precipitate as hydroxo- and/or chloro-bridged oligomers.[11,25] One possible oligomer formation reaction is shown by Eq. 7.[25] Other combinations of hydrolyzed chloropalladium may also form.[25] Consequently, when these complexes are formed, $PdCl_4^{2-}$, which can be reduced to Pd^0 to catalyze copper reduction, is not in excess anymore.

$$PdCl_4^{2-} + H_2O \rightleftarrows Cl^- + PdCl_3(H_2O)^- \quad (3)$$

$$PdCl_3(H_2O)^- + H_2O \rightleftarrows Cl^- + PdCl_2(H_2O)_2 \quad (4)$$

$$PdCl_3(H_2O)^- \rightleftarrows H^+ + PdCl_3(OH)^{2-} \quad (5)$$

$$PdCl_2(H_2O)_2 \rightleftarrows H^+ + PdCl_2(H_2O)(OH)^- \quad (6)$$

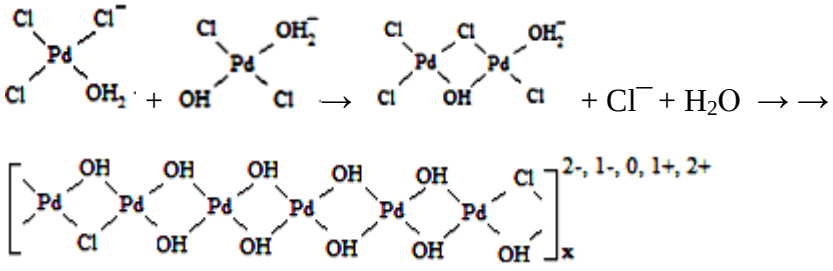

(7)

Even though stable Pd^{2+} ions exist in solution at pHs below ca. 2, [11] it is clear that this pH is not suitable for the ELD on biomaterials. However, formation of palladium complexes is both pH- and Cl^- concentration-dependent. It is well known that the Pd^{2+} stability in aqueous solution can be achieved using chloride ions.[11,25] H. Kind *et al.* have shown that high Cl^- concentrations of the sensitizing bath at pH 5 stabilizes $PdCl_4^{2-}$ and prevents the formation of other species of palladium considerably.[11] This is the condition employed in our study to prepare the Pd^0 layer on the PNTs. Moreover, Cl^-

adsorbs at metals like Au, Pd and Cu to increase the surface mobility by acting as a surfactant.[26-28] This results in a smoother film and better coverage.

Dressick *et al*. have shown that Pd^{2+} is completely reduced to Pd^0 in the presence of DMAB.[25] When the Pd^{2+} is reduced to Pd^0, the palladium complexes are not stable anymore.[11] Indeed, Pd^0 forms stable complexes only with a few ligands (e.g., ligands that contain As, Sb, or P).[11] This can be explained by the ligand field theory, stating that the Pd^0 with the electron configuration of d^{10} is energetically much less favorable than Pd^{2+} with the d^8 configuration.[11] The stabilization energy of Pd(II) is -24.56 Dq_0. For a ligand with $Dq_0 > 0.15$ eV, -24.56 Dq_0 (> 355 kJ/mol) lies in the range of chemical bond energies.[11] Therefore, the Pd^0-ligand bond must be much weaker than the Pd^{2+}-ligand bond, resulting in the diffusion of the Pd^0 species over the surface.[11]

For a better understanding of the Pd island formation, H. Kind *et al*. compared the binding energy of Pd and N before and after reducing the Pd^{2+} species.[11] In order to calculate Pd-Pd bond energy, they estimated the bond energy for a Pd atom in both Pd(111) islands with 16 atoms, as well as the palladium in bulk. They obtained ~3 eV for the microscopic, and 3.9 eV for the macroscopic model.[11] In both cases the Pd-Pd bond energy is almost twice as much as the Pd^{2+}-N binding energy, which is ~1.5 eV.[11]

5.3.3. Reducing Agent

DMAB is one of the most commonly used reducing agents in electroless metal deposition at biological surfaces.[8,12,29,30] The reduction of DMAB is highly pH-dependent. However, the mechanism of this reaction is still unclear. The Pourbaix diagram for a boron-water system reveals that at pH 7-9 and almost all relevant redox potentials (−1.0

and 0.8 V), $HB_4O_7^-$ is the prevailing species.[12] As a result, the DMAB oxidation at pH ~7 is suggested to be according to the following equation: [12]

$$4(CH_3)_2NHBH_3 + 21OH^- \rightarrow HB_4O_7^- + 4(CH_3)_2NH_2^+ + 14H_2O + 24e^- \quad (8)$$

Even though the mechanism is not completely clear, BH_3OH^- is mostly believed to be the active reducing species.[12] Because the BH_3OH^- formation is pH-dependent, it is essential to maintain the pH.[12] In an alkaline medium, the DMAB oxidation results in $B(OH)_4^-$ formation which is generally believed to occur by substitution of the H• of the DMAB by the OH^- in the solvent.[31] This replacement can be formulated as: [12,32]

$$2BH_{4-n}(OH)_n^- + 2OH^- \rightarrow 2BH_{3-n}(OH)_{1+n}^- + H_2 + 2e^- \quad (9)$$

The suggested mechanism for this reaction is exothermic, stabilized by 205 $kJmol^{-1}$ heat which is released because of the recombination of the emitted hydrogen radicals.[31] During DMAB oxidation, the oxidation number of boron does not change, and only hydride ions are oxidized to hydrogen radical.[11,12,32] The above-mentioned mechanism for DMAB oxidation in alkaline medium requires a high pH value [12]. Even though, in our experiments, the pH was not alkaline, the observed gas bubbles make this mechanism reasonable for DMAB oxidation.

It is known that the released heat due to DMAB oxidation decreases exponentially with an increase in the dielectric constant.[31] This occurs because the increase in the dielectric constant stabilizes OH^-.[31] While the dielectric constant of bulk pure water is 78.3, ε is assumed to be 1 (corresponding to the gas phase) at the surface.[31] Accordingly, the reduction of DMAB is expected to occur at the place as close as possible to the surface.[31] This can assist metal deposition at the catalyzed ΔK122-4

PNTs, as well as at the glass container, both of which were observed during our experiments.

5.4. Results and Discussion

The ELD process requires several steps: (a) sensitization of the PNTs with aqueous Pd(II) in the presence of a high concentration of Cl^- ions, (b) rinsing the PNTs and (c) copper deposition by treating the PNTs with the copper ELD solution.

5.4.1. Copper Deposition at ΔK122-4 PNTs

In order to verify ΔK122-4 PNT formation, the solution-initiated PNTs were stained and imaged by TEM. (Fig. 5.2a and 5.2b) 4% uranyl acetate ($UO_2(CH_3COO)_2$) solution was used to stain the PNTs. This compound precipitates at biological surfaces with no selectivity. Along with single PNTs with a diameter of ~6 nm, thicker filaments were also observed, as shown in Fig 5.2a. These filaments appear to be the result of attachment of single PNTs while growing, or during the time they are being prepared for TEM imaging. The boxed area of this figure (Fig. 5.2a) shows a single ΔK122-4 PNT. Fig. 5.2b shows a thick filament whose diameter varies from ~9 nm (at the tip) to ~300 nm (at the thickest part).

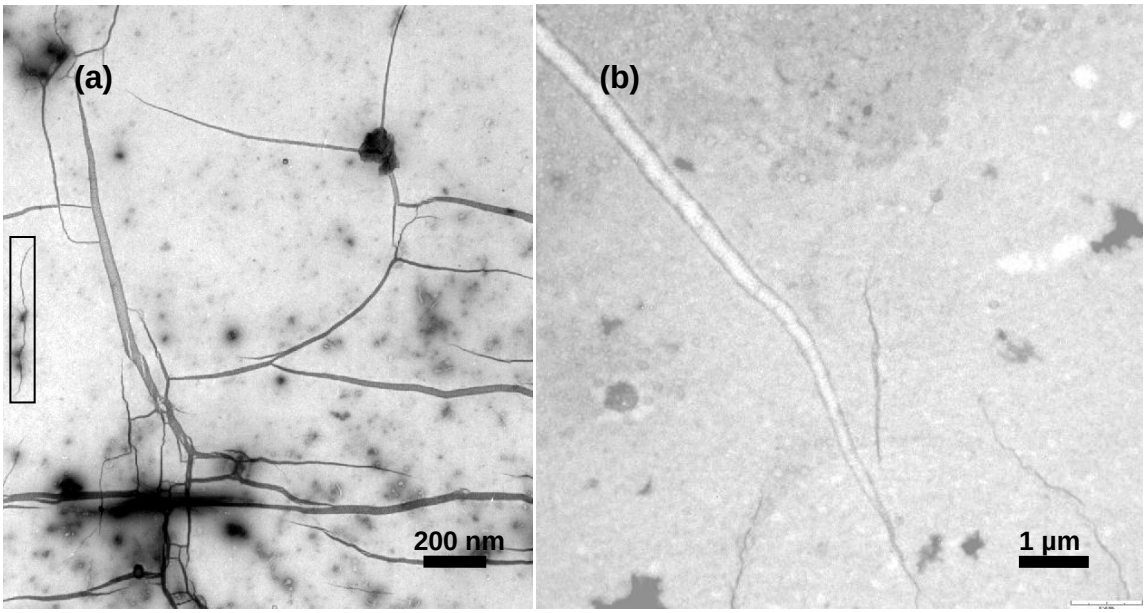

Fig. 5.2. TEM images of ΔK122-4 pilin-based PNTs formed in solution. PNTs are stained with 4% uranyl acetate. (a) Several thin and thick filaments are shown in this image. The boxed area shows a single ΔK122-4 PNT with diameter of 6 ± 1 nm. (b) A thick filament whose diameter varies from 9- 300 nm is shown in this image.

Then, copper deposition at ΔK122-4 PNTs was performed. Fig. 5.3a-d show some metal-deposited PNTs. Note that metalized tubes were not stained; hence, only metal-deposited ΔK122-4 PNTs are visible in the TEM. Fig. 5.3a shows narrow filaments with a diameter of ~6 and ~12 nm representing single and double PNTs. Two metal-deposited bundles of ΔK122-4 PNTs, shown in Fig. 5.3b, look like stained ΔK122-4 PNTs of Fig. 5.2b. The diameter of the tip of the filaments in Fig. 5.3b is ~6 nm which is as small as that of a single PNT, while the thickest part is up to 30 nm in diameter. Fig. 5.3c shows thick bundles of the PNTs which have a diameter of $(1.7 \pm 0.2) \times 10^2$ nm. Fig. 5.3d also shows a thick metal-deposited bundle ($(2.0 \pm 0.1) \times 10^2$ nm), formed by narrower filaments twisted-around each other.

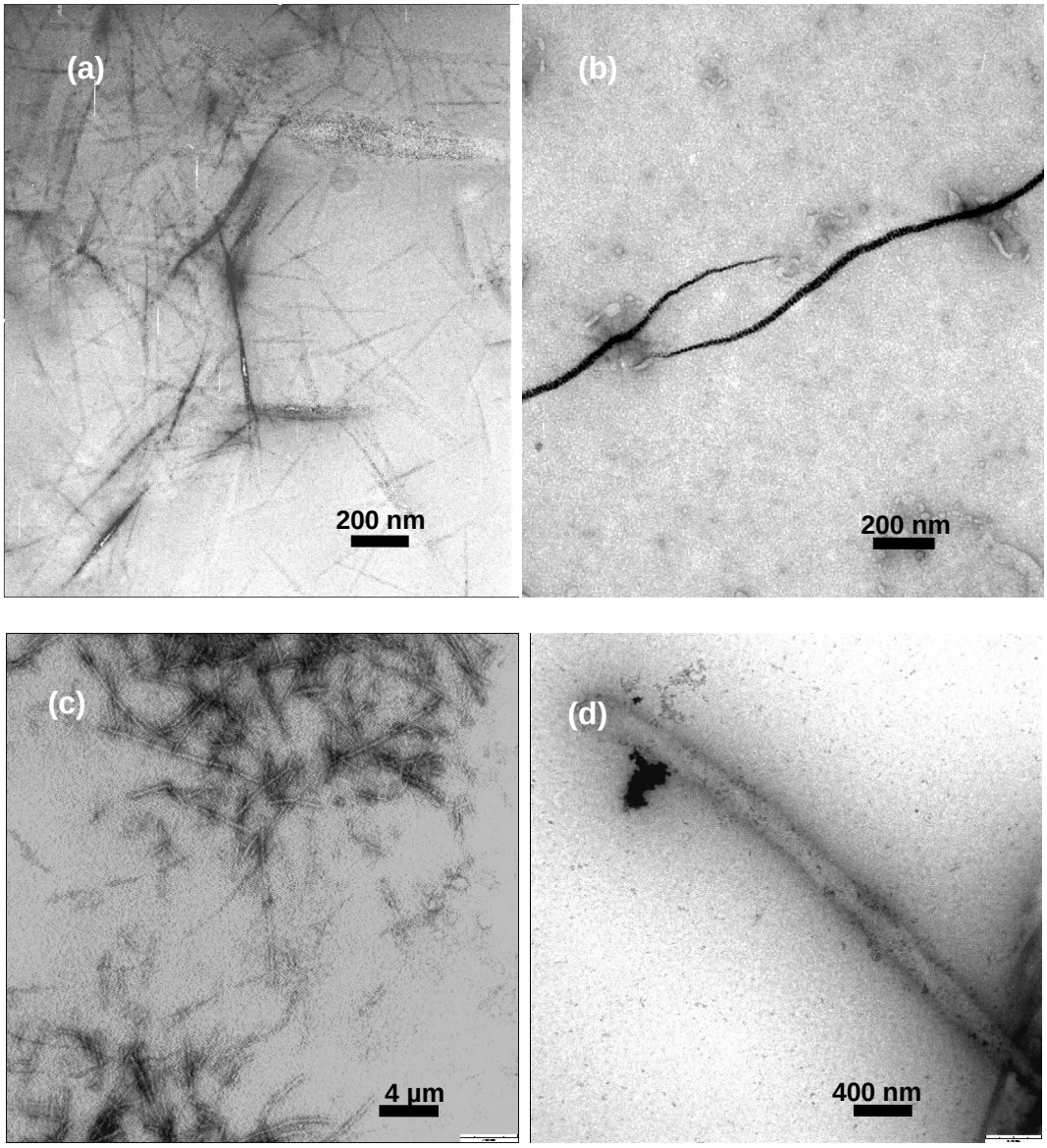

Fig. 5.3. TEM image of metal-deposited ΔK122-4 PNTs. The metallization was carried out by sensitizing the PNTs with Pd(II) followed by electroless copper deposition. (a) Narrow filaments with a diameter of ~6 nm and ~12 nm, revealing single and double PNTs. (b) Two metal-deposited bundles of ΔK122-4 PNTs. Their diameter varies from 6 nm at the tip to 30 nm at the thickest part. (c) Bundles of the PNTs with a diameter of (1.7 ± 0.2) 102 nm. (d) A bundle with a diameter of (2.0 ± 0.1) 102 nm formed by narrower filaments twisted-around each other.

While copper deposition was taking place at ΔK122-4 PNTs, some copper was deposited at the internal wall of the glass flask. Additionally, as shown in Fig. 5.4a, several copper dendrites were also observed. Copper dendrite formation may complicate the result interpretation. Hence, a control experiment was performed to make sure it is possible to differentiate between the metalized PNTs and the dendrites. In the control experiment the palladium solution was added to the copper ELD bath in the absence of ΔK122-4 PNTs. Fig. 5.4b shows copper dendrites formed in this condition. They have an appearance similar to dendrites shown in Fig. 5.4a; thus, it is easy to distinguish them from the metalized PNTs (Fig. 5.3).

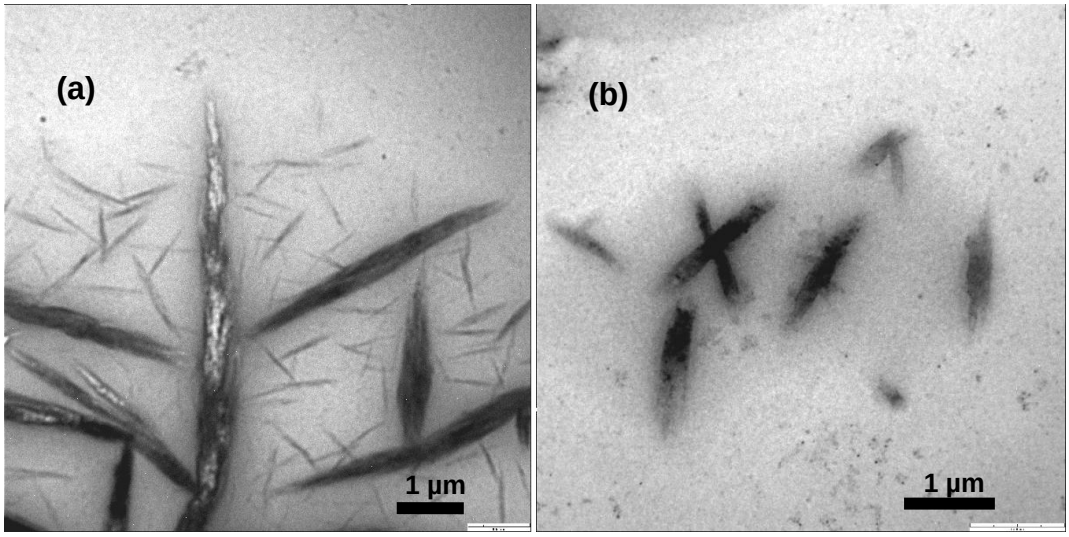

Fig. 5.4. TEM images of (a) copper dendrites formed while copper deposition at ΔK122-4 PNTs and (b) dendrites formed in a control experiment in which the palladium solution was added to the ELD bath in the absence of K122-4 pilin nanotubes.

Although, the ΔK122-4 pilin monomer charges are clustered in five positive and negative regions, the outer surface of PNTs is mostly positively charged.[33] (Fig. 3.6)

Consequently, in the sensitization bath, negatively charged $PdCl_4^{2-}$ ions easily adsorb at the outer surface of the PNTs at pH 5.

Additionally, Pd(II) is able to form a stable complex with the several amino acid residues of PNTs. Specific adsorption of Pd^{2+} ions onto a protein template is determined by the character of Pd^{2+}, accessible amino acid residues and their degree of protonation.[7,34] Pd(II) forms stable complexes with the S-, N- and O-donor groups [34,35] which are present in the side chains of the accessible amino acids. Because Pd^{2+} ion is a soft acid, S- and N-donor ligands are thermodynamically preferred over O-donors (carboxylate or hydroxyl groups).[7,34,36] However, because of the protonation, pH is a very important factor in determining the choice of the donor atoms.[34]

S-donor ligands (soft Lewis bases), cysteine and methionine residues, have a great tendency to bond Pd^{2+}.[34,35,37] The sequence of amino acid residues of ΔK122-4 pilins of bacterium *P. aeruginosa* shows each ΔK122-4 pilin has two accessible cysteine residues (C^{57} and C^{93}) and one moderately conserved methionine (M^{37}) in the PNTs.[33]

N-donor ligands (lysine, arginine, histidine, asparagine and glutamine) also can form strong complexes with Pd(II).[12,29,35,37] Each of the pilins has three asparagines (N^{74}, N^{119}, N^{132}) and one glutamine (Q^{143}) at the PNT surface.[33] Here we would exclude arginine, lysine and histidine. While there is no histidine residue in ΔK122-4 pilins, arginine and lysine are not taken into account because they are protonated at pH 5. The pK_a of the side chains of arginine and lysine are 12.48 and 10.53, respectively.[38]

In comparison to S- and N-donors, O-donor amino acid residues are less favorable to bind Pd(II).[36] However, it is known that carboxylate group is also able to form stable

palladium complexes even faster than the $-NH_2$ group, but thermodynamically the latter is more stable.[34,39] Aspartic acid and glutamic acid contain carboxylic group with pK_a values of 3.65 and 4.25 in their side chains.[38] Consequently, at pH 5, the aspartic acid and glutamic acid side chains are not protonated, able to form complexes with Pd^{2+}. Each ΔK122-4 pilin contains three aspartic acid (D^{54}, D^{72} and D^{103}) and one glutamic acid (E^{68}) residues accessible on the surface of the PNTs, while the other three aspartic acid residues (D^{49}, D^{54}, D^{70}) are moderately conserved.[33]

Only amino acid residues located at the surface of the PNTs are expected to be active. Out of a total 122 amino acids of each ΔK122-4 pilin, 50 are available, 13 are moderately conserved, and the rest are highly conserved. Two cysteines, three aspartic acids, one glutamic acid, three asparagines and one glutamine residues are fully accessible to form complexes with Pd^{2+} at pH 5. Consequently, 20% of fully accessible residues are able to form palladium complexes.

At this stage, it is not possible to confirm if metal deposition also took place inside the ΔK122-4 PNTs channel, but it is our view that this process is unlikely under the conditions used in this study. Because the central channel of ΔK122-4 PNTs is only 2 nm wide and partially occupied by the remaining part of the α-helices, it is difficult for ions to enter the channel. In particular, it is possible that free pilins close the entrance of the PNT channel. Moreover, the residues of the α-helices of ΔK122-4 pilins make the central channel hydrophobic which is not favorable for ions. It is also important to mention that $PdCl_4^{2-}$ with a negative charge is more susceptible to bind and catalyze the positively

charged outer surface of the PNTs. Consequently, it is reasonable to assume that copper deposition is more likely to occur on the external surface of the tubes.

Electroless copper deposition also resulted in some dendrites (Fig. 5.4a), the emergence of which can be explained by the autocatalytic nature of the process. It is known that DMAB oxidation at deposited copper releases more heat than that of the DMAB oxidation at Pd^0.[31] T. Homma *et al.* used Cu_4 and Pd_4 as copper and palladium surface models to calculate the released heat of DMAB oxidation via Eq. 9 at the surface of these metals.[31] They showed that the DMAB oxidation heat at Cu_4 is more than that of Pd_4. Therefore, copper has even more ability than palladium to facilitate the DMAB oxidation reaction. This may result in the dendrite formation. When the first copper atoms are deposited, they form a seed layer to deposit more copper, forming dendrites. This effect could be minimized by carefully adjust the plating electrolyte concentration and deposition time.

5.5. Conclusions

For the first time we carried out electroless copper deposition at the solution-initiated ΔK122-4 PNTs. Transmission electron microscope was employed to detect metal deposition at the ΔK122-4 PNTs. This work shows potential applications for ΔK122-4 PNTs in electronics.

Electroless copper deposition was carried out at Pd(II)-treated ΔK122-4 PNTs at the physiological condition of ca. pH ~7.5. Because of the small size and hydrophobicity of the central channel, we expect copper deposition at the outer surface of the PNTs. $PdCl_4^{2-}$

easily binds to the positively charged outer surface of the PNT. Pd(II) is able to form complexes with at least ~20% of amino acid residues located at the surface of the PNTs. The reduction of Pd^{2+} by DMAB produces Pd^{0} which is able to catalyze copper deposition.

While copper deposition at ΔK122-4 PNTs was taking place, some copper was deposited at the glass container. This observation can be attributed to the tendency of DMAB to be oxidized at the surface. Several copper dendrites were also detected which could be triggered by copper deposition at small aggregation of monomers. The autocatalytic nature of the ELD process [17,18], as well as the tendency of DMAB to be oxidized at the copper surface [31], can explain the fast growth of the dendrites.

Even though copper deposition at nonconductive surfaces via the method employed in this research is known [7,12], further work is required to confirm the presence of copper. To characterize the deposited metal, further experiments are needed.

Chapter 6: Summary

Our research was mostly focused on the subject of adsorption and self-assembly of proteins at modified surfaces. In the first part of this research, AFM was employed to study BSA and insulin adsorption at 1-decene- and methyl 10-undecenoate-modified Si(111) substrates. The results were compared to the MALDI-MS spectra of an earlier work performed by Professor S. Morin's group.[1] In the second part, self-assembled monolayers of different alkanethiols on Au(111) were used to investigate oligomerization of ΔK122-4 pilins from bacterium *P. Aeruginosa*. Then, electrochemical impedance spectroscopy was used to differentiate the ΔK122-4 pilin layer formed at the hydrophobic and hydrophilic surfaces. In the last part, electroless metal deposition at solution-initiated ΔK122-4 PNTs was performed, revealing that ΔK122-4 PNTs have potential applications in electronics.

The contributions to original research in our studies are as follows:

(1) For the first time, we employed AFM to investigate a weak BSA MALDI-MS peak. The previous research of this group [1] has shown that when applying a solution with 1 mg/mL BSA and ~0.01 mg/mL insulin, at methyl- and ester-terminated surfaces, MALDI-MS did not detect BSA, but a big insulin signal was observed.[1] Our AFM images revealed different results. Considerable BSA, but no insulin, was detected at the methyl- and ester-terminated surfaces. The BSA and insulin solutions that we employed had the same concentration level as the experiment with MALDI-MS. We inferred that lack of BSA MALDI-MS signal is due to the stronger interaction between the surface and BSA, rather than the absence of the adsorbed BSA at the substrates.

(2) We used a surface to oligomerize ΔK122-4 pilins for the first time. Different single- and double-component alkanethiol self-assembled monolayers on Au(111) were employed to trigger the oligomerization. We have shown that at alkanethiol SAMs, with more than 10-30% accessible hydrophobic component, ΔK122-4 pilins oligomerize into a nanoweb. At the SAMs with less hydrophobicity, the pilins aggregate randomly. The web coverage at the hydrophobic SAMs was ranging from 52 to 71%, while the thickness varied from 3.2 to 6.1 nm.

AFM imaging has shown that surface step edges and grain boundaries are active sites in adsorbing ΔK122-4 pilin monomers to initiate oligomerization. These areas are highly defective and may expose the hydrophobic alkanethiol chains to the pilins more effectively. We suggested that the surface hydrophobicity starts oligomerization of ΔK122-4 pilins to form protein nanotubes. Formation of PNTs is triggered by hydrophobic association of the remaining part of the truncated pilins α-helices. This hydrophobic association is motivated by water exclusion from the hydrophobic part of the pilins. Moreover, electrostatic interaction between the oppositely charged areas of the monomers assists PNT formation. PNT branching, along with joining of the surface-initiated PNTs, growing in different directions, results in the nanoweb formation.

(3) For the first time, we used electrochemical impedance spectroscopy to study ΔK122-4 pilin oligomerization/aggregation at alkanethiol self-assembled monolayers on gold. We suggested an equivalent circuit in which a pure resistance was used to model the solution resistance. In series with the Ohmic resistance, two other components were used to represent the pilin layer and the SAM. Each component comprises a leaky capacitor

(CPE) in parallel with the charge transfer resistance of the related layer. Using the above-mentioned model, we obtained the dielectric constant of the ΔK122-4 pilin-based web pattern which turned out to be 5.1 ± 0.7. The low value of ε shows that at hydrophobic surfaces, ΔK122-4 pilins form a structured layer, rather than a simple aggregate that incorporates water molecules.

(4) For the first time we carried out electroless copper deposition at the solution-initiated ΔK122-4 PNTs. The surface of the PNTs was activated for copper deposition by Pd deposition. Copper and palladium deposition was detected by transmission electron microscope. We expect that the metal deposition occurred at the outer surface of the PNTs, rather than at the internal channel. While the hydrophobicity and small internal channel of the PNTs make the channel less favorable to be catalyzed and deposit copper, the outer surface is positively charged and has at least 20% accessible amino acids to form complexes with the negatively charged $PdCl_4^{2-}$. Reduction of Pd^{2+} by DMAB produces Pd^0 which is able to catalyze copper deposition. Preliminary transmission electron microscope imaging results demonstrate that metal deposition at the PNTs was achieved. However, in order to have control over the amount of deposited metal, further experiments are required to learn more about the structure and stability of metalized ΔK122-4 PNTs.

References of Chapter 1

1. Endo, K. Chemical Modification of Metallic Implant Surfaces with Biofunctional Proteins (Part 1). Molecular Structure and Biological Activity of a Modified NiTi Alloy Surface. *Dent. Mater. J.* **1995**, 14, 185-198.

2. Scholler, M.; Hauck, A.; Thull, R.; Steinmeyer, R.; Hedrich, R.; Schneider, F. W.; Kiefer, W.; Popp, J. Laser Scanning Microscopy Study on Adsorption of Biologically Relevant Proteins on Implant Materials. *Biopolymers.* **2002**, 67, 344-348.

3. Volcke, C.; Gandhiraman, R. P.; Basabe-Desmonts, L.; Iacono, M.; Gubala, V.; Cecchet, F.; Cafolla, A. A.; Williams, D. E. Protein Pattern Transfer for Biosensor Applications. *Biosens. Bioelectron.* **2010**, 25, 1295-1300.

4. Heeres, J. T.; Kim, S. H.; Leslie, B. J.; Lidstone, E. A.; Cunningham, B. T.; Hergenrother, P. J. Identifying Modulators of Protein−Protein Interactions Using Photonic Crystal Biosensors. *J. Am. Chem. Soc.* **2009**, 131, 18202-18203.

5. Chvapli, M.; Eckmayer, Z. Role of Proteins in Cosmetics. *Int. J. Cosmet. Sci.* **1985**, 7, 41-49.

6. Gorouhi, F.; Maibach, H. I. Role of Topical Peptides in Preventing or Treating Aged Skin. *Int. J. Cosmet. Sci.* **2009**, 31, 327-345.

7. Houdebine, L.M. Production of Pharmaceutical Proteins by Transgenic Animals, *Comp. Immunol. Microb.* **2009**, 32, 107-121.

8. Chen, Q. Expression and Purification of Pharmaceutical Proteins in Plants. *Biol. Eng.* **2008**, 1, 291-321.

9. Ito, M.; Yamauchi, K.; Matsuzawa, K. The Adsorption of Proteins in Fermented Aqueous Food by Silica Gels. *Colloids Surf. A.* **1993**, 74, 107-113.

10. Nakanishi, K.; Sakiyama, T.; Imamura, K. On the Adsorption of Proteins on Solid Surfaces, a Common but Very Complicated Phenomenon. *J. Biosci. Bioeng.* **2001,** 91, 233-244.

11. Knez, M.; Bittner, A. M.; Boes, F.; Wege, C.; Jeske, H.; Maiβ, E.; Kern, K. Biotemplate Synthesis of 3-nm Nickel and Cobalt Nanowires. *Nano lett.* **2003**, 3, 1079-1082.

12. Kobayashi, M.; Seki, M.; Tabata, H.; Watanabe, Y.; Yamashita, I. Fabrication of Aligned Magnetic Nanoparticles Using Tobamoviruses. *Nano lett.* **2010**, 10, 773-776.

13. Lee, S. Y.; Choi, J.; Royston, E.; Janes, D. B.; Culver, J. N.; Harris, M. T. Deposition of Platinum Clusters on Surface-Modified Tobacco Mosaic Virus, *J. Nanosci. Nanotechnol.* **2006**, 6, 974-981.

14. Royston, E.; Lee, S. Y.; Culver, J. N.; Harris, M. T. Characterization of Silica-Coated Tobacco Mosaic Virus. *J. Colloid Interface Sci.* **2006**, 298, 706-712.

15. Iwamoto, G. K.; Van Wagenen, R. A.; Andrade, J. D. Insulin Adsorption: Intrinsic Tyrosine Interfacial Fluorescence, *J. Colloid Interface Sci.* **1982**, 86, 581-585.

16. Ling, J.; Hu, M.; Hagerup, T.; Campbell, R.K. Lispro Insulin: Adsorption and Stability in Selected Intravenous Devices. *The Diabetes Educator.* **1999**, 25, 237-245.

17. Hewson, M. P.; Nawadra, V.; Oliver, J. R.; Odgers, C.; Plummer, J. L.; Simmer, K. Insulin Infusions in the Neonatal Unit: Delivery Variation due to Adsorption. *J. paediatr. child H.* **2000**, 36, 216-220.

18. Fuloria, M.; Friedberg, M. A.; DuRant, R. H.; Aschner, J. L. Effect of Flow Rate and Insulin Priming on the Recovery of Insulin From Microbore Infusion Tubing. *Pediatrics*. **1998**, 102, 1401-1406.

19. Henry, M.; Dupont-Gillain, C.; Bertrand, P. Characterization of Insulin Adsorption in the Presence of Albumin by Time-of-Flight Secondary Ion Mass Spectrometry and X-Ray Photoelectron Spectroscopy. *Langmuir*. **2008**, 24, 458-464.

20. Baier, R.; Meyer, A. E; Natiella, J. R.; Natiella, R. R.; Carter, J. M. Surface Properties Determine Bioadhesive Outcomes: Methods and Results. *J. Biomed. Mater. Res.* **1984,** 18, 337-355.

21. Mollmann, S. H.; Jorgensen, L.; Bukrinsky, J. T.; Elofsson, U.; Norde, W.; Frokjaer, S. Interfacial Adsorption of Insulin: Conformational Changes and Reversibility of Adsorption. *Eur. J. Pharm. Sci.* **2006,** 27, 194-204.

22. Feuerstein, I. A.; Ratner, B. D. Adhesion and Aggregation of Thrombin Prestimulated Human Platelets: Evaluation of a Series of Biomaterials Characterized by ESCA. *Biomaterials.* **1990,** 11, 127-132.

23. Clark, D. P. Molecular biology; Elsevier Academic: Burlington, MA, 2005.

24. Norde, W. Adsorption of Proteins from Solution at the Solid Liquid Interface. *Adv. Colloid Interface Sci.* **1986,** 25, 267-340.

25. Tanford, C. Protein Denaturation. *Adv. Protein Chem.* **1968,** 23, 121-282.

26. Palop, J. J.; Mucke, L. Amyloid-β-Induced Neuronal Dysfunction in Alzheimer's Disease: from Synapses toward Neural Networks. *Nat. Neurosci.* **2010**, 13, 812-818.

27. Kidoaki, S.; Matsuda, T. Mechanistic Aspects of Protein/Material Interactions Probed by Atomic Force Microscopy. *Colloids Surf. B.* **2002**, 23, 153-163.

28. Norde, W.; Lyklema, J. The Adsorption of Human Plasma Albumin and Bovine Pancreas Ribonuclease at Negatively Charged Polystyrene Surfaces: V. Microcalorimetry. *J. Colloid Interface Sci.* **1978**, 66, 295-302.

29. Koutsoukos, P. G.; Norde, W.; Lyklema, J. Protein Adsorption on Hematite (α-Fe_2O_3) Surfaces. *J. Colloid Interface Sci.* **1983**, 95, 385-397.

30. Cohen Stuart, M. A.; Fleer, G. J.; Scheutjens, J. M. H. M. Displacement of Polymers. II. Experiment. Determination of Segmental Adsorption Energy of Poly(vinylpyrrolidone) on Silica. *J. Colloid Interface Sci.* **1984**, 97, 526-535.

31. Grabbe, A.; Horn, R. G. Double-Layer and Hydration Forces Measured between Silica Sheets Subjected to Various Surface Treatments. *J. Colloid Interface Sci.* **1993**, 157, 375-383.

32. Horn, R. G.; Smith, D. T.; Haller, W. Surface Forces and Viscosity of Water Measured between Silica Sheets. *Chem. Phys. Lett.* **1989**, 162, 404-408.

33. Valle-Delgado, J. J.; Molina-Bolivar, J. A.; Galisteo-Gonzalez, F.; Galvez-Ruiz, M. J.; Feiler, A.; Rutland, M. W. Interaction Forces between BSA Layers Adsorbed on Silica Surfaces Measured with an Atomic Force Microscope. *J. Phys. Chem. B.* **2004**, 108, 5365-5371.

34. Butt, H. J. Measuring Electrostatic, van der Waals and Hydration Forces in Electrolyte Solutions with an Atomic Force Microscope. *Biophys. J.* **1991**, 60, 1438-1444.

35. Israelachvili, J. N.; Pashly, R. M. Molecular Layering of Water at Surfaces and Origin of Repulsive Hydration Force, *Nature.* **1983**, 306, 249-250.

36. King, N. P.; Lai, Y. T. Practical Approaches to Designing Novel Protein Assemblies. *Curr. Opin. Struct. Biol.* **2013**, 23, 632-638.

37. Scheibel, T.; Parthasarathy, R.; Sawicki, G.; Lin, X. M.; Jaeger, H.; Lindquist, S. L. Conducting Nanowires Built by Controlled Self-Assembly of Amyloid Fibers and Selective Metal Deposition. *Proc. Natl. Acad. Sci. U. S. A.* **2003**, 100, 4527-4532.

38. Patolsky, F.; Weizmann, Y.; Willner, I. Actin- Based Metallic Nanowires as Bio-Nanotransporters. *Nat. Mater.* **2004**, 3, 692-695.

39. Banerjee, I. A.; Yu, L.; Matsui, H. Cu Nanocrystal Growth on Peptide Nanotubes by Biomineralization: Size Control of Cu Nanocrystals by Tuning Peptide Conformation. *Proc. Natl. Acad. Sci. U. S. A.* **2003**, 100, 14678-14682.

40. Reches, M.; Gazit, E. Casting Metal Nanowires within Discrete Self-Assembled Peptide Nanotubes. *Science.* **2003**, 300, 625-627.

41. Song, Y.; Challa, S. R.; Medforth, C. J.; Qiu, Y.; Watt, R. K.; Pena, D.; Miller, J. E; van Swol, F.; Shelnutt, J. A. Synthesis of Peptide-Nanotube Platinum-Nanoparticle Composites. *Chem. Commun.* **2004**, 9, 1044-1045.

42. Carny, O.; Shalev, D. E.; Gazit, E. Fabrication of Coaxial Metal Nanocables Using a Self-Assembled Peptide Nanotube Scaffold. *Nano Lett.* **2006,** 6, 1594-1597.

43. Uchida, M.; Klem, M. T; Allen, M.; Suci, P.; Flenniken, M.; Gillitzer, E.; Varpness, Z.; Liepold, L. O.; Young, M.; Douglas, T. Biological Containers: Protein Cages as Multifunctional Nanoplatforms. *Adv. Mater.* **2007**, 19, 1025-1042.

44. Audette, G. F.; Hazes, B. Development of Protein Nanotubes from a Multi-Purpose Biological Structure. *J. Nanosci. Nanotechnol.* **2007**, 7, 2222-2229.

45. Audette, G. F.; Van Schaik, E. J.; Hazes, B; Irvin, R. T. DNA-Binding Protein Nanotubes: Learning from Nature's Nanotech Examples. *Nano Lett.* **2004**, 4, 1897-1902.

46. Lombardo, S.; Jasbi, S.; Jeung, S.; Morin, S.; Audette, G. F. Initial Studies of Protein Nanotube Oligomerization from a Gold Surface. *J. Bionanosci.* **2009**, 3, 61-65.

47. Yu, B.; Giltner, C. L.; Van Schaik, E. J.; Bautista, D. L.; Hodges, R.; Audette, G.; Li, D.; Irvin, R. A Novel Biometallic Interface: High Affinity Tip-Associated Binding by Pilin-Derived Protein Nanotubes, *J. Bionanosci.* **2007**, 1, 73-83.

48. Petrov, A.; Audette, G. F. Peptide and Protein-Based Nanotubes for Nanobiotechnology. *Wiley Interdiscip. Rev.Nanomed. Nanobiotechnol.* **2012**, 4, 575-585.

49. Miller, R. A.; Presley, A. D.; Francis, M. B. Self-Assembling Light-Harvesting Systems from Synthetically Modified Tobacco Mosaic Virus Coat Proteins. *J. Am. Chem. Soc.* **2007**, 129, 3104-3109.

50. Huang, Y.; Chiang, C. Y.; Lee, S. K.; Gao, Y.; Hu, E. L.; Yoreo, J. D.; Belcher, A. Programmable Assembly of Nanoarchitectures Using Genetically Engineered Viruses. *Nano Lett.* **2005**, 5, 1429-1434.

51. Mukherjee, S.; Pfeifer, C. M.; Johnson, J. M.; Liu, J.; Zlotnick, A. Redirecting the Coat Protein of a Spherical Virus to Assemble into Tubular Nanostructures. *J. Am. Chem. Soc.* **2006**, 128, 2538-2539.

52. Smart, S. K.; Cassady, A. I.; Lu, G. Q; Martin, D. J. The Biocompatibility of Carbon Nanotubes. *Carbon.* **2006**, 44, 1034-1047.

53. Lin, Y.; Taylor, S.; Li, H.; Fernando, K. A. S.; Qu, L.; Wang, W.; Gu, L.; Zhou, B.; Sun, Y. P. Advances Toward Bioapplications of Carbon Nanotubes. *J. Mater. Chem.* **2004**, 14, 527-541.

54. Scanlon, S.; Aggeli, A. Self-Assembling Peptide Nanotubes. *Nano Today.* **2008**, 3, 22-30.

55. Jia, G.; Wang, H.; Yan, L.; Wang, X.; Pei, R.; Yan, T.; Zhao, Y.; Guo, X. Cytotoxicity of Carbon Nanomaterials: Single-Wall Nanotube, Multi-Wall Nanotube and Fullerene. *Environ. Sci. Technol.* **2005**, 39, 1378-1383.

56. Champion, J. A; Walker, A.; Mitragotri, S. Role of Particle Size in Phagocytosis of Polymeric Microspheres. *Bull. Pharm. Res.* **2008**, 25, 1815-1821.

57. Geng, Y.; Dalhaimer, P.; Cai, S. S.; Tsai, R.; Tewari, M.; Minko, T.; Discher, D. E. Shape Effects of Filaments Versus Spherical Particles in Flow and Drug Delivery. *Nat. Nanotechnol.* **2007**, 2, 249-255.

58. Bartneck, M.; Keul, H. A.; Singh, S.; Czaja, K.; Bornemann, J.; Bockstaller, M.; Moeller, M.; Zwadlo-Klarwasser, G; Groll, J. Rapid Uptake of Gold Nanorods by Primary Human Blood Phagocytes and Immunomodulatory Effects of Surface Chemistry. *ACS nano.* **2010**, 4, 3073-3086.

59. Beningo, K. A.; Wang, Y. L. Fc-Receptor-Mediated Phagocytosis is Regulated by Mechanical Properties of the Target. *J. Cell Sci.* **2002**, 115, 849-856.

60. Kim, S. W.; Kim, T.; Kim, Y. S.; Choi, H. S.; Lim, H. J.; Yang, S. J.; Park, C. R. Surface Modifications for the Effective Dispersion of Carbon Nanotubes in Solvents and Polymers. *Carbon.* **2012**, 50, 3-33.

61. Su, X.; Shuai, Y.; Guo, Z.; Feng, Y. Functionalization of Multi-Walled Carbon Nanotubes with Thermo-Responsive Azide-Terminated Poly(N-isopropylacrylamide) via Click Reactions. *Molecules.* **2013**, 18, 4599-4612.

62. Chen, Y.; Star, A; Vidal, S. Sweet Carbon Nanostructures: Carbohydrate Conjugates with Carbon Nanotubes and Graphene and Their Applications. *Chem. Soc. Rev.* **2013**, 42, 4532-4542.

63. Shim, M.; Shi Kam, N. W. S.; Chen, R. J.; Li, Y.; Dai, H. Functionalization of Carbon Nanotubes for Biocompatibility and Biomolecular Recognition. *Nano Lett.* **2002**, 2, 285-288.

64. Brahmachari, S.; Ghosh, M.; Dutta, S; Das, P. K. Biotinylated Amphiphile-Single Walled Carbon Nanotube Conjugate for Target-Specific Delivery to Cancer Cells. *J. Mater. Chem. B.* **2014**, 2, 1160-1173.

65. Yang, Q. H.; Wang, Q.; Gale, N.; Oton, C. J.; Cui, L.; Nandhakumar, I. S; Zhu, Z.; Tang, Z.; Brown, T.; Loh, W. H. Loosening the DNA Wrapping Around Single-Walled Carbon Nanotubes by Increasing the Strand Length. *Nanotechnology.* **2009**, 20, 195603-195605.

66. Yang, R.; Tang, Z.; Yan, J.; Kang, H.; Kim, Y.; Zhu, Z.; Tan, W. Noncovalent Assembly of Carbon Nanotubes and Single-Stranded DNA: An Effective Sensing Platform for Probing Biomolecular Interactions. *Anal. Chem.* **2008**, 80, 7408-7413.

67. Weizmann, Y.; Chenoweth, D. M.; T. M. DNA-CNT Nanowire Networks for DNA Detection. *J. Am. Chem. Soc.* **2011**, 133, 3238-3241.

68. Tonelli, F. M.; Santos, A. K.; Gomes, K. N.; Lorencon, E.; Guatimosim, S.; Ladeira, L. O.; Resende, R. R. Carbon Nanotube Interaction with Extracellular Matrix Proteins Producing Scaffolds for Tissue Engineering. *Int. J. Nanomed.* **2011**, 7, 4511-4529.

69. Viswanathan, S.; Li, P.; Choi, W.; Filipek, S.; Balasubramaniam, T. A.; Renugopalakrishnan, V. Protein-Carbon Nanotube Sensors: Single Platform Integrated Micro Clinical Lab for Monitoring Blood Analytes. *Methods Enzymol.* **2012,** 509, 165-194.

70. Park, H.; Zhao, J.; Lu, J. P. Effects of Sidewall Functionalization on Conducting Properties of Single Wall Carbon Nanotubes. *Nano Lett.* **2006**, 6, 916-919.

71. Frank, S.; Poncharal, P.; Wang, Z. L.; de Heer, W. A. Carbon Nanotube Quantum Resistors. *Science.* **1998**, 280, 1744-1746.

72. Ebbesen, T. W. ; Lezec, H. J; Hiura, H.; Bennett, J. W.; Ghaemi, H. F.; Thio, T. Electrical Conductivity of Individual Carbon Nanotubes. *Nature.* **1996**, 382, 54-56.

73. Zhang, Z.; Dikin, D. A.; Ruoff, R. S. ;Chandrasekhar, V. Conduction in Carbon Nanotubes through Metastable Resonant States. *Europhys. Lett.* **2004**, 68, 713-716.

74. Aggeli, A.; Bell, M.; Boden, N.; Keen, J. N.; Knowles, P. F.; McLeish, T. C. B.; Pitkeathly, M.; Radford, S. E. Responsive Gels Formed by the Spontaneous Self-Assembly of Peptides into Polymeric β-Sheet Tapes. *Nature.* **1997,** 386, 259-262.

75. Aggeli, A.; Nyrkova, I. A.; Bell, M.; Harding, R.; Carrick, L.; McLeish, T. C. B.; Semenov, A. N.; Boden, N. Hierarchical Self-Assembly of Chiral Rod-Like Molecules as a Model for Peptide β-Sheet Tapes, Ribbons, Fibrils and Fibers. *Proc. Natl. Acad. Sci. U. S. A.* **2001**, 98, 11857-11862.

76. Mahler, A.; Reches, M.; Rechter, M.; Cohen, S.; Gazit, E. Rigid, Self-Assembled Hydrogel Composed of a Modified Aromatic Dipeptide. *Adv. Mater.* **2006**, 18, 1365-1370.

77. Dobson, C.M. Protein Misfolding, Evolution and Disease. *Trends Biochem. Sci.* **1999**, 24, 329-332.

78. Harper, J. D.; Lansbury Jr, P. T. Models of Amyloid Seeding in Alzheimer's Disease and Scrapie: Mechanistic Truths and Physiological Consequences of the Time-Dependent Solubility of Amyloid Proteins. *Annu. Rev. Biochem.* **1997**, 66, 385-407.

79. Sipe, J. D.; Cohen, A. S. Review: History of the Amyloid Fibril. *J. Struct. Biol.* **2000**, 130, 88-98.

80. Gazit, E. Self-Assembled Peptide Nanostructures: the Design of Molecular Building Blocks and Their Technological Utilization. *Chem. Soc. Rev.* **2007**, 36, 1263-1269.

81. Rajagopal, K.; Schneider, J. P. Self-Assembling Peptides and Proteins for Nanotechnological Applications. *Curr. Opin. Struct. Biol.* **2004**, 14, 480-486.

82. Woolfson, D. N.; Ryadnov, M. G. Peptide-Based Fibrous Biomaterials: Some Things Old, New and Borrowed. *Curr. Opin. Chem. Biol.* **2006**, 10, 559-567.

83. Smith, A. M.; Williams, R. J.; Tang, C.; Coppo, P.; Collins, R. F.; Turner, M. L.; Saiani, A.; Ulijn, R. V. Fmoc-Diphenylalanine Self-Assembles to a Hydrogel via a Novel Architecture Based on π–π Interlocked β-Sheets. *Adv. Mater.* **2008**, 20, 37-41.

84. Matsuurua, K. Rational Design of Self-Assembled Proteins and Peptides for Nano- and Micro-Sized Architectures. *RSC Adv.* **2014**, 4, 2942-2953.

85. Mandelkow, E.; Mandelkow, E.-M. Microtubule Structure. *Curr. Opin. Struct. Biol.* **1994**, 4, 171-179.

86. Ballister, E. R.; Lai, A. H.; Zuckermann, R. N.; Cheng, Y.; Mougous, J. D. In Vitro Self-Assembly of Tailorable Nanotubes from a Simple Protein Building Block. *Proc. Natl. Acad. Sci. U. S. A.* **2008**, 105, 3733-3738.

87. Graveland-Bikker, J. F.; Koning, R. I.; Koerten, H. K.; Geels, R. B. J.; Heeren, R. M.A.; de Kruif, C. G. Structural Characterization of α-Lactalbumin Nanotubes. *Soft matter*. **2009**, 5, 2020-2026.

88. Kumara, M. T.; Srividya, N.; Muralidharan, S.; Tripp, B. C. Bioengineered Flagella Protein Nanotubes with Cysteine Loops: Self-Assembly and Manipulation in an Optical Trap. *Nano Lett.* **2006**, 6, 2121-2129.

89. Kumara, M. T.; Tripp, B.; Muralidharan, S. Self-Assembly of Metal Nanoparticles and Nanotubes on Bioengineered Flagella Scaffolds. *Chem. Mater.* **2007,** 19, 2056-2064.

90. Kumara, M. T.; Tripp, B. C.; Muralidharan, S. Layer-by-Layer Assembly of Bioengineered Flagella Protein Nanotubes. *Biomacromolecules*. **2007**, 8, 3718-3722.

91. Mattick, J. S. Type IV Pili and Twitching Motility. *Annu. Rev. Microbiol.* **2002**, 56, 289-314.

92. Wilkinson, J. M. Nanotechnology Applications in Medicine. *Med. device technol*. **2003,** 14, 29-31.

93. Taton, T. A. Bio-Nanotechnology: Two-Way Traffic. *Nat. Mater.* **2003**, 2, 73-74.

94. Braun, E.; Eichen, Y.; Sivan, U.; Ben-Yoseph, G. DNA-Templated Assembly and Electrode Attachment of a Conducting Silver Wire. *Nature.* **1998**, 391, 775-778.

95. Griffin, F.; Ongaro, A.; Fitzmaurice, D. DNA-Templated Assembly of Nanoscale Wires and Protein-Functionalized Nanogap Contacts. *Analyst.* **2004,** 129, 1171-1175.

96. Stanca, S. E.; Eritja, R.; Fitzmaurice, D. DNA-Templated Assembly of Nanoscale Architectures for Next-Generation Electronic Devices. *Faraday Discuss.* **2006**, 131, 155-165.

97. Mao, C.; Flynn, C. E.; Hayhurst, A.; Sweeney, R.; Qi, J.; Georgiou, G.; Iverson, B.; Belcher, A. M. Viral Assembly of Oriented Quantum Dot Nanowires. *Proc. Natl. Acad. Sci. U. S. A.* **2003**, 100, 6946-6951.

98. Mao, C.; Solis, D. J.; Reiss, B. D.; Kottmann, S. T.; Sweeney, R. Y.; Hayhurst, A.; Georgiou, G.; Iverson, B.; Belcher, A. M. Virus-Based Toolkit for the Directed Synthesis of Magnetic and Semiconducting Nanowires. *Science.* **2004**, 303, 213-217.

99. Chan, P.; Phan, T.; Kao, M. C.; Dolan, C.; Tok, J. B. Generating Short Peptidic Ligands for Silver Nanowires from Phage Display Random Libraries. *Bioorg. Med. Chem. Lett.* **2006**, 16, 5261-5264.

100. Nam, K. T.; Kim, D. W.; Yoo, P. J.; Chiang, C. Y.; Meethong, N.; Hammond, P. T.; Chiang, Y. M.; Belcher, A. M. Virus-Enabled Synthesis and Assembly of Nanowires for Lithium Ion Battery Electrodes. *Science.* **2006**, 312, 885-888.

101. Castillo-Leon, J.; Andersen, K. B.; Svendsen, W. E. Self–Assembled Peptide Nanostructures for Biomedical Applications: Advantages and Challenges, In *Biomaterials Science and Engineering*; Pignatello, R., Ed.; InTech: Rijeka, 2011; pp 115-138.

102. Clausen, C. H.; Jensen, J.; Castillo, J.; Dimaki, M.; Svendsen, W. E. Qualitative Mapping of Structurally Different Dipeptide Nanotubes. *Nano Lett.* **2008**, 8, 4066-4069.

103. Clausen, C. H.; Dimaki, M.; Panagos, S. P.; Kasotakis, E.; Mitraki, A.; Svendsen, W. E.; Castillo-Leon, J. Electrostatic Force Microscopy of Self-Assembled Peptide Structures. *Scanning.* **2011**, 33, 201-207.

104. Goldstein, J.; Newbury, D. E.; Joy, D. C.; Lyman, C. E.; Echlin, P.; Lifshin, E.; Sawyer, L.; Michael, J. R. Scanning Electron Microscopy and X-ray Microanalysis; 3rd Ed. Kluwer Academic/Plenum: New York, 2001.

105. Adler-Abramovich, L.; Reches, M.; Sedman, V. L.; Allen, S.; Tendler, S. J. B.; Gazit, E. Thermal and Chemical Stability of Diphenylalanine Peptide Nanotubes: Implications for Nanotechnological Applications. *Langmuir.* **2006**, 22, 1313-1320.

106. Song, H.; Diakowski, P. M.; Hudson, R. H. E.; Kraatz, H. B. Effect of Ferrocene Position on Charge Transfer in ds-DNA Films. *J. Inorg. Organomet. Polym. Mater.* **2012**, 22, 178-182.

107. Wain, A. J.; Zhou, F. Scanning Electrochemical Microscopy Imaging of DNA Microarrays Using Methylene Blue as a Redox-Active Intercalator. *Langmuir.* **2008**, 24, 5155-5160.

108. Grutzke, S.; Abdali, S.; Schuhmann, W.; Gebala, M. Detection of DNA Hybridization Using Electrochemical Impedance Spectroscopy and Surface Enhanced Raman Scattering. *Electrochem. Commun.* **2012**, 19, 59-62.

109. Ge, C.; Tan, Y.; Liao, J.; Zhang, Y.; Zhang, H.; Gu, N. Potential Control of DNA Self-Assembly on Gold Electrode. *Chin. Sci. Bull.* **2002**, 47, 370-375.

110. Cai, Z.; Liu, S.; Asakawa, D. Applications of MALDI-TOF Spectroscopy; Springer: Berlin, 2013.

111. Mengistu, T. Z.; DeSouza, L.; Morin, S. Probing Proteins on Functionalized Silicon Surfaces Using Matrix-Assisted Laser Desorption/Ionization Mass Spectrometry. J. Chromatogr. A. **2006**, 1135, 194-202.

112. Liu, H.; Motoda, H. Computational Methods of Feature Selection; Chapman & Hall/CRC: Boca Raton, (2008).

113. Strother, T.; Hamers, R. J.; Smith, L. M. Covalent Attachment of Oligodeoxyribonucleotides to Amine-Modified Si(001) Surfaces. *Nucleic Acids Res.* **2000**, 28, 3535-3541.

114. Strother, T.; Cai, W.; Zhao, X.; Hamers, R. J.; Smith, L. M. Synthesis and Characterization of DNA-Modified Silicon(111) Surfaces. *J. Am. Chem. Soc.* **2000**, 122, 1205-1209.

115. Wei, F.; Sun, B.; Guo, Y.; Zhao, X. S. Monitoring DNA Hybridization on Alkyl Modified Silicon Surface through Capacitance Measurement. *Bioelectron*. **2003**, 18, 1157-1163.

116. Finnskog, D.; Jaras, K.; Ressine, A.; Malm, J.; Marko-Varga, G.; Lilja, H.; Laurell, T. High-Speed Biomarker Identification Utilizing Porous Silicon Nanovial Arrays and MALDI-TOF Mass Spectrometry. *Electrophoresis.* **2006**, 27, 1093-1103.

117. Xu, S.; Zhou, H.; Pan, C.; Fu, Y.; Zhang, Y.; Li, X.; Ye, M.; Zou, H. Iminodiacetic Acid Derivatized Porous Silicon as a Matrix Support for Sample Pretreatment and

Matrix-Assisted Laser Desorption/Ionization Time-of-Flight Mass Spectrometry Analysis. *Rapid Commun. Mass Spectrom.* **2006**, 20, 1769-1775.

118. Weinberger, S. R.; Boschetti, E.; Santambien, P.; Brenac, V. Surface-Enhanced Laser Desorption–Ionization Retentate Chromatography™ Mass Spectrometry (SELDI–RC–MS): a New Method for Rapid Development of Process Chromatography Conditions. *J Chromatogr B.* **2002**, 782, 307-316.

119. Issaq, H. J.; Veenstra, T. D.; Conrads, T. P.; Felschow, D. The SELDI-TOF MS Approach to Proteomics: Protein Profiling and Biomarker Identification. *Biochem. Biophys. Res. Commun.* **2002**, 292, 587-592.

120. Yu, Q.; Zhang, Y.; Chen, H.; Wu, Z.; Huang, H.; Cheng, C. Protein Adsorption on Poly(N-isopropylacrylamide)-Modified Silicon Surfaces: Effects of Grafted Layer Thickness and Protein Size. *Colloids Surf. B.* **2010**, 76, 468-474.

121. Awsiuk, K.; Bernasik, A.; Kitsara, M.; Budkowski, A.; Rysz, J.; Haberko, J.; Petrou, P.; Beltsios, K.; Raczkowska, J. Protein Coverage on Silicon Surfaces Modified with Amino-Organic Films: a Study by AFM and Angle-Resolved XPS. *Colloids Surf. B.* **2010**, 80, 63-71.

122. Love, J. C.; Estroff, L. A.; Kriebel, J. K.; Nuzzo, R. G.; Whitesides, G. M. Self-Assembled Monolayers of Thiolates on Metals as a Form of Nanotechnology. *Chem. Rev.* **2005**, 105, 1103-1170.

123. Gupta, C.; Shannon, M. A.; Kenis, P. J. A. Electronic Properties of a Monolayer-Electrolyte Interface Obtained from Mechanistic Impedance Analysis. *J. Phys. Chem. C.* **2009**, 113, 9375-9391.

124. Chidsey, C. E. D. Free Energy and Temperature Dependence of Electron Transfer at the Metal-Electrolyte Interface. *Science.* **1991**, 251, 919-922.

125. Finklea, H. O.; Hanshew, D. D. Electron-Transfer Kinetics in Organized Thiol Monolayers with Attached Pentaammine(pyridine)ruthenium Redox Centers. *J. Am. Chem. Soc.* **1992**, 114, 3173-3181.

126. Finklea, H. O.; Ravenscroft, M. S.; Snider, D. A. Electrolyte and Temperature Effects on Long Range Electron Transfer Across Self-Assembled Monolayers. *Langmuir.* **1993**, 9, 223-227.

127. Acevedo, D.; Abruna, H. D. Electron-Transfer Study and Solvent Effects on the Formal Potential of a Redox-Active Self-Assembling Monolayer. *J. Phys. Chem.* **1991**, 95, 9590-9594.

128. Guo, Y.; Zhao, J.; Yin, X.; Gao, X.; Tian, Y. Electrochemistry Investigation on Protein Protection by Alkanethiol Self-Assembled Monolayers against Urea Impact. *J. Phys. Chem. C.* **2008**, 112, 6013-6021.

129. Menz, B.; Knerr, R.; Gopferich, A.; Steinem, C. Impedance and QCM Analysis of the Protein Resistance of Self-Assembled PEGylated Alkanethiol Layers on Gold. *Biomaterials.* **2005**, 26, 4237-4243

130. Ge, C.; Tan, Y.; Liao, J.; Zhang, Y.; Zhang, H.; Gu, N. Potential Control of DNA Self-Assembly on Gold Electrode. *Chin. Sci. Bull.* **2002**, 47, 370-375.

131. Dupont-Gillain, C. C.; Fauroux, C. M. J.; Gardner, D. C. J.; Leggett, G. J. Use of AFM to Probe the Adsorption Strength and Time-Dependent Changes of Albumin on Self-Assembled Monolayers. *J. Biomed. Mater. Res. Part A.* **2003**, 67, 548-558.

132. Ta, T. C.; McDermott, M. T. Mapping Interfacial Chemistry Induced Variations in Protein Adsorption with Scanning Force Microscopy. *Anal. Chem.* **2000**, 72, 2627-2634.

133. van Schaik, E. J.; Giltner, C. L.; Audette, G. F.; Keizer, D. W.; Bautista, D. L.; Slupsky, C. M.; Sykes, B. D.; Irvin, R. T. DNA Binding: a Novel Function of *Pseudomonas Aeruginosa* Type IV Pili. *J. Bacteriol.* **2005**, 187, 1455-1464.

References of Chapter 2

1. Petrie, R. J.; MacDonald, S. M.; Fuller, K. L.; Roscoe S.G.; Tafel Behaviour and Competitive Adsorption of Amino Acids and Peptides with Surface Oxide Formation at the Pt Electrode. *Can. J. Chem*. **2011**, 75, 1585-1596.

2. Brosseau, C.L.; Roscoe, S.G.; Electrochemical Quartz Crystal Nanobalance and Chronocoulometry Studies of Phenylalanine Adsorption on Au. *Electrochim. Acta.* **2006**, 51, 2145-2152.

3. Scholler, M.; Hauck, A.; Thull, R.; Steinmeyer, R.; Hedrich, R.; Schneider, F. W.; Kiefer, W.; Popp, J. Laser Scanning Microscopy Study on Adsorption of Biologically Relevant Proteins on Implant Materials. *Biopolymers.* **2002**, 67, 344-348.

4. Nakanishi, K.; Sakiyama, T.; Imamura, K. On the Adsorption of Proteins on Solid Surfaces, a Common but Very Complicated Phenomenon. *J. Biosci. Bioeng.* **2001,** 91, 233-244.

5. Norde, W. Adsorption of Proteins from Solution at the Solid Liquid Interface. *Adv. Colloid Interface Sci.* **1986,** 25, 267-340.

6. Norde, W.; Lyklema, J. The Adsorption of Human Plasma Albumin and Bovine Pancreas Ribonuclease at Negatively Charged Polystyrene Surfaces: V. Microcalorimetry. *J. Colloid Interface Sci.* **1978**, 66, 295-302.

7. Iwamoto, G. K.; Van Wagenen, R. A.; Andrade, J. D. Insulin Adsorption: Intrinsic Tyrosine Interfacial Fluorescence. *J. Colloid Interface Sci.* **1982**, 86, 581-585.

8. Hewson, M. P.; Nawadra, V.; Oliver, J. R.; Odgers, C.; Plummer, J. L.; Simmer, K. Insulin Infusions in the Neonatal Unit: Delivery Variation Due to Adsorption. *J. paediatr. child H.* **2000**, 36, 216-220.

9. Fuloria, M.; Friedberg, M. A.; DuRant, R. H.; Aschner, J. L. Effect of Flow Rate and Insulin Priming on the Recovery of Insulin From Microbore Infusion Tubing. *Pediatrics.* **1998**, 102, 1401-1406.

10. Rabinow, B. E.; Ding, Y. S.; Qin, C.; McHalsky, M. L.; Schneider, J. H.; Ashline, K. A.; Shelbourn, T. L.; Albrecht, R. M. Biomaterials with Permanent Hydrophilic Surfaces and Low Protein Adsorption Properties. *J. Biomater. Sci. Polym. Ed.* **1994**, 6, 91-109.

11. Xu, S.; Zhou, H.; Pan, C.; Fu, Y.; Zhang, Y.; Li, X.; Ye, M.; Zou, H. Iminodiacetic Acid Derivatized Porous Silicon as a Matrix Support for Sample Pretreatment and Matrix-Assisted Laser Desorption/Ionization Time-of-Flight Mass Spectrometry Analysis. *Rapid Commun. Mass Spectrom.* **2006**, 20, 1769-1775.

12. Finnskog, D.; Jaras, K.; Ressine, A.; Malm, J., Marko-Varga, G.; Lilja, H.; Laurell, T. High-Speed Biomarker Identification Utilizing Porous Silicon Nanovial Arrays and MALDI-TOF Mass Spectrometry. *Electrophoresis.* **2006**, 27, 1093-1103.

13. Mengistu, T. Z.; DeSouza, L.; Morin, S. Probing Proteins on Functionalized Silicon Surfaces Using Matrix-Assisted Laser Desorption/Ionization Mass Spectrometry. J. Chromatogr. A. **2006**, 1135, 194-202.

14. Buriak, J. M. Organometallic Chemistry on Silicon and Germanium Surfaces. *Chem. Rev.* **2002**, 102, 1271-1308.

15. Linford, M. R.; Fenter, P.; Eisenberger, P. M.; Chidsey, C. E. D.; Alkyl Monolayers on Silicon Prepared from 1-Alkenes and Hydrogen-Terminated Silicon. *J. Am. Chem. Soc.* **1995**, 117, 3145-3155.

16. Boukherroub, R.; Morin, S.; Bensebaa, F.; Wayner, D. D. M. New Synthetic Routes to Alkyl Monolayers on the Si(111) Surface, *Langmuir*. **1999**, 15, 3831-3835.

17. Sieval, A. B.; Demirel, A. L.; Nissink, J. W. M.; Linford, M. R.; Van der Maas, J. H.; De Jeu, W. H.; Zuilhof, H.; Sudholter, E. J. R. Highly Stable Si−C Linked Functionalized Monolayers on the Silicon (100) Surface. *Langmuir.* **1998**, 14, 1759-1768.

18. Buriak, J. M.; Allen, M. J. Lewis Acid Mediated Functionalization of Porous Silicon with Substituted Alkenes and Alkynes. *J. Am. Chem. Soc.* **1998**, 120, 1339-1340.

19. de Smet, L. C. P. M.; Zuilhof, H.; Sudholter, E. J. R.; Lie, L. H; Houlton, A.; Horrocks, B. R. Mechanism of the Hydrosilylation Reaction of Alkenes at Porous Silicon: Experimental and Computational Deuterium Labeling Studies. *J. Phys. Chem. B.* **2005**, 109, 12020-12031.

20. Higashi, G. S.; Chabal, Y. J.; Trucks, G. W.; Raghavachari, K. Ideal Hydrogen Termination of the Si (111) Surface. *Appl. Phys. Lett.* **1990**, 56, 656-658.

21. Hines, M. A. The picture Tells the Story: Using Surface Morphology to Probe Chemical Etching Reactions. *Int. Rev. Phys. Chem*. **2001**, 20, 645-672.

22. Wintersteiner, O.; Abramson, H. A. The Isoelectric Point of Insulin: Electrical Properties of Adsorbed and Crystalline Insulin. *J. Biol. Chem.* **1933**, 99, 741-753.

23. Laogun, A. A.; Sheppard, R. J.; Grant, E. H Dielectric Properties of Insulin in Solution. *Phys. med. biol*. **1984**, 29, 519-524.

24. Wright, J. E. I.; Cosman, N. P.; Fatih, K.; Omanovic, S.; Roscoe, S. G. Electrochemical Impedance Spectroscopy and Quartz Crystal Nanobalance (EQCN) Studies of Insulin Adsorption on Pt. *J. Electroanal. Chem.* **2004**, 564, 185-197.

25. Lakhiari, H.; Muller, D. Insulin Adsorption on Coated Silica Based Supports Grafted with N-Acetylglucosamine by Liquid Affinity Chromatography. *J. Chromatogr. B: Anal. Technol. Biomed. Life Sci.* **2004**, 808, 35-41.

26. Mayer, J. P.; Zhang, F.; DiMarchi, R. D. Insulin Structure and Function. *Pept. Sci.* **2007**, 88, 687-713.

27. Macdonald, S. M.; Roscoe, S. G. Electrochemical Studies of the Interfacial Behavior of Insulin. *J. Colloid Interface Sci.* **1996**, 184, 449-455.

28. Pocker, Y.; Biswas, S. B. Self-Association of Insulin and the Role of Hydrophobic Bonding: A Thermodynamic Model of Insulin Dimerization. *Biochemistry.* **1981**, 20, 4354-4361.

29. Jeffrey, P. D.; Coates, J. H. An Equilibrium Ultracentrifuge Study of the Effect of Ionic Strength on the Self-Association of Bovine Insulin. *Biochemistry.* **1966**, 5, 3820-3824.

30. Mollmann, S. H.; Jorgensen, L.; Bukrinsky, J. T.; Elofsson, U.; Norde, W.; Frokjaer, S. Interfacial Adsorption of Insulin: Conformational Changes and Reversibility of Adsorption. *Eur. J. Pharm. Sci.* **2006**, 27, 194-204.

31. Buijs, J.; Vera, C. C.; Ayala, E.; Steensma, E.; Haakansson, P.; Oscarsson, S. Conformational Stability of Adsorbed Insulin Studied with Mass Spectrometry and Hydrogen Exchange. *Anal. Chem.* **1999**, 71, 3219-3225.

32. McClellan, S. J.; Franses, E. I. Adsorption of Bovine Serum Albumin at Solid/Aqueous Interfaces. *Colloids Surf. A.* **2005**, 260, 265-275.

33. Hirayama, K.; Akashi, S.; Furuya, M.; Fukuhara, K. Rapid Confirmation and Revision of the Primary Structure of Bovine Serum Albumin by ESIMS and Frit-FAB LC/MS. *Biochem. Biophys. Res. Commun.* **1990**, 173, 639-646.

34. El Kadi, N.; Taulier, N.; Le Huerou, J. Y.; Gindre, M.; Urbach, W.; Nwigwe, I.; Kahn, P. C.; Waks, M. Unfolding and Refolding of Bovine Serum Albumin at Acid pH: Ultrasound and Structural Studies. *Biophys. J.* **2006**, 91, 3397-3404.

35. Tsai, D. H.; DelRio, F. W.; Keene, A. M.; Tyner, K. M.; MacCuspie, R. I.; Cho, T. J.; Zachariah, M. R.; Hackley, V. A. Adsorption and Conformation of Serum Albumin Protein on Gold Nanoparticles Investigated Using Dimensional Measurements and in Situ Spectroscopic Method. *Langmuir.* **2011**, 27, 2464-2477.

36. Ferrer, M. L.; Duchowicz, R.; Carrasco, B.; de la Torre, J. G.; Acuna, A. U. The Conformation of Serum Albumin in Solution: A Combined Phosphorescence Depolarization-Hydrodynamic Modeling Study. *Biophys. J.* **2001**, 80, 2422-2430.

37. Dupont-Gillain, C. C.; Fauroux, C. M. J.; Gardner, D. C. J.; Leggett, G. J. Use of AFM to Probe the Adsorption Strength and Time- Dependent Changes of Albumin on Self-Assembled Monolayers. *J. Biomed. Mater. Res. Part A.* **2003**, 67, 548-558.

38. Das, A.; Chitra, R.; Choudhury, R. R.; Ramanadham, M. Structural Changes During the Unfolding of Bovine Serum Albumin in the Presence of Urea: A Small-Angle Neutron Scattering Study. *Pramana*. **2004**, 63, 363-368.

39. Valle-Delgado, J. J.; Molina-Bolivar, J. A.; Galisteo-Gonzalez, F.; Galvez-Ruiz, M. J.; Feiler, A.; Rutland, M. Structural Changes During the Unfolding of Bovine Serum Albumin in the Presence of Urea: A Small-Angle Neutron Scattering Study. *J. Phys. Chem. B.* **2004**, 108, 5365-5371.

40. Peters Jr, T. Serum Albumin. *Adv. Protein Chem.* **1985**, 37, 161-245.

41. Carter, D. C.; Ho, J. X. Structure of Serum Albumin. *Adv. Protein Chem.* **1994**, 45, 153-203.

42. Roach, P.; Farrar, D.; Perry, C. C. Interpretation of Protein Adsorption: Surface-Induced Conformational Changes. *J. Am. Chem. Soc.* **2005**, 127, 8168-8173.

43. Mirabella, F. M. Internal Reflection Spectroscopy: Theory and Applications, In *Practical Spectroscopy Series*; Brame, E. G., Ed.; Marcel Dekker: New York, 1992, vol. 15.

44. Ratcliff, G. C.; Erie, D. A Novel Single-Molecule Study to Determine Protein-Protein Association Constants. *J. Am. Chem. Soc.* **2001**, 123, 5632-5635.

45. Peter E.; Paul, W. Atomic Force Microscopy; Oxford University: New York, 2010.

46. Faucheux, A.; Gouget-Laemmel, A. C.; de Villeneuve, C. H.; Boukherroub, R.; Ozanam, F.; Allongue, P.; Chazalviel, J. N. Well-Defined Carboxyl-Terminated Alkyl Monolayers Grafted onto H-Si(111): Packing Density from a Combined AFM and Quantitative IR Study. *Langmuir*. **2006**, 22, 153-162.

47. Allongue, P.; Kieling, V.; Gerischer, H. Etching Mechanism and Atomic Structure of H-Si(111) Surfaces Prepared in NH_4F. *Electrochim. Acta.* **1995**, 40, 1353-1360.

48. Allongue, P.; de Villeneuve, C. H.; Morin, S.; Boukherroub, R.; Wayner, D. D. M. The Preparation of Fat H–Si(111) Surfaces in 40% NH_4F Revisited. *Electrochim. Acta.* **2000**, 45, 4591-4598.

49. Wade, C. P.; Chidsey, C. E. D. Etch-Pit Initiation by Dissolved Oxygen on Terraces of H-Si(111). *Appl. Phys. Lett.* **1997**, 71, 1679-1681.

50. Ta, T. C.; McDermott, M. T. Investigation of Dual Component Protein Films on Graphite with Scanning Force Microscopy. *Colloids Surf. B.* **2003**, 32, 191-202.

References of Chapter 3

1. Audette, G. F.; van Schaik, E. J.; Hazes, B.; Irvin, R. T. DNA-Binding Protein Nanotubes: Learning from Nature's Nanotech Examples. *Nano Lett.* **2004**, 4, 1897-1902.

2. Lee, J. S.; Latimer, L. J. P.; Reid, R. S. A Cooperative Conformational Change in Duplex DNA Induced by Zn^{2+} and Other Divalent Metal Ions. *Biochem. Cell Biol.* **1993**, 71, 162-168.

3. Aich, P.; Labiuk, S. L.; Tari, L. W.; Delbaere, L. T. J.; Roesler, W. J.; Falk, K. J.; Steer, R. P.; Lee, J. S. M-DNA: A Complex between Divalent Metal Ions and DNA which Behaves as a Molecular Wire. *J. Mol. Biol.* **1999**, 294, 477-485.

4. Aich, P.; Skinner, R. J.; Wettig, S. D.; Steer, R. P.; Lee, J. S. Long Range Molecular Wire Behaviour in a Metal Complex of DNA. *J. Biomol. Struct. Dyn.* **2002**, 20, 93-98.

5. Rakitin, A.; Aich, P.; Papadopoulos, C.; Kobzar, Y.; Vedeneev, A. S.; Lee, J. S.; Xu, J. M. Metallic Conduction through Engineered DNA: DNA Nanoelectronic Building Blocks. *Phys. Rev. Lett.* **2001**, 86, 3670-3673.

6. Wettig, S. D.; Bare, G. A.; Skinner, R. J. S.; Lee, J. S. Signal Transduction through Dye-Labeled M-DNA Y-Branched Junctions: Switching Modulated by Chemical Reduction of Anthraquinone. *Nano Lett.* **2003**, 3, 617-622.

7. Wettig, S.D.; Li, C. Z.; Long, Y. T.; Kraatz, H. B.; Lee, J. S.; M-DNA: a Self-Assembling Molecular Wire for Nanoelectronics and Biosensing. *Anal. Sci.* **2003**, 19, 23-26.

8. Reguera, G.; McCarthy, K. D.; Mehta, T.; Nicoll, J. S.; Tuominen, M. T.; Lovley, D. R. Extracellular Electron Transfer via Microbial Nanowires. *Nature.* **2005**, 435, 1098-1101.

9. Gorby, Y. A.; Yanina, S.; McLean, J. S.; Rosso, K. M.; Moyles, D.; Dohnalkova, A.; Beveridge, T. J.; Chang, I. S.; Kim, B. H.; Kim, K. S.; Culley, D. E.; Reed, S. B.; Romine, M. F.; Saffarini, D. A.; Hill, E. A.; Shi, L.; Elias, D. A.; Kennedy, D. W.; Pinchuk, G.; Watanabe, K.; Ishii, S.; Logan, B.; Nealson K. H.; Fredrickson J. K.; Electrically Conductive Bacterial Nanowires Produced by *Shewanella Oneidensis* Strain MR-1 and other Microorganisms. *Proc. Natl. Acad. Sci. U. S. A.* **2006,** 103, 11358-11363.

10. Audette, G. F.; Hazes, B. Development of Protein Nanotubes from a Multi-Purpose Biological Structure. *J. Nanosci. Nanotechnol.* **2007**, 7, 2222-2229.

11. Xie, S.; Li, W.; Pan, Z.; Chang, B.; Sun, L. Mechanical and Physical Properties on Carbon Nanotube. *J. Phys. Chem. Solids.* **2000**, 61, 1153-1158.

12. Hazes, B.; Dijkstra, B. W. Model Building of Disulfide Bonds in Proteins with Known Three-Dimensional Structure. *Protein Eng.* **1988**, 2, 119-125.

13. Lombardo, S.; Zahedi Jasbi, S.; Jeung, S.; Morin, S.; Audette, G. F. Initial Studies of Protein Nanotube Oligomerization from a Modified Gold Surface. *J. Bionanosci.* **2009**, 3, 61-65.

14. Love, J. C.; Estroff, L. A; Kriebel, J. K; Nuzzo, R. G.; Whitesides, G. Self-Assembled Monolayers of Thiolates on Metals as a Form of Nanotechnology. *Chem. Rev.* **2005**, 105, 1103-1170.

15. Sanderson, R. T. Chemical Bonds and Bond Energy; 2nd Ed. Academic: New York, 1976.

16. Kondoh, H.; Kodama, C.; Sumida, H.; Nozoye, H. Molecular Processes of Adsorption and Desorption of Alkanethiol Monolayers on Au(111). *J. Chem. Phys.* **1999**, 111, 1175-1184.

17. Schreiber, F. Structure and Growth of Self-Assembling Monolayers. *Prog. surf. sci.* **2000**, 65, 151-257.

18. Poirier, G. E. Mechanism of Formation of Au Vacancy Islands in Alkanethiol Monolayers on Au(111). *Langmuir.* **1997**, 13, 2019-2026.

19. Yang, G.; Liu, G.-Y. New Insights for Self-Assembled Monolayers of Organothiols on Au(111) Revealed by Scanning Tunneling Microscopy. *J. Phys. Chem. B.* **2003**, 107, 8746-8759.

20. Stranick, S. J.; Parikh, A. N.; Allara, D. L.; Weiss, P. S. A New Mechanism for Surface Diffusion: Motion of a Substrate-Adsorbate Complex *J. Phys. Chem.* **1994**, 98, 11136-11142.

21. Stranick, S. J.; Kamna, M. M.; Krom, K. R.; Parikh, A. N.; Allara, D. L.; Weiss, P. S. Scanning Tunneling Microscopy Studies of Self-Assembled Monolayers of Alkanethiols on Gold. *J. Vac. Sci. Technol. B Microelectron. Nanometer Struct.* **1994**, 12, 2004-2007.

22. Chen, S.; Li, L.; Boozer, C. L; Jiang, S. Controlled Chemical and Structural Properties of Mixed Self-Assembled Monolayers of Alkanethiols on Au(111). *Langmuir.* **2000**, 16, 9287-9293.

23. Lee, M. T.; Hsueh, C. C.; Freund, M. S.; Ferguson, G. S. Air Oxidation of Self-Assembled Monolayers on Polycrystalline Gold: The Role of the Gold Substrate. *Langmuir*. **1998**, 14, 6419-6423.

24. Hutt, D. A; Leggett, G. L. Influence of Adsorbate Ordering on Rates of UV Photooxidation of Self-Assembled Monolayers. *J. Phys. Chem.* **1996**, 100, 6657-6662.

25. Schoenfisch, M. H.; Pemberton, J. E. Air Stability of Alkanethiol Self-Assembled Monolayers on Silver and Gold Surfaces. *J. Am. Chem. Soc.* **1998**, 120, 4502-4513.

26. Audette, G. F.; Irvin, R. T.; Hazes, B. Crystallographic Analysis of the *Pseudomonas aeruginosa* Strain K122-4 Monomeric Pilin Reveals a Conserved Receptor-Binding Architecture. *Biochemistry.* **2004**, 43, 11427-11435.

27. Keizer, D. W.; Slupsky, C. M.; Kalisiak, M.; Campbell, A. P.; Crump, M. P.; Sastry, P. A.; Hazes, B.; Irvin, R. T.; Sykes, B. D. Structure of a Pilin Monomer from *Pseudomonas aeruginosa* Implications for the Assembly of Pili, *J. Biol. Chem.* **2001**, 276, 24186-24193.

28. Chen, C. J. Introduction to Scanning Tunneling Microscopy; Oxford University: New York, 1993.

29. Oura, K.; Lifshits, V. G.; Saranin, A. A.; Zotov, A. V.; Katayama, M. Surface Science: An Introduction; Springer-Verlag: Berlin, 2003.

30. Bonnell, D.; Huey, B. D. Electron Tunneling, Atomic Forces and Scanning Probe Microscopy, In *Scanning Probe Microscopy and Spectroscopy: Theory, Techniques and Applications*; Bonnell, D., Ed.; 2nd ed. Wiley-VCH: New York, 2001.

31. Porter, M. D.; Bright, T. B.; Allara, D. L.; Chidsey, C. E. D. Spontaneously Organized Molecular Assemblies. 4. Structural Characterization of n-Alkyl Thiol Monolayers on Gold by Optical Ellipsometry, Infrared Spectroscopy and Electrochemistry. *J. Am. Chem. Soc.* **1987**, 109, 3559-3568.

32. Snyder, R. J.; Strauss, H. L.; Elliger, C. A. C-H Stretching Modes and the Structure of n-Alkyl Chains. 1. Long, Disordered, Chains. *J. Phys. Chem.* **1982**, 86, 5145-5150.

33. Kang, J. H.; Zhu, X. Y. Layer-by-Layer Growth of Incommensurate, Polycrystalline, Lying-Down Pentacene Thin Films on Au(111). *Chem. Mater.* **2006,** 18, 1318-1323.

References of Chapter 4

1. Orazem, M. E.; Tribollet, B. Electrochemical Impedance Spectroscopy; John Wiley and Sons: Hoboken, 2008.

2. Barsoukov, E.; Macdonald, J. R. Impedance Spectroscopy: Theory, Experiment and Applications; 2nd Ed. John Wiley and Sons: Hoboken, 2005.

3. Lvovich, V. F. Impedance Spectroscopy: Applications to Electrochemical and Dielectric Phenomena; John Wiley and Sons: Hoboken, 2012.

4. Lasia, A. Electrochemical Impedance Spectroscopy and Its Applications, In *Modern Aspects of Electrochemistry*; Conway, B. E., Bockris, J., White, R. E., Eds.; Kluwer Academic/Plenum: New York, 1999, Vol. 32.

5. O'Brien, B.; Sahalov, H.; Searson, P. C. The Temperature Dependence of the Impedance of Alkanethiol Self-Assembled Monolayers. *Appl. Phys. Lett.* **2010**, 97, 043110-1 -043110-3.

6. Darwish, N.; Eggers, P. K.; Ciampi, S.; Zhang, Y.; Tong, Y.; Ye, S.; Paddon-Row, M. N.; Gooding, J. J. Reversible Potential-Induced Structural Changes of Alkanethiol Monolayers on Gold Surfaces. *Electrochem. Commun.* **2011**, 13, 387-390.

7. Sahalov, H.; O'Brien, B.; Stebe, K. J.; Hristova, K.; Searson, P. C. Influence of Applied Potential on the Impedance of Alkanethiol SAMs. *Langmuir.* **2007**, 23, 9681-9685.

8. Campina, J. M.; Martins, A.; Silva, F. Selective Permeation of a Liquidlike Self-Assembled Monolayer of 11-Amino-1-undecanethiol on Polycrystalline Gold by Highly Charged Electroactive Probes. *J. Phys. Chem. C.* **2007**, 111, 5351-5362.

9. Degefa, T. H.; Kwak, J. Electrochemical Impedance Sensing of DNA at PNA Self-Assembled Monolayer. *J. Electroanal. Chem.* **2008**, 612, 37-41.

10. Park, J. Y.; Park, S. M. DNA Hybridization Sensors Based on Electrochemical Impedance Spectroscopy as a Detection Tool. *Sensors.* **2009**, 9, 9513-9532.

11. Ge, C.; Tan, Y.; Liao, J.; Zhang, Y.; Zhang, H.; Gu, N. Potential Control of DNA Self-Assembly on Gold Electrode. *Chin. Sci. Bull.* **2002**, 47, 370-375.

12. Mohsen, Q.; Fadl-allah, S. A.; El-Shenawy, N. S. Electrochemical Impedance Spectroscopy Study of the Adsorption Behavior of Bovine Serum Albumin at Biomimetic Calcium–Phosphate Coating. *Int. J. Electrochem. Sci.* **2012**, 7, 4510 - 4527.

13. Singh, R.; Suni, I. I. Minimizing Nonspecific Adsorption in Protein Biosensors that Utilize Electrochemical Impedance Spectroscopy. *J. Electrochem. Soc.* **2010**, 157, 334-337.

14. Liu, M.; Zhang, Y.; Wang, M.; Deng, C.; Xie, Q.; Yao, S. Adsorption of Bovine Serum Albumin and Fibrinogen on Hydrophilicity-Controllable Surfaces of Polypyrrole Doped with Dodecyl Benzene Sulfonate-A Combined Piezoelectric Quartz Crystal Impedance and Electrochemical Impedance Study. *Polymer.* **2006**, 47, 3372-3381.

15. Moisel, M.; de Mele, M. A. F. L.; Muller, W. D. Biomaterial Interface Investigated by Electrochemical Impedance Spectroscopy. *Adv. Eng. Mater.* **2008**, 10, 33-46.

16. Smiechowski, M. F.; Lvovich, V. F.; Roy, S.; Fleischman, A.; Fissell, W. H.; Riga, A. T. Electrochemical Detection and Characterization of Proteins. *Biosens. Bioelectron.* **2006**, 22, 670-677.

17. Bard, A. J.; Fulkner, L. R. Electrochemical Methods Fundamental and Applications; 2nd Ed. John Wiley and Sons: New York, 2001.

18. Skoog, D. A.; Holler, F. J.; Nieman, T. A. Principles of Instrumental Analysis; 5th Ed. Harcourt Brace: Philadelphia, 1998.

19. Brug, G. J.; Van den Eeden, A. L. G.; Sluyters-Rehbach, M.; Sluyters, J. H. The Analysis of Electrode Impedances Complicated by the Presence of a Constant Phase Element. *J. Electroanal. Chem.* **1984**, 176, 275-295.

20. Hsu, C. H.; Mansfeld, F. Technical Note: Concerning the Conversion of the Constant Phase Element Parameter Y_0 into a Capacitance. *Corrosion.* **2001**, 57, 747-748.

21. Hirschorn, B.; Orazem, M. E.; Tribollet, B.; Vivier, V.; Frateur I.; Musiani, M. Determination of Effective Capacitance and Film Thickness from Constant-Phase-Element Parameters. *Electrochim. Acta.* **2010**, 55, 6218.

22. Boubour E.; Tennox, R. B. Stability of ω-Functionalized Self-Assembled Monolayers as a Function of Applied Potential. *Langmuir.* **2000**, 16, 7464–7470.

23. Porter, M. D.; Bright, T. B.; Allara, D. L.; Chidsey, C. E. D. Spontaneously Organized Molecular Assemblies. 4. Structural Characterization of n-Alkyl Thiol Monolayers on Gold by Optical Ellipsometry, Infrared Spectroscopy and Electrochemistry. *J. Am. Chem. Soc.* **1987**, 109, 3559-3568.

24. Lefrou, C.; Fabry, P.; Poignet, J.-C. Electrochemistry: the Basics, with Examples; Springer: Berlin, 2012.

25. Finklea, H. O. Electrochemistry of Organized Monolayers of Thiols and Related Molecules on Electrodes, In *Electroanalytical Chemistry*; Bard, A. J., Rubenstein, I., Eds.; Marcel Dekker: New York, 1996, Vol. 19.

26. Eberhardt, D.; Santos, E.; Schmickler, W. Impedance Studies of Reconstructed and Non-Reconstructed Gold Single Crystal Surfaces. *J. Electroanal. Chem.* **1996**, 419, 23-31.

27. Hamelin, A. The Electrochemical Double Layer on sp Metal Single Crystals: The Current Status of Data. *J. Electroanal. Chem.* **1983**, 145, 225-164.

28. Bianchi, J.; Mazza, F.; Mussini, T. Oxygen and Hydrogen-Peroxide Processes on Gold Electrodes in Acid Solutions. *Electrochim. Acta*. **1966**, 11, 1509-1523.

29. Genshaw, M.A.; Damjanovic, A.; Bockris, J.O'M. Hydrogen Peroxide Formation in Oxygen Reduction at Gold Electrodes: I. Acid Solution. *J. Electroanal. Chem*. **1967**, 15, 163-172.

30. Damjanovic, A.; Genshaw, M.A.; Bockris, J.O'M. Hydrogen Peroxide Formation in Oxygen Reduction at Gold Electrodes: II. Alkaline Solution. *J. Electroanal. Chem.* **1967**, 15, 173-180.

31. Wroblowa, H.S.; Pan, Y.C.; Razumney, G. Electroreduction of Oxygen: A New Mechanistic Criterion. *J. Electroanal. Chem.* **1976**, 69, 195-201.

32. Adzic, R.R.; Strbac, S.; Anastasijevic, N. Electrocatalysis of Oxygen on Single Crystal Gold Electrodes. *Mater. Chem. Phys*. **1989**, 22, 349-375.

33. Slowinski, K.; Majda, M. Mercury–Mercury Tunneling Junctions: Part II. Structure and Stability of Symmetric Alkanethiolate Bilayers and Their Effect on the Rate of Electron Tunneling. *J. Electroanal. Chem.* **2000**, 491, 139-147.

34. Wang, B.; Luo, J.; Wang, X.; Wang, H.; Hou, J. G. Dielectric Properties and Frequency Response of Self-Assembled Monolayers of Alkanethiols. *Langmuir.* **2004**, 20, 5007-5012.

35. Bird, J. Electrical and Electronic Principles and Technology; 4th Ed. Elsevier; Oxford, 2010.

36. Gilson, M. K.; Honig, B. H. The Dielectric Constant of a Folded Protein. *Biopolymers.* **1986**, 25, 2097-2119.

37. Bone, S.; Pethig, R. Dielectric Studies of Protein Hydration and Hydration-Induced Flexibility. *J. Mol. Biol.* **1985**, 181,323-326.

38. Kukic, P.; Farrell, D.; McIntosh, L. P.; Garcia-Moreno, B. E.; Jensen, K. S.; Toleikis, Z.; Teilum, K.; Nielsen, J. E. Protein Dielectric Constants Determined from NMR Chemical Shift Perturbations. *J. Am. Chem. Soc.* **2013**, 135, 16968–16976.

39. Antosiewicz, J.; McCammon, J. A.; Gilson, M. K. Prediction of PH-Dependent Properties of Proteins. *J. Mol. Biol.* **1994**, 238, 415-436.

40. Vicatos, S.; Roca, M.; Warshel, A. Effective Approach for Calculations of Absolute Stability of Proteins Using Focused Dielectric Constants. *Proteins Struct. Funct. Bioinf.* **2009**, 77, 670-684.

41. Homma, T.; Tamakai, A.; Nakai, H.; Osaka, T. Molecular Orbital Study on the Reaction Process of Dimethylamine Borane as a Reductant for Electroless Deposition. *J. Electroanal. Chem.* **2003**, 559, 131-136.

42. Audette, G. F.; Irvin, R. T.; Hazes, B. Crystallographic Analysis of the *Pseudomonas aeruginosa* Strain K122-4 Monomeric Pilin Reveals a Conserved Receptor-Binding Architecture. *Biochemistry.* **2004**, 43, 11427–11435.

References of Chapter 5

1. Wang, Z. L. Nanobelts, Nanowires, and Nanodiskettes of Semiconducting Oxides-From Materials to Nanodevices. *Adv. Mater.* **2003**, 15, 432-436.

2. Gazit, E. Use of Biomolecular Templates for the Fabrication of Metal Nanowires. *FEBS J.* **2007**, 274, 317-322.

3. Richter, J.; Seidel, R.; Kirsch, R.; Mertig, M.; Pompe, W.; Plaschke J.; Schackert, H. Nanoscale Palladium Metallization of DNA. *Adv. Mater.* **2000**, 12, 507-510.

4. Wong, K.; Mann, S. Biomimetic Synthesis of Cadmium Sulfide-Ferritin Nanocomposites. *Adv. Mater.* **1996**, 8, 928-932.

5. Shenton, W.; Douglas, T.; Young, M.; Stubbs, G.; Mann, S. Inorganic–Organic Nanotube Composites from Template Mineralization of Tobacco Mosaic Virus. *Adv. Mater.* **1999**, 11, 253-256.

6. Shenton, W.; Davis, S.; Mann, S. Directed Self-Assembly of Nanoparticles into Macroscopic Materials Using Antibody–Antigen Recognition. *Adv. Mater.* **1999**, 11, 449-452.

7. Kirsch, R.; Mertig, M.; Pompe, W.; Wahl, R.; Sadowski, G.; Bohm, K.-J.; Unger, E. Three-Dimensional Metallization of Microtubules. *Thin Solid Films*. **1997**, 305, 248-253.

8. Eichen, Y.; Braun, E.; Sivan, U.; Ben-Yoseph, G. Self-Assembly of Nanoelectronic Components and Circuits Using Biological Template. *Acta Polym.* **1998**, 49, 663-670.

9. Ijiro, K.; Matsuo, Y.; Hashimoto, Y. DNA-Based Silver Nanowires Fabricated by Electroless Plating. *Mol. Cryst. Liq. Cryst.* **2006**, 445, 207-211.

10. Suchentrunk, R. Metallizing of plastics: a Handbook of Theory and Practice; ASM International: Materials Park, OH, 1993.

11. Kind, H.; Bittner, A. M.; Cavalleri, O.; Kern, K. Electroless Deposition of Metal Nanoislands on Aminothiolate-Functionalized Au(111) Electrodes. *J. Phys. Chem. B.* **1998**, 102, 7582-7589.

12. Balci, S.; Bittner, A. M.; Hahn, K.; Scheu, C.; Knez, M.; Kadri, A.; Wege, C.; Jeske, H.; Kern, K. Copper Nanowires within the Central Channel of Tobacco Mosaic Virus Particles. *Electrochim. Acta.* **2006**, 51, 6251-6257.

13. Okinaka, Y.; Osaka, T. Electroless Deposition Processes: Fundamentals and Applications, In *Advances in Electrochemical Science and Engineering*; Gerischer, H., Tobias, C. W., Eds.; VCH: Weinheim, 1990, Vol. 3.

14. Weber, C. J.; Pickering, H. W.; Weil, K. G.; Surface Development during Electroless Copper Deposition. *J. Electrochem. Soc.* **1997**, 144, 2364-2369.

15. Pourbaix, M. Atlas of Electrochemical Equilibria in Aqueous Solutions; National Association of Corrosion Engineers: Houston, 1974.

16. Shacham-Diamand, Y.; Dubin, V.; Angyal, M. Electroless Copper Deposition for ULSI. *Thin Solid Films.* **1995**, 262, 93-103.

17. Sard, R. The Nucleation, Growth and Structure of Electroless Copper Deposits. *J. Electrochem. Soc.* **1970**, 117, 864-870.

18. Ma, C.; Ye, W.; Shi, X.; Chang, Y.; Chen, Y.; Wang, C. Comparative Study of Electroless Copper Deposition Based on the Seed Layers of Pd, PtPd and AuPd. *Appl. Surf. Sci.* **2009**, 255, 3713-3718.

19. Bindra, P.; White, J. R. Fundamental Aspects of Electroless Copper Plating, In *Electroless Plating*; Mallory, G. O., Hajdu, J. B., Eds.; Cambridge University: New York, 1990.

20. Fultz, B.; Howe, J. Transmission Electron Microscopy and Diffractometry of Materials; Springer: Berlin, 2008.

21. Champness, P. E. Electron Diffraction in the Transmission Electron Microscope; Taylor and Francis: Oxford, 2001.

22. Aksu, S.; Doyle, F. M. Potential-pH Diagrams for Copper in Aqueous Solutions of Various Organic Complexing Agents, In *Electrochemistry in Mineral and Metal processing V*; Richardson, P. E., Srinivasan, S., Woods, R., Eds.; Electrochemical Society: Pennington, 2000.

23. Knez, M.; Bittner, A. M.; Boes, F.; Wege, C.; Jeske, H.; Maib, E.; Kern, K. Biotemplate Synthesis of 3-nm Nickel and Cobalt Nanowires. *Nano Lett.* **2003**, 3, 1079-1082.

24. Hsu, H.-H.; Teng, C.-W.; Lin S.-J.; Yeh, J.-W. Sn/Pd Catalyzation and Electroless Cu Deposition on TaN Diffusion Barrier Layers. *J. Electrochem. Soc.* 2002, 149, C143-C149.

25. Dressick, W. J.; Dulcey, C. S.; Georger, J. H.; Calabrese, G. S.; Calvert, J. M. Covalent Binding of Pd Catalysts to Ligating Self-Assembled Monolayer Films for Selective Electroless Metal Deposition. *J. Electrochem. Soc.* **1994**, 141, 210-220.

26. Moller, F. A.; Magnussen O. M.; Behm, R. J. In Situ STM Studies of Cu Underpotential Deposition on Au(100) in the Presence of Sulfate and Chloride Anions. *Phys. Rev. B Condens. Matter.* **1995**, 51, 2484-2490.

27. Polewska, W.; Behm, R. J.; Magnussa, O. M. In-Situ Video-STM Studies of Cu Electrodeposition on Cu(100) in HCl Solution. *Electrochim. Acta.* **2003**, 48, 2915-2921.

28. Kim, J. Y.; Kim, Y.-G.; Stickney, J. L. Cu Nanofilm Formation by Electrochemical Atomic Layer Deposition (ALD) in the Presence of Chloride Ions. *J. Electroanal. Chem.* **2008**, 621, 205-213.

29. Habicht, W.; Behrens, S.; Wu, J.; Unger, E.; Dinjus, E. Characterization of Metal Decorated Protein Templates By Scanning Electron/Scanning Force Microscopy and Microanalysis. *Surf. Interface Anal.* **2004**, 36, 720-723.

30. Vernick, S.; Moscovich-Dagan, H.; Porat-Ophir, C.; Rishpon, J.; Freeman, A.; Shacham-Diamand, Y. Directed Metallization of Single-Enzyme Molecules With Preserved Enzymatic Activity. *IEEE Trans. Nanotechnol.* **2009**, 8 , 95-99.

31. Homma, T.; Tamakai, A.; Nakai, H.; Osaka, T. Molecular Orbital Study on the Reaction Process of Dimethylamine Borane as a Reductant for Electroless Deposition. *J. Electroanal. Chem.* **2003**, 559, 131-136.

32. Sadik, O. A.; Xu H.; Sargent, A.; Multi-Electron Transfer Mechanism of Dimethylamine Borane in Electroless Gold Deposition. *J. Electroanal. Chem.* **2005**, 583, 167-175.

33. Keizer, D. W.; Slupsky, C. M.; Kalisiak, M.; Campbell, A. P.; Crump, M. P.; Sastry, P. A.; Hazes, B.; Irvin, R. T.; Sykes, B. D. Structure of a Pilin Monomer from

Pseudomonas aeruginosa, Implications for the Assembly of Pili. *J. Biol. Chem.* **2001**, 276, 24186-24193.

34. El-Sherif, A. A. Coordination Chemistry of Palladium(II) Ternary Complexes with Relevant Biomolecules, In *Stoichiometry and Research - The Importance of Quantity in Biomedicine*; Innocenti, A., Ed.; InTech Europe: Rijeka, 2012.

35. Knez, M.; Sumser, M.; Bittner, A. M.; Wege, C.; Jeske, H.; Martin, T. P.; Kern, K. Spatially Selective Nucleation of Metal Clusters on the Tobacco Mosaic Virus. *Adv. Funct. Mater*. **2004**, 14, 116-124.

36. Pearson, R. G. Hard and Soft Acids and Bases. *J. Am. Chem. Soc.* **1963**, 85, 3533-3539.

37. Mertig, M.; Kirsch, R.; Pompe, W. Biomolecular Approach to Nanotube Fabrication. *Appl. Phys. A: Mater. Sci. Process.* **1998**, 66, S723-S727.

38. Lehninger, A. L.; Nelson, D. L.; Cox, M. M. Lehninger Principles of Biochemistry; 4th Ed. W. H. Freeman: New York, 2004.

39. Appleton, T. G.; Bailey, A. J.; Bedgood Jr., D.R.; Hall, J. R. Amino Acid Complexes of Palladium(II). 1. NMR Study of the Reactions of the Diaqua(ethylenediamine)palladium(II) Cation with Ammonia, Betaine, and the Amino Acids $^{+}NH_3(CH_2)_nCO^{2-}$ (n = 1-3). *Inorg. Chem.* **1994**, 33, 217-226.

References of Chapter 6

1. Mengistu, T.Z.; DeSouza, L.; Morin, S. Probing Proteins on Functionalized Silicon Surfaces Using Matrix-Assisted Laser Desorption/Ionization Mass Spectrometry. *J. Chromatogr. A.* **2006**, 1135, 194-202.